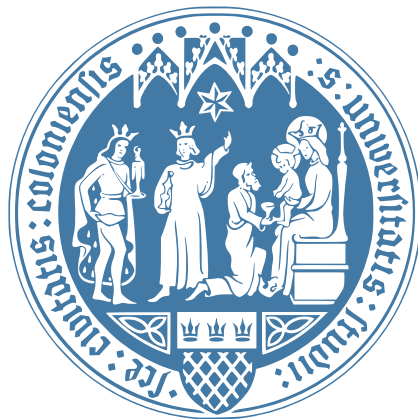


The infrared interferometric capabilities of the Large Binocular Telescope with respect to the Galactic Center

zur

Erlangung des Doktorgrades
der Mathematisch-Naturwissenschaftlichen Fakultät
der Universität zu Köln



vorgelegt von

Hakan Kayan

aus Düren

Köln 2018

Berichterstatter: Prof. Dr. Andreas Eckart
Prof. Dr. Lucas Labadie

Tag der letzten mündlichen Prüfung: 23.07.2018

Abstract

The Galactic Centre is nowadays, after its discovery in 1932 by Karl Jansky, still a major focus of current research in astrophysics. It still has a lot of secrets that are to be discovered and provides the unique opportunity to scrutinise new hypothesis. The crucial part for investigating the Galactic Centre and verifying or rejecting new theories is of course observing and measuring objects in the Galactic Centre. Primarily these measurements deal with position determination of celestial objects or determination of structures. The position determination is of great importance for proper motion measurements. Here, the position of a celestial object is measured through different epochs. These observations are not trivial and hold a lot of difficulties. One of the greatest inconveniences are disturbances in Earth's atmosphere which must be passed by signals from far away in order to reach ground based observatories. A solution is to place the observatories in space, but due to maintaining expenditure and cost for bringing the observatories into space, this solution is less practical, although of course space observatories are used for some applications.

In order to build telescopes with bigger diameters and with a higher resolution, the only practical way is to work with ground based telescopes. In order to overcome the limitation of observing through Earth's atmosphere, adaptive optics are used. Adaptive optics contain a deformable mirror. The surface of this mirror can be adjusted by servos such that it corrects incoming, disturbed wavefront. To do so a guiding source is required, so that the system has a reference for the correct, undisturbed wavefront.

In this thesis the propagation through Earth's atmosphere is simulated with the layer oriented simulation tools (LOST). The performed simulations contain atmospheric models and produce as result point spread functions (PSF). These PSFs contain the performed corrections of the adaptive optics and show the effects of both the corrected atmospheric and instrumental effects when imaging via ground

based telescopes. The simulated telescope is the large binocular telescope (LBT) which is positioned on Mount Graham. Different constellations were simulated with different guiding stars. The obtained PSFs were convolved with different input images of the Galactic Centre which contained science cases in order to get the output image one would obtain when observing the Galactic Centre with the LBT. Finally this output image was de-convolved with PSF in order to get again the input image.

This re-convolved input image was further investigated to understand how efficiently the science cases can be reconstructed. A measure for the quality of the re-convolution is the error with which the science cases could be located in the re-convolved input image.

Zusammenfassung

Das galaktische Zentrum ist seit seiner Entdeckung in 1932 durch Karl Jansky, immer noch ein Hauptforschungsobjekt in der Astrophysik. Es birgt immer noch ungelöste Geheimnisse und gibt die einzigartige Möglichkeit zur Prüfung neuer Hypothesen. Der entscheidende Teil der Untersuchung des galaktischen Zentrums und die damit verbundene Verifizierung beziehungsweise Ablehnung von Theorien ist selbstverständlich die Beobachtung und Messung von Objekten im galaktischen Zentrum. Vorrangig beinhalten diese Messungen Positionsbestimmungen und Analysen von Strukturen. Die Positionsbestimmung ist von größter Bedeutung für die Untersuchung von Eigenbewegungen. Hierbei wird die Position eines himmlischen Objekte über verschiedene Epochen gemessen. Diese Beobachtungen sind nicht trivial und bergen einige Schwierigkeiten. Eine der größten Schwierigkeiten stellen atmosphärische Störung dar, die ein weit entferntes Signal passieren muss um Observatorien auf der Erde erreichen zu können. Eine mögliche Lösung ist es diese Observatorien im Weltall zu platzieren, aber aufgrund von Wartungsaufwand und Kosten ist diese Lösung weniger praktikabel, wobei solche Lösungen natürlich bereits existieren.

Um größere Durchmesser und damit einhergehend eine höhere Auflösung zu erreichen, ist die einzig praktikable Lösung mit Erdteleskopen zu arbeiten. Um die Einschränkungen der Beobachtung durch die Erdatmosphäre zu überwinden, werden adaptive Optiken eingesetzt. Adaptive Optiken beinhalten einen verformbaren Spiegel. Die Oberfläche dieses Spiegels kann mit Servomotoren an die ankommende und verformte Wellenfront angepasst werden. Um dies zu tun, wird eine Leitquelle, damit das System eine Referenz für eine korrekte, ungestörte Wellenfront hat, benötigt

In dieser Arbeit wird die Propagation durch die Erdatmosphäre mit dem Softwarepaket LOST (layer oriented simulation tools) simuliert. Die Simulationen

beinhalten atmosphärische Modelle und produzieren als Ausgabe PSFs (point spread functions). Diese PSFs beinhalten die Korrekturen der adaptiven Optik und zeigen sowohl den Effekt der korrigierten Atmosphäre als auch den der Instrumente, wenn durch die Atmosphäre beobachtet wird. Das simulierte Teleskop ist das LBT (large binocular telescope), das auf Mount Graham positioniert ist. Verschiedene Konstellationen mit unterschiedlichen Leitsternen wurden simuliert. Die erzeugten PSFs wurden mit verschiedenen Eingangsbildern des galaktischen Zentrum, welches wissenschaftlicher Fälle beinhaltet, gefaltet, um das Ausgangsbild zu erzeugen, welches man bei der Beobachtung mit dem LBT sehen würde. Dieses Ausgangsbild wiederum wurde mit der PSF entfaltet, um das ursprüngliche Eingangsbild zu erhalten.

Dieses entfaltete Eingangsbild wurde weiter untersucht, um dann zu verstehen wie wirksam die wissenschaftlichen Fälle rekonstruiert werden können. Ein Maß für die Qualität der Entfaltung ist der Fehler, mit dem die wissenschaftlichen Fälle im entfaltenen Eingangsbild lokalisiert werden können.

Anneme

Contents

List of Figures	21
List of Tables	21
Abbreviation	23
0 Introduction	25
1 Theory	29
1.1 Astronomical interferometer	30
1.1.1 Van Cittert - Zernike theorem	31
1.1.2 Fizeau interferometer	34
1.1.3 Telescope point spread function	36
1.2 Atmospheric turbulences	36
1.2.1 Fluctuation of refraction index	38
1.2.2 Strehl ratio	41
1.2.3 Resolving power	42
1.2.4 Phasevariation	43
1.2.5 Zernike modes	43
1.2.6 Astronomical seeing	45
1.3 Adaptive optics	47
1.3.1 Phase reference	47
1.3.2 Fringe tracking	48
1.4 Galactic center	49
1.4.1 Observing techniques	50
1.4.2 Radio wavelength	51
1.4.3 Far-infrared wavelength	54

1.4.4	Near- and mid-infrared wavelength	55
1.4.5	Optical wavelength	55
1.4.6	X-ray wavelength	56
1.4.7	γ wavelength	57
1.4.8	Sagittarius A*	58
1.5	Parallactic Angle	59
1.6	Altitude	63
1.7	Field rotation	64
1.8	The Large Binocular Telescope	66
1.9	LINC-NIRVANA	68
1.10	Multi Conjugate Adaptic Optics (MCAO)	69
1.11	Functional principle	69
2	Software description	73
2.1	Simulation structure	73
2.2	Simulation setup	74
2.2.1	Telescope and MCAO	74
2.2.2	Atmosphere	74
2.2.3	Computing wind	76
2.2.4	Reference star field	76
2.2.5	Dummy stars	78
2.3	PSF and strelmap	78
2.4	Deconvolution	78
2.5	Simulation parameters	79
3	Simulations	81
3.1	Simulation setup	81
3.2	PSFs	81
3.3	Image generation	88
3.4	Transition smoothing	89
3.5	Cosine-bell function	94
3.6	Galactic Center - low resolution	96
3.7	Galactic center - high resolution	100

Contents	3
----------	---

3.8 De-convolution	104
3.9 Simulation of various science cases	104

4 Science cases 109

4.1 Proper motions of stars within the central stellar cluster	110
4.2 Small stellar associations	114
4.3 Thin dusty filaments	120
4.4 Disk embedded sources	123
4.5 Cometary and asymmetric bow-shock sources	131
4.6 Results	132

5 Summary 135

Bibliography 142

Danksagung 143

Erklärung 145

List of Figures

1	Flickering hot air around jet engines. [Image credit to NASA (2018a), "NASA Armstrong Flight Research Center"]	26
2	Left: observation without adaptive optics, Right: observation with adaptive optics, [Image credit to GMT (2018), "Giant Magellan Telescope"]	26
1.1	Principle structure of a refracting telescope. (Tamás (2018)) 1) Front lens 2) Rear lens 3) Eye 4) Original object 5) Focus point 6) Virtual image	29
1.2	Principle structure of a reflecting telescope: The electromagnetic wave enters through the entry point a) and is focused by concave mirror b) towards the plain mirror c) and finally passed through the exit point d) (Krishnavedala (2018))	30
1.3	Pictograms for the derivating the van Cittert - Zernike theorem. Left: source S at short distance emitting radiation. Observing points 1 and 2. Right: same setup, but this time the source is moved to a very large distance so that the rays appear parallel.	32

1.4	Homothetic pupil condition Fizeau's idea was to place a plate with two holes in the beam path of a telescope. So the telescope becomes a beam combiner for the two sub-beams. By this procedure the brightness distribution of the source can be determined, but of course there is no extension of the field of view (FoV) nor sensitivity. To achieve this goal multiple telescopes must be combined. It is most important that non-axis sub-beams have no optical-path-differences (OPD), so that the combined beam appears to be from one single telescope (Traub (1986)). This condition is fulfilled when the input and exit pupils of each sub-optic are scaled versions of each other.	35
1.5	LINC-NIRVANA PSF for four optical path distances: $0, \frac{1}{3}\pi, \frac{2}{3}\pi, \pi$ from left to right.(Kürster (2010))	37
1.6	C_n^2 profile for Mt. Graham [Masciadri et al. (2010)]	39
1.7	First 15 Zernike polynomials. Vertically ordered by radial degree and horizontally ordered by azimuthal degree. [2pem Wikipedia (2015)]	44
1.8	Galactic center, combined in optical, infrared and X-Ray domains [Image credit to NASA (2018b), "NASA/CXC/SAO"]	49
1.9	Galactic center in radio domain. The bright object in the lower right part is Sgr A*. [Image credit to NASA (2018b), "NASA/CXC/SAO"]	52
1.10	Galactic center in far-infrared domain in different wavelength: $21.3 \mu\text{m}$ (blue), $70 \mu\text{m}$ (green) and $350 \mu\text{m}$ (red). Around the central cavity stretching from 1 to 5 the circumnuclear disk (CND) is visible. [Image credit to Etzaluze et al. (2011)]	54
1.11	Galactic center in infrared domain [Image credit to NASA (2018b), "NASA/CXC/SAO"]	55
1.12	Galactic center in optical domain [Image credit to NASA (2018b), "NASA/CXC/SAO"]	56
1.13	Galactic Center in X-ray domain [Image credit to NASA (2018b), "NASA/CXC/SAO"]	57

1.14	Sagittarius A* in X-ray domain. The image is 15 arcmin across. [Image credit to NASA (2018b), "NASA/CXC/SAO"]	58
1.15	Parallactic angle The parallactic angle q is a function of the hour angle and is defines as the angle in the astronomic triangle opposite to the colatitude and between the altitude and (90° - declination). The other two angles are the azimuth and the hour angle.	60
1.16	Parallactic angle for various declinations	61
1.17	Parallactic angle for the GC	62
1.18	Altitude variation over the hour angle for various declinations and the latitude of LBTO ($B=32.70^\circ$). The amplitude of the altitude is bigger for smaller declinations, that means for a object at the equator level the difference between the highest and lowest position is maximal and for a object at north pole level the celestial object appears always on the same altitude. The highest altitude is reached at a declination of about 30°	63
1.19	Altitude variation over the hour angle for declination $\delta = -29^\circ$ (GC) and latitude $B=32.70^\circ$ (LBTO). The maximum altitude is at 28.298° where the parallactic angle is 0.	64
1.20	Schematic illustration of field rotation: The alt-azimuth mounting of the LBTO causes the image to rotate in the focal plane. That means the observed image rotates corresponding to equation 1.50 and the image in the focal plane rotates like shown in this figure respectively.	65
1.21	Field rotation: The variation \dot{q} of the field rotation is the first derivation of the parallactic angle q in equation ? and describes how fast the parallactic angle changes and, hereby, how fast the detector must rotate. The first derivation is shown here as graphic for the declination $\delta = -29^\circ$ and the latitude $B = 32.70^\circ$	66
1.22	Large Binocular Telescope (LBT), on Mount Graham in southeastern Arizona at an altitude of 3300 m (LBT (2018)), [Image credit: Large Binocular Telescope Observatory]	67
1.23	System and sub-system overview of LINC-NIRVANA (Kürster (2010))	68
1.24	Functional principle of LINC-NIRVANA (Bertram (2007))	70

- 2.1 Software structure: At first in a script file the relevant parameters are set (telescope parameters, stellar field and atmospheric configuration). In the next steps the simulation loops are performed. The number of loops depends on the simulation time. During the loops in each steps image formation is performed. This input is used to perform the DMs commands, which are used to correct the images. The next step is to evolve the atmosphere and again format the image. After the corresponding number of loops are done, the output algorithms provide the output files, i.a. the long exposure PSF files. [Tordi et al. (2002)] 75
- 2.2 Distribution of wind direction and speed: On the left graph the wind speed in x direction and on the right graph the wind speed in y direction are shown on the y axis. The x-axis represent different simulations, that means random distributions for each new calculated atmosphere. The different colours represent the different layers in the atmospheric model. The boxes beneath show the average speed per layer and the corresponding error. The wind speed in both directions is distributed randomly. 77
- 3.1 A grid of 5×5 PSFs were simulated. Each PSF has an edge length of 1360 pixel and is cut to 250 pixel in order to view the non-zero part of the PSF's due to the fact that these cut out parts are of no interest for further consideration. These crops were made in order to have a better view on the PSFs and has no scientific effect. One can see that the structure of the PSFs are as expected: the PSF which are in the area of the NGS are much more narrow and sharper than in the areas far away from the NGS. This corresponds with the strelhmap shown in figure 3.2 83
- 3.2 Strelhmap corresponding to PSFs in figure 3.1: The strelhmap shape shows a maximum at the right side where the NGS was positioned and slopes in all directions. The parallactic angle for this simulation was 35° and the simulated period was 1 second. The other parameters can be seen in table 2.1. 84

- 3.3 Input pictures: The test input-picture is specifically chosen: all points have the same magnitude and all points distributed homogeneously so that the effect of the PSF can be estimated for each part of the field of view equally. 85
- 3.4 Input image in 3.3 convolved with each PSF in figure 3.1: These 25 convolved output images show the expected structures. The first convolved image (in the left top) shows only a smudged though rectangular structure. There is a noisy structure in the middle sector and the intensity seems to drop in a rectangular form towards the edges. No single sharp maxima is recognisable. This corresponds with low quality in the strehmap and the wide and unprecise PSF in figure 3.1. Along the first row towards the fifth convolved image, the image quality increases. Although more structures can be seen, the single points from the input image are only vaguely recognisable. The quality of the convolved images in the 2nd row are already better. Since the 6th convolved image (1st convolved image in 2nd row) is similar to the 5th, the 10th convolved image (last image in 2nd row) already allows to determine all the maxima from the input image. Also, the diffraction limited structure is recognisable. Especially in the middle the single maxima gets more smudged, but still each maxima is visible. For the 15th convolved pictures the best PSF is used. Best means that the PSF is small, sharp and shows the diffraction limited structures. Accordingly each maxima is recognisable with its diffraction limited form and all maxima are clearly separated. Since the given PSFs are axially symmetric, the lower halves of the convolved images are very similar to the upper halves. 87

- 3.5 Overall picture stitched together from convolved pictures from figure 3.4: In order to get an overall picture with an edge length of also 250 pixel, each of the 25 convolved pictures are correspondingly stitched together. That means that from the first convolved picture in the first row a segment in x-direction from 1 to 50 pixel and in y-direction also 1 to 50 pixel is taken and is put in the segment of the overall picture in x-direction from 1 to 50 and in y from 1 to 50. Then from the second convolved picture in the first row a segment in x-direction from 50 to 100 pixel and in y-direction 1 to 50 pixel is taken and is put in the overall picture in x-direction 50 to 100 pixel and in y-direction 1 to 50 pixel. This is done until from each convolved picture the corresponding part is put in the overall picture. 88
- 3.6 Stitchpoint in the overall picture: Exemplary, the column at the position $x = 75$ was chosen to demonstrate the leaps at the transition point in x-direction 50, 100, 150 and 200. Although the transitions seems to be smooth, the cross section figure 3.7 show the leaps at the transitions points. 90
- 3.7 Transition in column 75 of the overall picture: At the four transition points 50, 100, 150 and 200, leaps are present, that means that the transition are not continuous. Especially at the points 100, 150 and 200 the leaps are very clearly visible. In addition the slope at the points 100 and 200 have different signs and switch from positive to negative at the point 100 and the from negative to positive at the point 200. Although the slope at the point 150 is the same before and after the transition, there is a major gap in the functional value. It is a coincidence that at the point 50 the leap is smaller than at the other transition points. 91

- 3.8 Smoothed transition in row 75 of the overall picture: After applying the cosine-bell function on the cross section of the overall picture at $x = 75$, it can easily be seen that at the transition points are smoother than before. Both slopes at each transitions show the same value before and after the transition and it is only left a small leap at the point 200. 91
- 3.9 Final overall picture with smoothed transitions: Finally, after applying the cosine-bell function to all transitions for both x and y direction the final convolved and stitched together picture is shown in figure 3.9. Corresponding to the strelhmap and the 25 single PSF the smoothed final output image shows the expected structure. On the left side of the image, where the Strehl ratio is very low, the single input points are not recognisable. In the middle part the image quality increases and some structures are shown but the results are not conclusive. In the middle right part, the diffraction limited image of the point can clearly be seen. In contrast to the un-smoothened image in figure 3.5 there are less hard edges and the transition points are no longer recognisable. 93
- 3.10 The principle of the cosine-bell-function: Red line: unprocessed original input data Blue line: smoothed, cosine-bell-function applied output data Green line: 1st cosine-function Purple line: 2nd cosine-function Principle: the algorithm goes from left to right. To evaluate the value at each step m over a smoothing width of n , the functional value of the input data (red line) at the point m is multiplied with 1st cosine function at the point m , the value of $(m - n)^{th}$ value is multiplied with 2nd cosine-bell functions at the point $m - n$ and the sum of this both results gives the new output value (blue line) at the point m 94
- 3.11 Low resolution 10" x 10" detail pictures of the Galactic Centre in a resolution of 2000 x 2000 pixel 96

- 3.12 5x5 simulated PSFs with a centered NGS: The 25 PSFs comply with the specification that the NGS is positioned in the centre of the FoV. The central PSF (the 13th or 3rd PSF in 3rd row) shows clearly a diffraction limited structure. The central and the two secondary maxima are clearly distinguishable and the structure is hardly smudged. This observation also applies for the eight directly adjacent PSFs: the diffraction limited structure is also clearly recognisable, whereby the structure is a little more smudged. Also the outer lying PSFs show a central and mostly secondary maxima, but as expected the structures are more smudged. In general, the shown PSFs have a high quality. 98
- 3.13 10" x 10" detail around the Galactic Center in low resolution: The given image show the expected structure: the central part shows detailed structures and the diffraction limited images of the point sources are recognisable. Radial outward going the image quality decreases and although still diffraction limited sources can be seen, these structures are more smeared. 99
- 3.14 10" x 10" detail around the Galactic Centre in higher resolution . . . 100
- 3.15 Convolution with a low resolution picture of the gc (Fig. 3.11) and the PSFs in (3.12): The image quality of the single convolved images is correlated to the PSFs shown in figure 3.12: The image in the centre show detailed structures and single sources are recognisable. This good image quality also applies for the eight directly adjacent images: detailed structures are also given, although the structure in the centre starts to smear. This effect of smearing increases for the outwards images and instead of single sources the centre structure becomes mashed up. 101

- 3.16 Strehlmap corresponding to PSFs in figure 3.12: The Strehl ratio goes up to 90 % in the middle and falls circular to a value of 20 % to 25 %. The strehlmap is extremely symmetric and of very good quality. It must be considered that atmospherical and instrumental effects hardly cause disturbance while imaging through the central arcsecs with a Strehl ration of about 90 %. Although such a good strehlmap is unrealistic under normal observing conditions, convolving the corresponding PSFs with the input image helps understanding the influences of atmospherical and instrumental effects on imaging. 102
- 3.17 10" x 10" detail of the Galactic Centre in high resolution. Fig. 3.14 convolved with Fig. 3.12: Since the PSF quality is extremely good, the convolved image shows in the central part diffraction limited images of single point sources. The output image quality decreases radially outwards. When comparing with the original input picture in 3.14 one can see that although the PSF quality is very good, a lot of details cannot be reconstructed in the convolved output image. 103
- 3.18 Strehlmaps for the 5 different parallactic angles: 1st image (1st image in 1st row): -30.783° 2nd image(2nd image in 1st row): -24.698° 3rd image(3rd image in 1st row): 0° 4th image(1st image in 2nd row): 30.783° 5th image(2nd image in 2nd row): 24.698° 105
- 3.19 Left: Output picture after de-convolving. Right: Input picture of Galactic Center in high resolution with science cases (both: 10" x 10" detail in 2000 x 2000 pixel resolution) The, to be analysed, science cases are marked in figure 4.1 and discussed in chapter 4. Although the single cases are discussed later, one science case (thin dusty filaments, in section 4.3) is marked with a yellow circle in order to show that these structures are still present after the de-convolving process. 106

3.20	Image of the convolved Galactic Centre (10" x 10" detail in 2000 x 2000 pixel resolution). The convolved images of the Galactic Centre are shown for 5 different parallactic angles: 1 st image (1 st image in 1 st row): -30.783° , 2 nd image(2 nd image in 1 st row): -24.698° , 3 rd image(3 rd image in 1 st row): 0° , 4 th image(1 st image in 2 nd row): 30.783° , 5 th image(2 nd image in 2 nd row): 24.698° . The yellow circles show thin dusty filaments (discussed in section 4.3). It can be seen that for each parallactic angle these structures are present, although the image quality differs for the parallactic angles. In the 2 nd and 5 th image the structure is clearly recognisable. The 3 rd image shows this structure, but is more smudged. In the 1 st and 4 th image still a maxima is visible, but is hardly discernible as a linear structure.	107
4.1	Science Cases, 10" x 10" detail around the Galactic Centre: α, β, γ and δ : Proper motions, GC, II, III and IV: small stellar associations, A and B: Thin dusty filaments, a, b, c, d, e, f, g, h and m: disk embedded sources, k: cometary and asymmetric bow-shock sources.	110
4.2	Stripe α . Top: Original Image, Bottem: Re-Convolved Image. Each image shows a detail of 3.6" x 0.1".	111
4.3	Stripe β Left: Original Image, Right: Re-Convolved Image. Each image shows a detail of 0.1" x 4.1"	113
4.4	Stripe γ Left: Original Image, Right: Re-Convolved Image. Each image shows a detail of 0.1" x 5,6"	113
4.5	Stripe δ Left: Original Image, Right: Re-Convolved Image. Each image shows a detail of 0.1" x 5.1"	113
4.6	Mean value for \bar{y} and error Δy in table 4.5 and point coordinates (red circles) in tab. 4.1	113

4.7	Measured point with 1σ -gauss-errors of stripes α , β , γ and δ . Red represents the original points in the input image. Green represents the measured point in the re-convolved image. One can see that in stripe α the position in x-direction is reproduced very well, since the y components vary. This can be seen better in figure 4.7a. For the stripes β , γ and δ it is similar, but in these cases the y-components can be reproduced well and the x-components vary. It is important to mention that although in the input image all points are placed in a line (red line), the linearity can not always be determined. The reason therefore is that in very dense regions the placed points are difficult to find. The gaussian fit is performed for a 10 px x 10 px area around the known position of the input points. In cases where multiple sources are in this area, the gaussian function may fit another source and performs the fit accordingly.	116
a	Stripe α	116
b	Stripe β	116
c	Stripe γ	116
d	Stripe δ	116

- 4.8 Small stellar associations. Left top: Original image of GC. Right top: GC. Middle left: GC III. Middle right: GC II, Bottom left: GC IV. Each image shows a detail of 1" x 1". Like one can see the original picture of the GC is extremely detailed and star clusters can be identified. The GC in the resulting image after de-convolving shows less structures, but the positions of individual sources can still be determined, although the single structures are expatiated. Since GC III is farthest away from the the guiding stars, the image quality drops as expected. Almost none of the sources can clearly be determined. Due to the fact that both, GC II and GC IV are closest to the guiding stars more details can be seen. Nevertheless, in both cases an allocation of structures to the original sources is hardly possible. One can see that the background noise is reduced in all re-convolved images. Halos which can be seen in the original image of the Galactic Center lack completely in the re-convolved images. 119
- 4.9 Linear structure A. Left: Re-convolved image. Right: Original input image. Each image shows a detail of 0.275" x 0.25". As one can see the linearity of the original filaments are recognisable. Since the structure A is closer to guiding stars, more points could be resolved. However, the line structure is broken down to seven more or less separate points, such that the linearity is apparent but does not allow the conclusion that these points are coherent. Also, the individual points are wider than the original line structure width. 121
- 4.10 Linear structure B. Left: Re-convolved image. Right: Original input image. Each image shows a detail of 0.1" x 0.3". As one can see the linearity of the original filaments are recognisable. B is in the re-convolved image reconstructed as a narrow and oblong structure with two separate maxima. Also, the two maxima are wider than the original line structure width. 122

- 4.11 Source a: each image shows a detail of 0.225" x 0.225". The right image shows the original input gaussian source. On the left the re-convolved output source is shown. One can see that the re-convolved image is no longer symmetric, and therefore the fitted gaussian function is narrower than in the original input source. The position determination however is accurate. In the re-convolved image also additional points sources are recognisable. Most likely, these additional structures originate in inaccuracy during the de-convolution process. 124
- 4.12 Source b: each image shows a detail of 0.225" x 0.225". The right image shows the original input gaussian source. On the left the re-convolved output source is shown. The re-convolved image is no longer radially symmetrical and shows two maxima. The gaussian fit matches best on the right maxima. In general, the position determination is accurate but the symmetric form of the input point source is mostly lost during the convolution and re-convolution process. 124
- 4.13 Source c: each image shows a detail of 0.225" x 0.225". The right image shows the original input gaussian source. On the left the re-convolved output source is shown. Since in the input image additional structures around the source point are given, in the re-convoluted image these structures are missing. In general, the radial symmetric form is given in the output image, although there is no longer a single, centre maxima, but two maxima slightly below and above the original maxima of the input image. Above the central structure also small round structure is recognisable. 125

- 4.14 Source d: each image shows a detail of 0.225" x 0.225". The right image shows the original input gaussian source. On the left the re-convolved output source is shown. In the input image, several structures around the central gaussian source are given. These structures are lost in the re-convolved image, which means that detailed structures cannot be reproduced after re-convolution. Although in the output structure the radial symmetric structure of the input source can hardly be seen, the position determination is accurate. 125
- 4.15 Source e: each image shows a detail of 0.225" x 0.225". The right image shows the original input gaussian source. On the left the re-convolved output source is shown. The radial symmetric input source is split up into two separate bigger maxima and two minor maxima. The symmetric structure is hereby no longer recognizable, although the position determination is quite good but varies from the position of the input source. 126
- 4.16 Source f: each image shows a detail of 0.225" x 0.225". The right image shows the original input gaussian source. On the left, the re-convolved output source is shown. The radial symmetric input source is split up into two separate maxima. The central, more dominant maxima show a radial symmetric structure but is much smaller in diameter. This leads to a smaller 1σ -error of the gaussian fit. 126
- 4.17 Source g: each image shows a detail of 0.225" x 0.225". The right image shows the original input gaussian source. On the left, the re-convolved output source is shown. The radial symmetric input source can be reconstructed in the re-convolved image, since the structure is frayed and smaller in diameter. 127

4.18	Source h: each image shows a detail of 0.225" x 0.225". The right image shows the original input gaussian source. On the left, the re-convolved output source is shown. The radial symmetric input source is reconstructed as a more smudged structure, but still a central maxima is recognisable. Around the central maxima several small structures can be seen.	127
4.19	Source k: each image shows a detail of 0.575" x 0.575". The right image shows the original input gaussian source. On the left the re-convolved output source is shown. The input image shows three comet-shaped sources. Since both the three central maxima and the linearity of the three input source can be reproduced, the comet-shaped characteristics can no longer be seen. This shows that observing comet-shaped structures in the Galactic Centre is still a challenge.	128
4.20	Source m: each image shows a detail of 0.225" x 0.225". The right image shows the original input gaussian source. On the left the re-convolved output source is shown. The radial symmetric structure of the input image is split up into three maxima. The major maxima is positioned slightly below the original position and is narrower than the original one.	128
4.21	Position measurement of the three sources k. The red line represents input sources and the green line the position of the re-convolved sources. Both in the input and the re-convolved image the three sources lay on a line. The error bars for the re-convolved sources are smaller due to the fact that the re-convolved structures are narrower than the original ones.	130
4.22	Sum of disk embed sources a, b, c, d, e, f, g, h and m. Detail of 0.2" x 0.2".	131
5.1	Whole FoV divided in 5x5 simulated PSFs with a centred NGS.	137
5.2	Strehlmap corresponding to PSFs in figure 5.1	138

- 5.3 Science Cases, 10" x 10" detail around the Galactic Centre: α, β, γ and δ : Proper motions, GC, II, III and IV: small stellar associations, A and B: Thin dusty filaments, a, b, c, d, e, f, g, h and m: disk embedded sources, k: cometary and asymmetric bow-shock sources. 139
- 5.4 Left: Output picture after de-convolving. Right: Input picture of Galactic Center in high resolution with science cases (both: 10" x 10" detail in 2000 x 2000 pixel resolution). 140

List of Tables

1.1	This table shows the individual Zernike polynomials and their aberrational meaning. The modes are normalised to $\int_0^{2\pi} \int_0^1 Z_j^2 \rho d\rho d\theta = \pi$	45
2.1	This table shows the parameters used to perform the simulations in chapter 4	80
3.1	Optical reference stars.	106
3.2	Simulated parallactic angles.	106
4.1	Point coordinates for stripe α including 1σ -gauss-error.	114
4.2	Point coordinates for stripe β including 1σ -gauss-error.	114
4.3	Point coordinates for stripe γ including 1σ -gauss-error.	115
4.4	Point coordinates for stripe δ including 1σ -gauss-error.	115
4.5	Mean value and errors of stripes α, β, γ and δ	117
4.6	Positions of sources a, b, c, d, e, f, g, h, k and m in the original image and the re-convolved output, including errors in x and y direction.	129
4.7	Slope and intersections of the line fits of the three sources k.	130
4.8	Positions of sources a, b, c, d, e, f, g, h, k and m in original image and re-convolved output including errors in x and y direction.	131
4.9	Mean measuring errors for original and re-constructed image in x- and y-direction in pixel and milliarcseconds	133

List of Abbreviations

AO	Adaptive Optic
CCD	Charge-Coupled Device (detector)
CND	Circus Nuclear Disk
DM	Deformable Mirror
FoV	Field of View
FWHM	Full Width Half Maximum
GC	Galactic Centre
GWS	Groundlayer Wavefront Sensor
IDL	Interactive Data Language
LBT	Large Binocular Telescope
LBTO	Large Binocular Telescope Observatory
LINC	LBT INterferometric CAmera
LOST	Layer Oriented Simulation Tool
mas	milli arcsecond
MCAO	Multi Conjugate Adaptiv Optics
MHWS	Mid-High-Layer Wavefront Sensor
NGS	Natural Guiding Star
NIRVANA	Near-IR/Visible Adaptive iNterferometer for Astronomy
OPD	Optical Path Difference
OTF	Optical Transfer Function
PSF	Point Spread Function
Sgr A*	Sagittarius A*
SH	Shack-Herman (WFS)
SMBH	Super Massiv Black Hole
SR	Strehl Ratio
VLA	Very Large Array

WFS Wave Front Sensor

Introduction

In order to extend our understanding of our universe it is crucial to observe it. These observations allow us to create new hypothesis about the evolution of the stars, galaxies and the whole universe and thus our own history. In the other way around once formulated hypothesis also must withstand observations in order to be verified or repudiated. New hypothesis may result in small variations in the measured value, but possibly have a huge impact on our understanding of our universe. So very precise measurements are essential to extend our knowledge about physical laws (we will come to that). A particularly interesting object of study is our Galactic Centre. We are about 8 kpc away from the Galactic Centre and electromagnetic waves travel almost the whole distance unimpeded. But only almost, since Earth's atmosphere disturbs the arriving wavefronts on the last 100 km and causes uneven and non-parallel wavefronts.

We all know this effect from flicking above hot roads or hot air around plane engines as in figure 1. The same effect takes place when we watch the stars at night. As beautiful as the twinkling of the stars may be, this effect reduces the quality at imaging celestial objects significantly .



Fig. 1: Flickering hot air around jet engines. [Image credit to NASA (2018a), "NASA Armstrong Flight Research Center"]

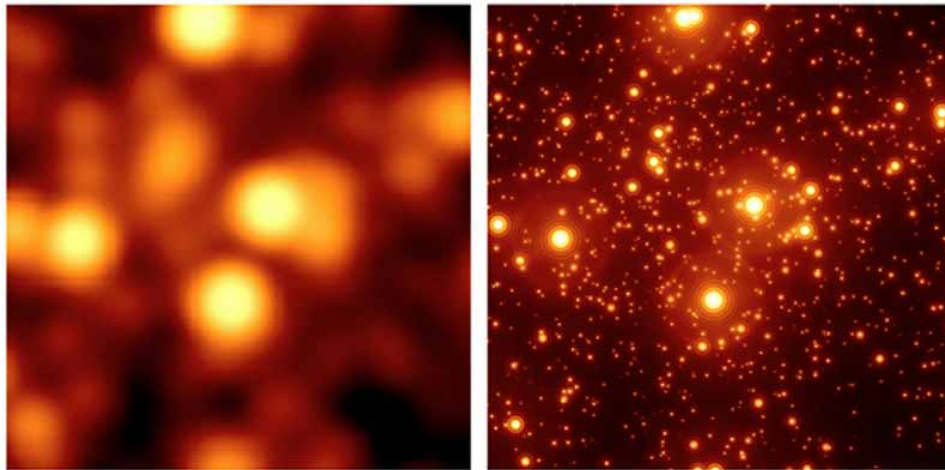


Fig. 2: Left: observation without adaptive optics, Right: observation with adaptive optics, [Image credit to GMT (2018), "Giant Magellan Telescope"]

This thesis deals with these disturbances; not only with their cause and effect, but also with the actions to reduce them, namely adaptive optics. Adaptive optics are capable to smooth and to co-phase incoming wavefronts with adjustable mirrors

which adapt to the uneven wavefront. The potential of this technique can be seen in figure 2.

In order to investigate these corrective effects, certain constellations are simulated. Although such a simulation has a great number of parameters, the main criteria are

- ▶ **From where is observed?** Mount Graham, southeastern Arizona, US
- ▶ **With which telescope is observed?** The large Binocular Telescope
- ▶ **What is observed?** The Galactic Centre

Looping back to precise measurements: What do the limitation of atmospheric disturbances mean for Earth based observations of celestial objects like the Galactic Centre? In other words: How precisely (with which error) are we able to observe our Milky Way?

Answering this question is the main purpose of this thesis.

Theory

In observational astronomy celestial objects are studied by using telescopes. Since the beginning of modern times, optical telescopes are used to observe the sky. The first type of telescopes were refractors, that gathered optical light waves by curved lenses. In figure 1.1 the schematic of a refractor telescope is shown. The light reflected from the object **4**) passes through the entry lens **1**) and is deflected toward the focus point **5**). It must be noted that the image in the focus point is upside down. The light passes through the exit lens **2**) and reaches the eye **3**). The virtual image **6**) is what is seen through the exit lens.

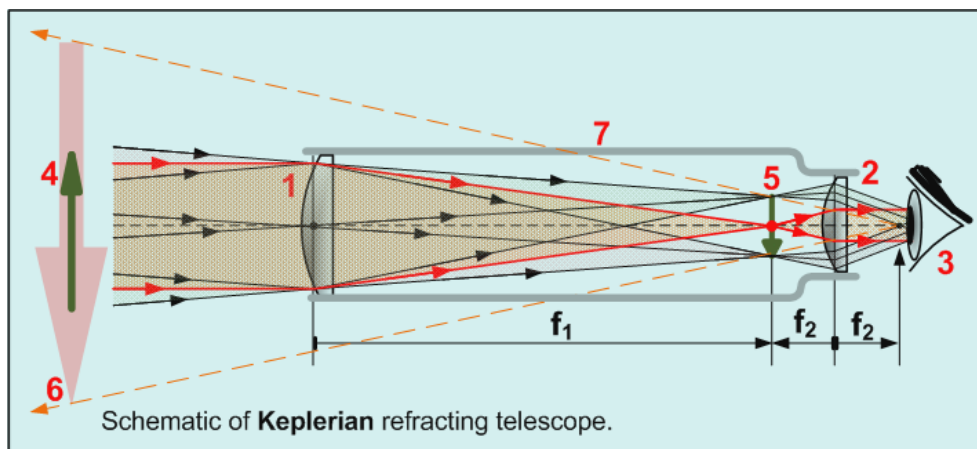


Fig. 1.1: Principle structure of a refracting telescope. (Tamás (2018))

- 1) Front lens
- 2) Rear lens
- 3) Eye
- 4) Original object
- 5) Focus point
- 6) Virtual image

Soon after the first refracting telescopes, reflecting telescopes with parabolic mirrors as gathering element were invented. The advantages of reflecting telescopes compared to refracting telescopes are the reduction of spherical aberrations and the absence of chromatic aberrations. In Fig. 1.2 the schematic of a Newtonian telescope (a special kind of reflecting telescope) is shown. The electromagnetic wave enters through the entry point **a**) and is focused by a concave mirror **b**) towards the secondary mirror **c**) and finally passed through the exit point **d**)

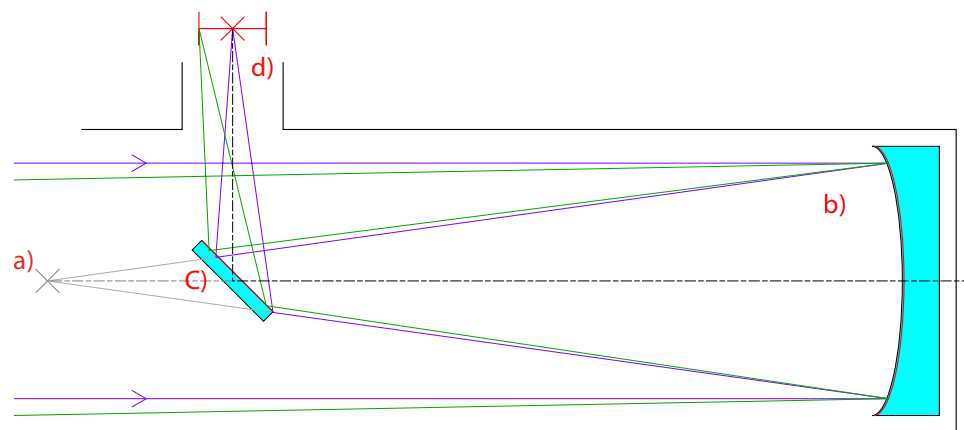


Fig. 1.2: Principle structure of a reflecting telescope:
The electromagnetic wave enters through the entry point **a**) and is focused by concave mirror **b**) towards the plain mirror **c**) and finally passed through the exit point **d**) (Krishnavedala (2018))

Of certain interest for this work are infrared telescopes. Ground based telescopes are limited since water vapour in Earth's atmosphere absorbs infrared radiation. Therefore ground based infrared telescopes are placed in high altitudes and dry weather conditions in order to amplify their performance.

1.1 Astronomical interferometer

Astronomical interferometers are arrays of telescopes which are interconnected by the principle of interferometry to measure fine angular details of electromagnetic sources from outer space. The angular resolution of common earth based telescopes are insufficient for a great number of astronomical cases since the angular resolution and sensitivity is limited by the size of the aperture of the telescope. The

growth of the aperture is limited by practical reasons because the technological barriers of bigger telescopes are not to be underestimated. Measurements of the positions of cosmic objects with sufficient resolution are of immense importance for further progress in astronomy. More accurate measurements allow identification of objects within various ranges of the electromagnetic spectrum. The precise position and the intrinsic movements of celestial objects but also their movement ascribable to Earth's parallax are essential to understand the physics of our universe. Interferometry offers to overcome the limitation of common telescopes. Based on the area of the array of telescopes spanned of an astronomical interferometers, its angular resolution is comparable to a single telescope of the same diameter. The resolution of a single telescope depends on the investigated wavelength λ and the diameter D and scales to $\frac{D}{\lambda}$. The resolution of a two-telescope interferometer scales to $\frac{B}{\lambda}$, where the baseline B is the distance between the two telescopes. The downsides of astronomical interferometers are that they do not collect as many photons as a single telescope of the same size and the maximum angular size of detectable objects are limited by the minimum gap between two telescopes. The biggest challenge in interferometry is to combine the beams in phase after passing the same optical path through Earth's atmosphere, the telescopes and finally to the point where both beams are combined. The accuracy must lie within a few tenth of the wavelength of the observed spectrum at $\lambda = 600\text{nm}$. To achieve this accuracy the interferometer must be mechanical stable, the detectors need a good time resolution and an adaptiv optic to reduce the effects of atmospherical turbulences. (Jankov (2010)).

1.1.1 Van Cittert - Zernike theorem

We assume a source S emits monochrome radiation with a frequency ν which is detected at the point 1 and 2. We also assume the distance d to be $d = (d_1 + d_2)/2$. We can write the electric field as

$$E_A(t) = A_S e^{-2\pi i \nu t} \quad (1.1)$$

where A_S is a complex time-independent amplitude. The electric field is antiproportional to the distance d to S as: $|E| \propto 1/d$. Radiation emitted at S reaches

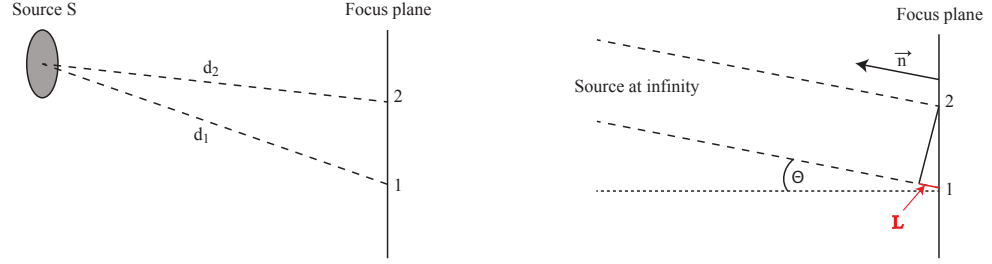


Fig. 1.3: Pictograms for the derivating the van Cittert - Zernike theorem. Left: source S at short distance emitting radiation. Observing points 1 and 2. Right: same setup, but this time the source is moved to a very large distance so that the rays appear parallel.

point 1 with a lag compared to point 2. Therefore, when radiation arrives at point 2 at t , the radiations arrives at point 1 at $t + d_1/c$. One can write the electric field at point 1 as

$$E_1(t) = \frac{\sqrt{\Delta S_S}}{d} A_S e^{-2\pi i \nu (t + d_1/c)} \quad (1.2)$$

where ΔS_S is the surface area of the emitting region S. In equation 1.2 we take $\sqrt{\Delta S_S}$ since we later will integrate over many non-coherent regions and N non-coherent sources increase the amplitude of the electric field by \sqrt{N} . Equation 1.2 can accordingly be written for the observing point 2. The spacial coherence between the observing points 1 and 2 can be written as

$$\langle E_1^*(t) E_2(t) \rangle = \frac{1}{T} \int_0^T \frac{\Delta S_S}{d^2} A_S^* A_S \exp \left[-2\pi i \nu \left(\frac{d_2 - d_1}{c} \right) \right] dt \quad (1.3)$$

In the case $\vec{r}_1 = \vec{r}_2$ the measured flux from S is

$$F = \frac{c}{4\pi} \langle E_1^*(t) E_1(t) \rangle = \frac{c}{4\pi} \frac{\Delta S_S}{d^2} A_S^* A_S \quad (1.4)$$

For the general case $\vec{r}_1 \neq \vec{r}_2$ the arriving rays can be seen as quasi parallel since $d_{1/2} \gg |\vec{r}_2 - \vec{r}_1|$ (figure 1.3, right). The length L in the right part of figure 1.3 is given by $L = d_1 - d_2 = |\vec{r}_2 - \vec{r}_1| \sin \Theta$, where Θ is the angle between the normal of the focus plane and the source S. We can rewrite L with the vector \vec{n} which point from the focus plane towards the source S. We then have

$$d_1 - d_2 = \vec{n} \cdot (\vec{r}_2 - \vec{r}_1) \quad (1.5)$$

With equation 1.5 we can rewrite equation 1.3 to

$$\langle E_1^*(t)E_2(t) \rangle = \frac{\Delta S_S}{d^2} A_S^* A_S \exp \left[-2\pi i \nu \left(\frac{\vec{n} \cdot (\vec{r}_2 - \vec{r}_1)}{c} \right) \right]. \quad (1.6)$$

By defining $\vec{r} \equiv \vec{r}_2 - \vec{r}_1$ and reducing to a 2-D problem by setting $r_z = 0$ we thus get

$$\vec{n} \cdot (\vec{r}_2 - \vec{r}_1) \equiv \vec{n} \cdot \vec{r} = n_x r_x + n_y r_y \quad (1.7)$$

and obtain

$$\langle E_1^*(t)E_2(t) \rangle = \frac{\Delta S_S}{d^2} A_S^* A_S \exp \left[-2\pi i \nu \left(\frac{n_x r_x + n_y r_y}{c} \right) \right]. \quad (1.8)$$

Equation 1.8 applies for a single emitting area S and shows a phase shift of

$$\delta \phi(r_x, r_y) = \nu \frac{n_x r_x + n_y r_y}{c} \quad (1.9)$$

for the points 1 and 2. When integrating equation 1.8 over an entire region, one has to substitute ΔS by

$$dS_a = d^2 n_x dn_y \quad (1.10)$$

and get

$$\langle E_1^*(t)E_2(t) \rangle = \int A^*(n_x, n_y) A(n_x, n_y) \exp \left[-2\pi i \nu \left(\frac{n_x r_x + n_y r_y}{c} \right) \right] dn_x dn_y. \quad (1.11)$$

Equation 1.11 is a 2-D Fourier integral with r_x/λ and r_y/λ . The Fourier transformed integrand $A^*(n_x, n_y)A(n_x, n_y)$ is the intensity $I(n_x, n_y)$.

The Fourier transformed image of the observed source is thus the correlation between the observing points 1 and 2.

1.1.2 Fizeau interferometer

In order to obtain the benefits of multiple telescopes, their beams must be coherently combined. At the common focus point, the interferometric signal can be detected. This interferometric pattern is called *fringe*. In general there are two possible combination points for the fringes:

► Pupil plane (Michelson mode)

In the Michelson mode, the ratio of aperture diameter and separation is not constant. The reason therefore is that the diameter of the combined beams stays the same from the exit point of the telescope to the recombination lens. The consequence is that the image is not a convolution of the object. The field of view of Michelson interferometers is narrower than for Fizeau interferometers.

► Image plane (Fizeau mode)

In the Fizeau mode, the ratio of aperture diameter and separation is constant from the exit point of the telescope and the focus plane. This state is called homothetic pupil condition (see fig. 1.4). The advantage of Fizeau mode compared to Michelson mode is the wider field of view.

The fringe pattern in the point where both beams are combined can be described:

$$I = I_1 + I_2 + 2\sqrt{I_1 I_2} |\gamma_{12}| \cos\left(\frac{2\pi P}{\lambda} - \phi\right), \quad (1.12)$$

where I_1 and I_2 are the intensities of the fields each telescope observes. It must be noted that equation 1.12 assumes coherent or at least quasi coherent part fields, which is the case for sources at large distances (van Cittert-Zernike theorem). P is the optical path length difference of each field to the point of interference. $|\gamma_{12}|$ is the normalized complex degree of spatial coherence. It depends on the brightness distribution of the source $B(\alpha, \delta)$. By measuring the degree of coherence at different points on the image plain, the brightness distribution of the source can be reconstructed. The van Cittert-Zernike theorem states (see section 1.1.1):

$$|\mathcal{F}(B(\alpha, \delta))| = |\gamma_{12}|. \quad (1.13)$$

The left side of equation 1.13 states the modulus of the normalized spatial Fourier transformation of the brightness distribution of the plane.

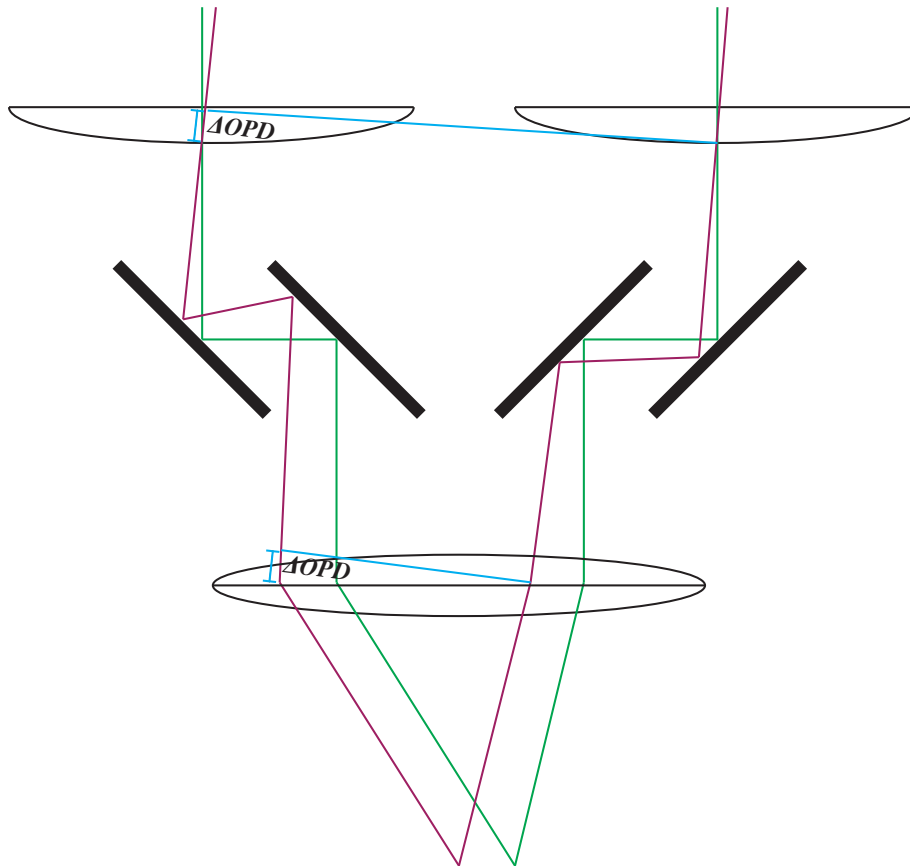


Fig. 1.4: Homothetic pupil condition

Fizeau's idea was to place a plate with two holes in the beam path of a telescope. So the telescope becomes a beam combiner for the two sub-beams. By this procedure the brightness distribution of the source can be determined, but of course there is no extension of the field of view (FoV) nor sensitivity. To achieve this goal multiple telescopes must be combined. It is most important that non-axis sub-beams have no optical-path-differences (OPD), so that the combined beam appears to be from one single telescope (Traub (1986)). This condition is fulfilled when the input and exit pupils of each sub-optic are scaled versions of each other.

Fizeau's idea was to place a plate with two holes in the beam path of a tele-

scope. So the telescope becomes a beam combiner for the two sub-beams. By this procedure the brightness distribution of the source can be determined, but of course there is no extension of the FoV nor sensitivity. To achieve this goal multiple telescopes must be combined. It is most important that non-axis sub-beams have no optical-path-differences (OPD), so that the combined beam appears to be from one single telescope (Traub (1986)). This condition is fulfilled when the input and exit pupils of each sub-optic are scaled versions of each other. This homothetic pupil condition is illustrated in figure 1.4.

1.1.3 Telescope point spread function

Distant stars appear as point sources at the sky. When observing these point sources with telescopes, the result is not a point like image. The reason therefore is diffraction in the telescopes aperture. Atmospheric turbulences and aberration amplify this effect by distorting the image. The diffraction is reciprocally to the size of the aperture: the bigger the aperture is, the smaller is the diffraction. The structure of the diffractions is given by the point spread function (PSF) of the telescope and has the form shown in the fig. 1.5. Both, atmospheric turbulences and aberration, will cause broadening and distorting of the PSF. In absence of atmospheric turbulences and aberration the PSF of the telescope is the diffraction-limited and ideal PSF. The diffraction-limited PSF gives the maximum angular resolution. This is the minimum angular separation of equally bright objects that can be detected under perfect conditions. This is a fundamental limit depending on the observed wavelength λ and the diameter D_0 of the telescope and cannot be undercut. The minimum angular resolution is

$$\alpha_C = 1.22 \frac{\lambda}{D_0} \quad (1.14)$$

α_C is known as Rayleigh criterion.

1.2 Atmospheric turbulences

The light emitted by astronomical objects travels mostly unimpeded over several lightyears. The wavefronts of these lights can be considered as perfectly

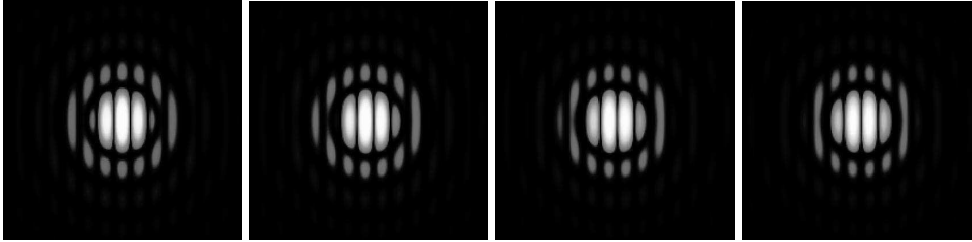


Fig. 1.5: LINC-NIRVANA PSF for four optical path distances: 0 , $\frac{1}{3}\pi$, $\frac{2}{3}\pi$, π from left to right.(Kürster (2010))

plane. These conditions state until the wavefronts reach Earth's atmosphere. Air at 0°C and 1 bar has at optical wavelength a refraction index of approximately $n = 1.00029$, thus is very close to 1 and nearly perfect. But Earth's atmosphere is fluctuating regarding temperature, pressure and density. These fluctuations are both temporarily and spatially but always subsonic. It can be assumed to a very high degree that the velocity fields are non divergent. Therefore atmospherical turbulences are caused by solenoidal motions. By traveling through this inhomogeneous conditions the light respectively its wavefront gets distorted. The fluctuations in the atmosphere's parameters result in variation of the refractive index. So light traveling through the atmosphere in order to reach ground based observatories experiences optical aberration. This again leads to different effects when the radiation of a celestial object reach Earth's surface. On the one hand these distortions cause multiple copies of the stars which are close together. This effect is called *speckles*. On the other hand they cause slight variations in the appearing brightness of the object, called *scintillation*. The latter effect can be observed as twinkling of the stars at night.

The reason for atmospherical turbulences are

- ▶ *Wind around the observing spot:*
Wind flowing over the telescope dome can cause turbulences.
- ▶ *Wind shear:*
Earth's atmosphere consists of different layers. Each layer can have a different horizontal velocity. The gradient of the horizontal velocity can be described as dv_x/dz and if the gradient is big, this can lead to turbulent layers.

In this context the *Richardson number* Ri plays a significant role. If

$$Ri = \frac{g}{\Delta h \cdot (dv_x/dz)^2} \quad (1.15)$$

with g as gravitational acceleration and Δh as altitude difference between two adjacent atmospherical layers, is $\gg 1$, than turbulences occur.

► *Convection:*

Warm air rises due to lower density. When lower levels of the atmosphere head up convectively instability can occur. Then warmer air bubbles rise in higher altitudes. These bubbles can lead to clouds and some even to thunder storms. In smaller scales these bubbles lead to *seeing*.

1.2.1 Fluctuation of refraction index

Due to its inhomogeneous conditions Earth's atmosphere can be described as a turbulent medium. The critical parameter here is the refractive index which depends on both temperature T and pressure p and can be described like in Cox (2015):

$$n_1 \simeq n - 1 \approx 7.76 \cdot 10^{-5} \frac{p}{T} \quad (1.16)$$

where p has the unit mbar and T is given in Kelvin. Equation 1.16 shows that the main reason for the distribution of the refractive index are the changing conditions of temperature and pressure within the atmosphere. Note that solenoidal¹ turbulences per se do not influence the observation at all. Only differences in temperature and pressure among the different layers initiate fluctuations in the refraction index and hereby *seeing*.

It is necessary to describe this spacial and temporal fluctuations statistically. Kolmogorov (1941) gave a very simple description for this distribution. Kinetic energy is introduced into in the turbulent flow at large scales L_0 and splits into smaller and smaller spacial scales and finally is converted into heat, when the eddies reach a critical scale length of l_0 . Within this range, the turbulent flow can be considered as homogenous and isotropic eddies. The boundaries between these eddies have

¹Solenoidal means in this context, that the turbulences have no compressional components

smooth transitions in order to prevent discontinuities.

The spacial power spectral density $\Phi_n(\vec{k})$ describes in equation 1.17 the statistical distribution of the size and the number of these eddies like described in Bertram (2007). An extension to the Kolmogorov model is the Karmen model, which describes the spacial power spectral density $\Phi_n^V(\vec{k})$ as

$$\Phi_n^V(\vec{k}) = \frac{0.033C_n^2}{(\kappa^2 + \kappa_0^2)^{11/6}} \cdot \exp\left(-\frac{\kappa^2}{\kappa_m^2}\right) \quad (1.17)$$

where for the he spacial wave number $\kappa = \frac{2\pi}{l}$ applies $\frac{2\pi}{L_0} \leq \kappa \leq \frac{2\pi}{l_0}$. C_n^2 is the refractive index structure function, which is different for each observatory site. The C_n^2 profile of Mt. Graham is shown in figure 1.6.

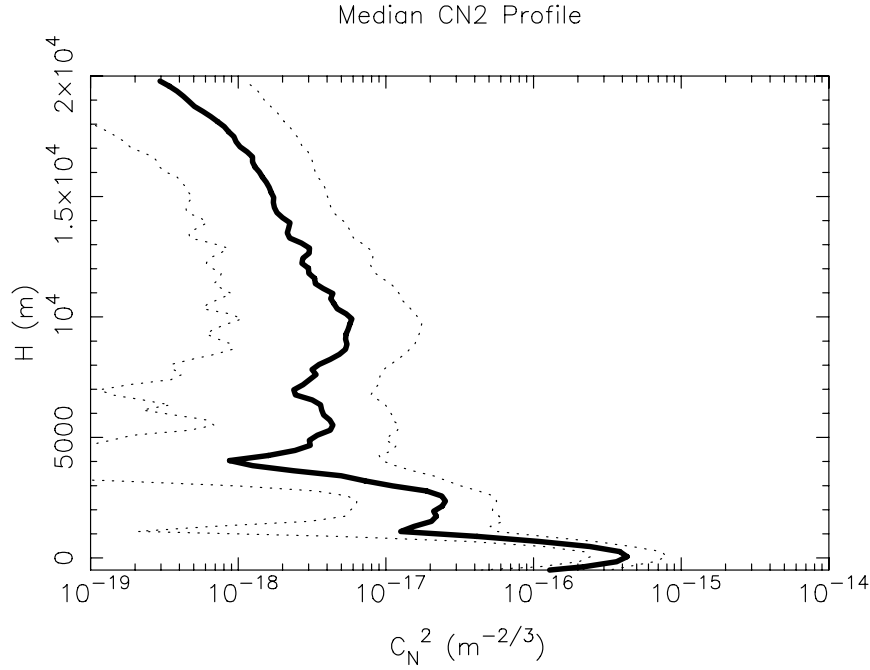


Fig. 1.6: C_n^2 profile for Mt. Graham [Masciadri et al. (2010)]

It is most important to understand the variation of the refraction index between two spatially separated points in order to handle the wave propagation through the atmosphere. The variance of the refraction index n between two points \vec{r}_0 and \vec{r}_1 is

defined as:

$$D_n(r) = \langle |n(\vec{r}_0 + \vec{r}_1) - n(\vec{r}_0)| \rangle. \quad (1.18)$$

Equation 1.18 is called the refraction index structure function and it can be shown that by assuming Kolmogorov statistics it results in:

$$D_n(r) = C_n^2 \cdot r^{2/3} \quad (1.19)$$

The variation of the refraction index in the atmosphere causes an immediate perturbation of the wavefront which travels through. The emitted wavefront from the distant astronomical source can be assumed as plane before it passes our atmosphere. In order to simulate the perturbation of the wavefront we assume a discrete number of atmospheric layers. Furthermore we assume that each atmospheric layer i has a constant $C_{n_i}^2$ with the altitude z_i and the thickness Δz . The vector $\Delta \vec{x}$ represents the separation of two points in a plane perpendicular to the direction of the propagation. $u_i(x)$ is the complex optical field in the i th layer. The spatial correlation function is given by

$$\Gamma(\Delta \vec{x}) = \langle u_i(\vec{x}) u_i^*(\vec{x} - \Delta \vec{x}) \rangle = \exp \left[-\frac{1}{2} D_{\Psi_i}(\Delta \vec{x}) \right] \quad (1.20)$$

where $D_{\Psi_i}(\Delta \vec{x})$ is the phase structure function

$$D_{\Psi_i}(\Delta \vec{x}) = \left\langle k^2 \left(\int_{z_i}^{z_i + \Delta z_i} dz [n_1(\vec{x}, z) - n_1(\vec{x} - \Delta \vec{x}, z)] \right)^2 \right\rangle \quad (1.21)$$

and k the optical wave number. It can be shown, assuming Kolmogorov statistics and that the thickness of each i th layer is much larger than $|\Delta \vec{x}|$, that the phase structure function can be written as (Fried (1966))

$$D_{\Psi_i}(\Delta \vec{x}) = 2.91 k^2 \Delta z_i C_{n_i}^2 |\Delta \vec{x}|^{5/3}. \quad (1.22)$$

Fried (1966) defined r_0 as diameter of an area in which the phase error is not more than ~ 1 rad.

$$\begin{aligned}
r_0 &= 0.185 \left(\frac{4\pi^2}{k^2 \sum_{i=1}^N C_{n_i}^2 \Delta z_i} \right)^{3/5} \\
&= \left(0.423 k^2 \sec \gamma \int C_n^2(z) dz \right)^{-3/5}.
\end{aligned} \tag{1.23}$$

In order to obtain the same angular resolution when observing an object in long exposure, one would need a telescope with the diameter of r_0 . The dependency between the Fried parameter and the wavelength is

$$r_0 \propto \lambda^{6/5}. \tag{1.24}$$

This leads to the image size (also known as *seeing disc* or *seeing PSF*) of

$$\alpha_{seeing} \propto \frac{\lambda}{r_0} \propto \frac{1}{\lambda^5}. \tag{1.25}$$

Equation 1.25 shows that the seeing PSF loses significance compared to the diffraction limited PSF for longer wavelength.

With the Fried parameter follows for the phase structure function $D_{\Psi_i}(\Delta \vec{x})$

$$D_{\Psi_i}(\Delta \vec{x}) = 6.88 \left(\frac{|\Delta \vec{x}|}{r_0} \right)^{5/3} \tag{1.26}$$

and for the total spatial correlation function $\Gamma(\Delta \vec{x})$

$$\Gamma(\Delta \vec{x}) = \exp \left[-3.44 \left(\frac{|\Delta \vec{x}|}{r_0} \right)^{5/3} \right]. \tag{1.27}$$

Without turbulences then is $\Gamma(\Delta \vec{x}) = 1$.

1.2.2 Strehl ratio

The obtained image $I(\vec{r})$ in the focus plane contains both the real image of the observed celestial $I_0(\vec{r})$ object and the aberrations caused by atmospheric disturbances and the telescope. These aberrations can be described by the point spread function (PSF)

$$I(\vec{r}) = I_0(\vec{r}) \odot \text{PSF} \quad (1.28)$$

where the symbol \odot represents a convolution. The Fourier transformed of the PSF is called the optical transfer function (OTF)

$$\mathcal{F}(\text{PSF}) = \text{OTF} \quad (1.29)$$

The OTF includes like the PSF the aberrations from both atmospherical disturbances OTF_A and the telescope OTF_T and can be written as

$$\text{OTF} = \text{OTF}_A \cdot \text{OTF}_T. \quad (1.30)$$

The optical performance of a telescope is measured in the Strehl ratio S . The Strehl ratio is the quotient of the peak value of the measured PSF and the peak value the theoretical PSF_T (see chapter 1.1.3)

$$S = \frac{\text{PSF}}{\text{PSF}_T}. \quad (1.31)$$

This ratio gives information about how much intensity a point source loses through "smearing" compared to a perfect diffraction limited optic. That means a perfect optical system would have the Strehl ratio of 1. A normal (not corrected) ground based telescope reaches a Strehl ratio of about 1% under seeing conditions. The Strehl ratio of an ao system can reach up to 70%.

1.2.3 Resolving power

The telescope transfer function $T(\vec{f})$ is defined as

$$T(\vec{f}) = \int P(\vec{u})P * (\vec{u} + \vec{f})d\vec{u} \quad (1.32)$$

with the aperture function $P(\vec{u})$, $\vec{u} = \vec{x}/\lambda$ and $\vec{f} = \vec{r}/\lambda$. The resolving power is defined as

$$R = \int \Gamma(\vec{f})T(\vec{f})d\vec{f}. \quad (1.33)$$

For the turbulence free case follows for a circular aperture

$$R_{\text{diffract}} = \frac{\pi}{4} \left(\frac{D}{\lambda} \right)^2. \quad (1.34)$$

Equation 1.34 shows the optimum case where resolving power depends on the square of the telescope diameter D^2 and the inverse square of the observed wavelength $1/\lambda^2$. For strong turbulences T equals 1 and for equation 1.33 follows

$$R_{\text{turb}} = \frac{\pi}{4} \left(\frac{r_0}{\lambda} \right)^2 \quad (1.35)$$

with Fried parameter r_0 from equation 1.23.

1.2.4 Phasevariation

The variance of the phase variation between two points is given by phase structure function $D_{\Psi_i}(\Delta\vec{x})$. The standard deviation between two specific points (distance B) σ_{Ψ} where the interferometer is formed by the specific aperture of this given by

$$\sigma_{\Psi} = \sqrt{D_{\Psi_i}(\Delta\vec{x})} = 2.62 \left(\frac{B}{r_0} \right)^{5/6}. \quad (1.36)$$

1.2.5 Zernike modes

In order to describe the distortions of the wavefront, its phase is qualified by a set of orthogonal functions, most common in Zernike polynomials:

$$\psi(D, \rho, \theta) = \sum_j c_j \cdot Z_j(\rho, \theta) \quad (1.37)$$

with

$$Z_j(\rho, \theta) = \begin{cases} \sqrt{n+1} R_n^0(\rho) & \text{if } m \geq 0, \\ \sqrt{n+1} R_n^m(\rho) \sqrt{2} \cos(m\theta) & \text{if } m \text{ is even,} \\ \sqrt{n+1} R_n^m(\rho) \sqrt{2} \sin(m\theta) & \text{if } m \text{ is odd,} \end{cases} \quad (1.38)$$

The radial polynomials are defined as

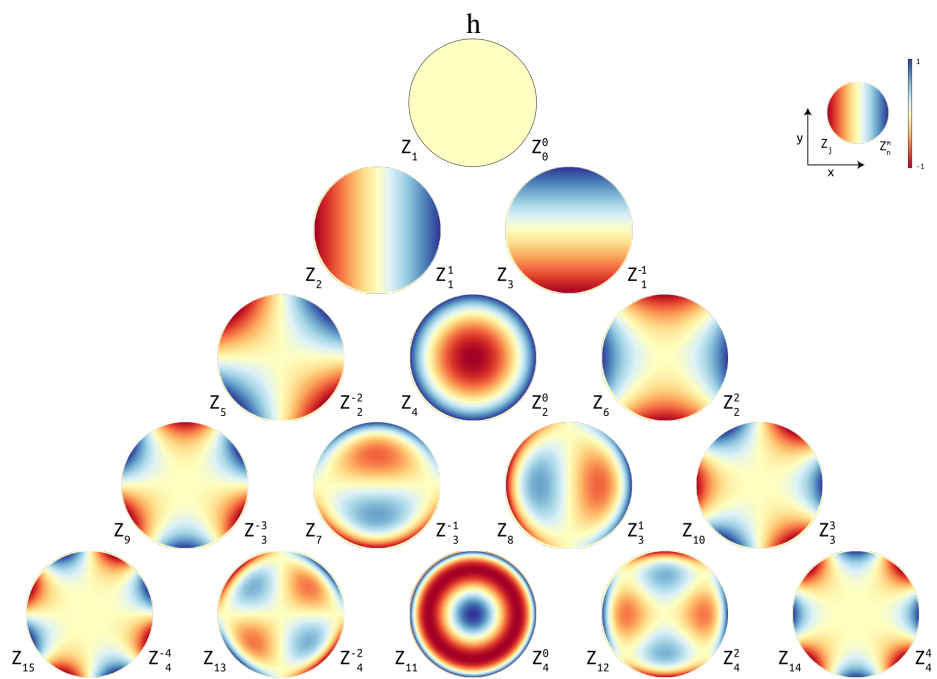


Fig. 1.7: First 15 Zernike polynomials. Vertically ordered by radial degree and horizontally ordered by azimuthal degree. [2pem Wikipedia (2015)]

Tab. 1.1: This table shows the individual Zernike polynomials and their aberrational meaning. The modes are normalised to $\int_0^{2\pi} \int_0^1 Z_j^2 \rho d\rho d\theta = \pi$

Zernike polynomials	Z_j	Classification
Z_0^0	1	Piston
Z_1^{-1}	$2\rho \sin \theta$	Vertical tilt
Z_1^1	$2\rho \cos \theta$	Horizontal tilt
Z_2^{-2}	$\sqrt{6}\rho^2 \sin 2\theta$	Oblique astigmatism
Z_0^{-2}	$\sqrt{3}(2\rho^2 - 1)$	Defocus
Z_2^2	$\sqrt{6}\rho^2 \cos 2\theta$	Vertical astigmatism
Z_3^{-3}	$\sqrt{8}\rho^3 \sin 3\theta$	Vertical trefoil
Z_3^{-1}	$\sqrt{8}(3\rho^3 - 2\rho) \sin \theta$	Vertical coma
Z_3^1	$\sqrt{8}(3\rho^3 - 2\rho) \cos \theta$	Horizontal coma
Z_3^3	$\sqrt{8}\rho^3 \cos 3\theta$	Oblique trefoil
Z_4^{-4}	$\sqrt{10}\rho^4 \sin 4\theta$	Oblique quadrafoil
Z_4^{-2}	$\sqrt{10}(4\rho^4 - 3\rho^2) \sin 2\theta$	Oblique secondary astigmatism
Z_4^0	$\sqrt{5}(6\rho^4 - 6\rho^2 + 1)$	Primary spherical
Z_4^2	$\sqrt{10}(4\rho^4 - 3\rho^2) \cos 2\theta$	Vertical secondary astigmatism
Z_4^4	$\sqrt{10}\rho^4 \cos 4\theta$	Vertical quadrafoil

$$R_n^m = \sum_s^{\frac{n-m}{2}} (-1)^s \frac{(n-s)!}{s! \left(\frac{n+m}{2} - s\right)! \left(\frac{n-m}{2} - s\right)!} \rho^{n-2s}. \quad (1.39)$$

The different orders of Zernik polynomials can be seen as optical monochrome aberrations. The first two orders are associated with the tip and tilt of the wavefront. The next higher modes represent for example defocus and spherical aberration. The 0th Zernike order is called the piston mode and stands for the general phase shift of the wavefront. The few first Zernike modes are listed in table 1.1.

1.2.6 Astronomical seeing

Astronomical seeing describes in general the effects of blurring or twinkling of astronomical objects caused by fluctuations of the refraction index which again are

caused by turbulences in Earth's atmosphere.

Seeing refers to best angular resolution of an optical telescope at long exposures and is measured by the FWHM (full width at half maximum) of the intensity of the PSF (point spread function). The best seeing that can be achieved for ground based telescopes is about 1 arcseconds. In order to overcome this insufficiency of the angular resolution adaptive optics (see section 1.3) are applied, which improve the resolution to about 0.4 arcseconds. Beside FWHM, there are two other methods of measuring of seeing: the C_n^2 -profile and the r_0/t_0 -measurement.

► C_n^2 -profile

The C_n^2 -profile describes the turbulence strength according to the altitude (see Figure 1.6).

► r_0/t_0

Astronomical seeing can be described by the parameters r_0 (Fried parameter, see 1.26) and t_0 .

For telescopes with diameter D smaller than r_0 applies for FWHM:

$$\text{FWHM} = \frac{\lambda}{D}. \quad (1.40)$$

If r_0 is smaller than the diameter of the telescope the following equation applies:

$$\text{FWHM} = \frac{\lambda}{r_0}. \quad (1.41)$$

On good weather conditions the Fried parameter can reach 10cm to 20cm. Over water typical values for r_0 are about 5 cm. The Fried parameter t_0 can be determined to

$$t_0 \approx \frac{0.3r_0}{\bar{v}_0} \quad (1.42)$$

where \bar{v}_0 is the average wind speed. t_0 is the typical time scale in which atmospheric disturbances do not affect the image.

Seeing has several effects on imaging of astronomical objects. Where in the absence of atmosphere, a point source (like a star) would create a steady airy pattern picture, the atmospheric turbulences cause speckle patterns, which change rapidly. This rapid changing of speckle patterns cause blurring in the images. Also the brightness of the observed object appears to fluctuate. This circumstance is called scintillation. The fringes in an astronomical interferometer also move very fast.

1.3 Adaptive optics

In order to observe astronomical object through Earth's atmosphere over a longer period of time, the perturbation of the incoming phases must be actively compensated by an adaptive optic (AO) system before it reaches the detector. AOs are used both in single telescopes as well as in telescope arrays. A speciality of an AO system is the fringe tracking (see 1.3.2).

Each wavefront perturbation can be represented by as superposition of discrete Zernike modes. The basic idea of AO systems is to compensate the perturbation of the wavefront by deformable mirrors (DMs), which are shaped like the perturbation itself. The adjustments of the DMs must be faster than the characteristic timescale on which the atmospheric disturbances take place. The number of actuators, which form the shape of the DM, limits the number of the Zernike modes that can be corrected. The number of actuators should be round about the number of Fried cells in the aperture:

$$N \approx \left(\frac{D}{r_0}\right)^2. \quad (1.43)$$

1.3.1 Phase reference

In order to correct the phase perturbation, the wavefront sensor needs a phase reference. In general this phase reference is a natural guide star. The reference target must match certain conditions like apparent magnitude and distance to the object of interest. The amount of received photons must match the required sampling

rate of the wavefront sensor. The angular separation between the reference and the observed targets must not be bigger than the isoplanatic angle θ_0 :

$$\theta_0 = 0.0581\lambda^{5/6} \left[\int dz C_n^2(z) \cdot z^{5/3} \right]. \quad (1.44)$$

For two objects within the isoplanatic angle θ_0 , their phase decorrelation is smaller than 1 rad^2 (Fried (1982)).

1.3.2 Fringe tracking

The great advantage of interferometers is that the light of the observed object can be probed in multiple apertures. In each aperture the corresponding segment of the wavefront is smoothed by a separate AO system. It is necessary to combine this segment coherently, but, in general, between each wavefront segment there is a path length difference (OPD). Before coherent combination of the wavefront segments can take place the difference between the piston values (differential piston) must be eliminated. There are two main reasons for differential pistons: atmospheric and instrumental.

► Atmospheric differential piston

Adaptive optical systems are able to reduce atmospheric disturbances. However, the 0th Zernike mode (piston mode, J=1) cannot be tracked by the sensors. The piston mode has no effect on single apertures but very well on multiple apertures. When there is more than one aperture, the light of these are directed to one optical lab where they interfere. The differential atmospheric piston now describes the effect of the turbulent atmosphere on the difference in the piston mode between the multiple apertures. These differences result from different refraction indices in the atmosphere and thus different travel speeds of the electromagnetic wave front.

► Instrumental differential piston

The length of single apertures are usually not exactly the same. This alone could cause OPD. But there are more reasons why instrumental differential piston can occur. For instance, misalignment, vibration, flexure and imperfectly operating AO systems can cause instrumental-made OPDs.

The fringe tracking system which is used in LBT (see section 1.8) is based on the cophasing concept. The differential piston is permanently corrected in order to remain zero. This is performed by a piston mirror that, by moving up and down, adjusts the relative OPD between the wavefront sections, which shall be coherently combined. With other words, the fringe tracking system deals with the Zernike mode $J=1$, which has no importance in single apertures but in multiple apertures.

1.4 Galactic center



Fig. 1.8: Galactic center, combined in optical, infrared and X-Ray domains [Image credit to NASA (2018b), "NASA/CXC/SAO"]

Like described in Eckart et al. (2005) the galactic center is only 8 kpc away from Earth and hosts a massive black hole Sagittarius A* of 3 to 4 million solar masses (M_{\odot}) at the central parsec. It is surrounded by a clumpy circum nuclear disk (CND) of $10^4 M_{\odot}$ with an average density of $10^4 - 10^7 \text{ cm}^{-3}$ and temperature of several hundred Kelvin. The extension of the CND goes from 1.5 parsecs to approximately 7 parsecs from the center. Streams of gas and dust ("mini-spiral") are infalling spirally towards the center. These mini-spirals are most intense and brightest thermal radio source of Sagittarius A*.

At a distance of more than 0.5 parsecs the star distribution follows isothermal conditions. At a distance of 0.39 parsec the stellar density flattens out. This indicates a radius of the central core of 0.34 ± 0.20 parsecs. The scale of the nuclear cluster is about 0.7 parsecs and within 0.1 parsecs there is a peak at the stellar density.

At a distance of a few arcseconds from the center most of the observed luminosity (about 9 to 12 magnitudes in K-band) is produced by about 20 massive, bright blue stars. Their surface temperature lies at about 20000 to 30000 Kelvin. They probably arose of a star formation episode between 3 to 7 million years ago.

Near infrared images are also dominated by intermediate bright late-type stars (about 10 to 13 magnitudes in K-band) whose formation was about 100 million years ago.

Within 0.39 parsecs stars with magnitudes of 14 to 15 in K-band can be found. These stars have high motion velocity of about $1000 \frac{km}{s}$ and even seem to accelerate.

At the center of the stellar cluster Sagittarius A* is located and is perceivable by its radio, infrared and X-ray emissions. Its diameter is about 2.4×10^{13} cm and corresponds to the scale of the Earth's orbit around the Sun.

Due to the gas and dust that surrounds the Milky Way, the GC is not directly observable at optical or ultraviolet wavelength but rather in radio, infrared and X-ray wavelength.

In order to understand the processes in our Milky Way or the behavior of Sagittarius A*, we need to observe the radio, infrared and X-Ray wavelength in the highest possible resolution. In order to achieve this goal, there are different observing methods for each wavelength.

1.4.1 Observing techniques

Usually the common technique for detecting electromagnetic radiation is *heterodyning*. Two frequencies which are created by nonlinear combining two different frequencies f_1 and f_2 are called heterodynes. In general, one combination is the sum of $f_1 + f_2$ and the other one is the difference $f_1 - f_2$. Using heterodynes the incoming signals are transformed from one frequency range to another. The device

used to combine the two frequencies f_1 and f_2 is called the *mixer*.

Optical frequencies change to rapidly too be detectable and processable directly by conventional electronics. But in the domain of visible or infrared light, typically the compared frequencies are so similar that the difference of them can be processed by conventional electronics. This is the main purpose of heterodyning: shifting frequency domains from non-tractable frequencies to tractable frequencies.

The mathematical principle of heterodyning is based on

$$\sin(f_1) \cdot \sin(f_2) = \frac{1}{2} \cos(f_1 - f_2) - \frac{1}{2} \cos(f_1 + f_2). \quad (1.45)$$

The left side of the equation 1.45 represents the *mixing* of the two frequencies and the right side the sum respectively the difference of the incoming frequencies. The main advantage of heterodyning, besides shifting the signal frequency to a tractable domain, is that the mixed signal in general has a larger amplitude than the original signals. Furthermore, by heterodyning, the optical phase is preserved other than by pure intensity measurements. Another advantage is that since the difference frequency is in another domain than the original detected frequencies, is that the noise effect to the measurement can be decreased.

1.4.2 Radio wavelength

Besides optical wavelengths only the radiation of celestial radio sources can reach Earth ground. Frequencies lower than $f \sim 10$ MHz cannot be detected with ground based telescopes because wavelength bigger than $\lambda \sim 30$ m are reflected by Earth's ionosphere. Radiation at wavelength below $\lambda \sim 30$ m respectively frequencies higher than $f \sim 60$ GHz are mostly absorbed by Earth's atmosphere. Frequencies higher than $f \sim 1$ THz cannot penetrate Earth's atmosphere at all.

Radio radiation was found in the early 1930s, when the first radio antenna were build. These antennas received noise signals which varied on a daily time scale. Later it was found that those noises originated from the direction of the Galactic Center. Nowadays we are aware that the source for the radio radiation at the Galactic Center is a black hole.

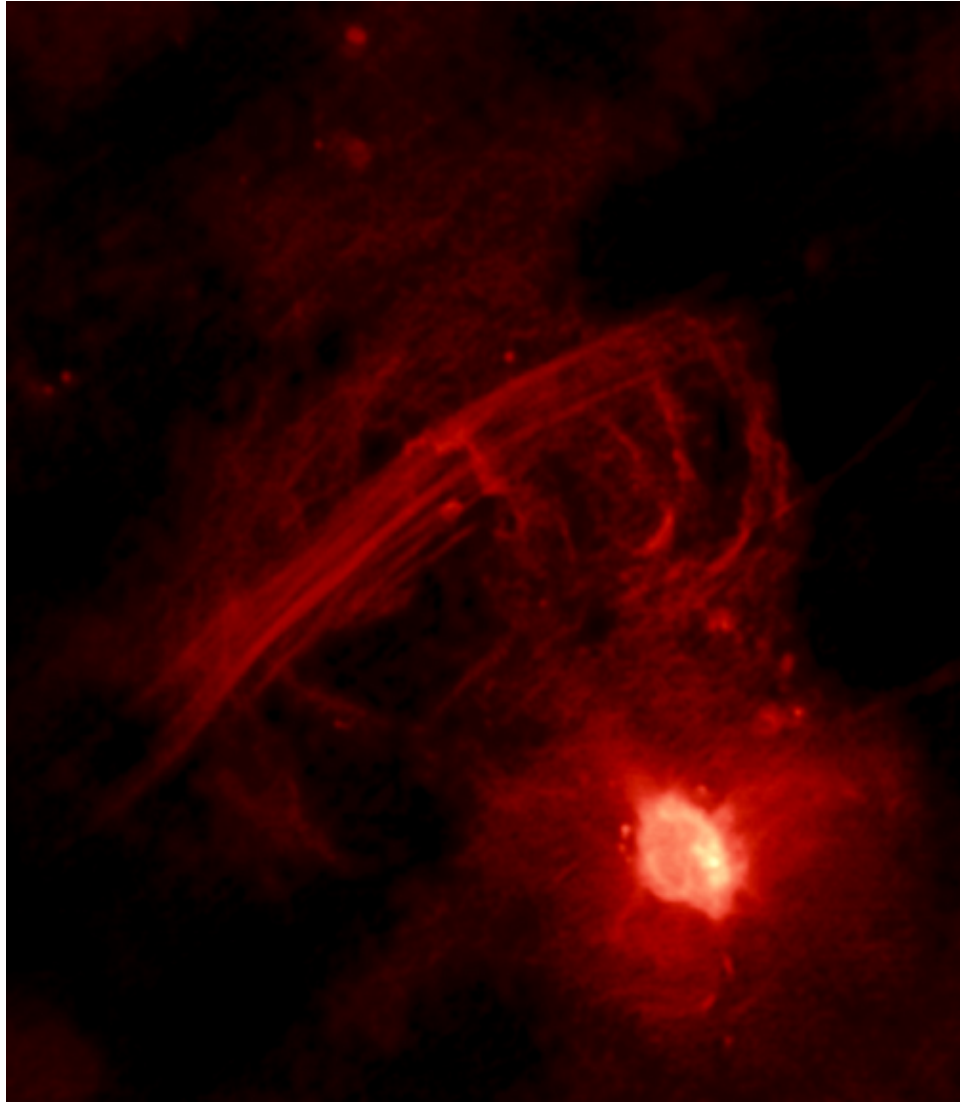


Fig. 1.9: Galactic center in radio domain. The bright object in the lower right part is Sgr A*. [Image credit to NASA (2018b), "NASA/CXC/SAO"]

For the investigation of the structure of the Galactic Center on the angular scale of few arcseconds, the radio interferometry is absolutely necessary. The angular resolution A is proportional to the quotient of the observed wavelength λ and the parabolic mirror diameter d . For present-day detectors, that means a resolution of round about 10 arcseconds. In order to increase the angular resolution, several

mirrors can be combined. In this case the diameter of each mirror is no longer the limitation for the angular resolution, but the baseline B of the mirror array. Such a combined array is for example the Very Large Array VLA ((Eckart et al. 2005, P.4)) with up to 27 antennas. At these wave very high-energy physical processes can be detected.

1.4.3 Far-infrared wavelength

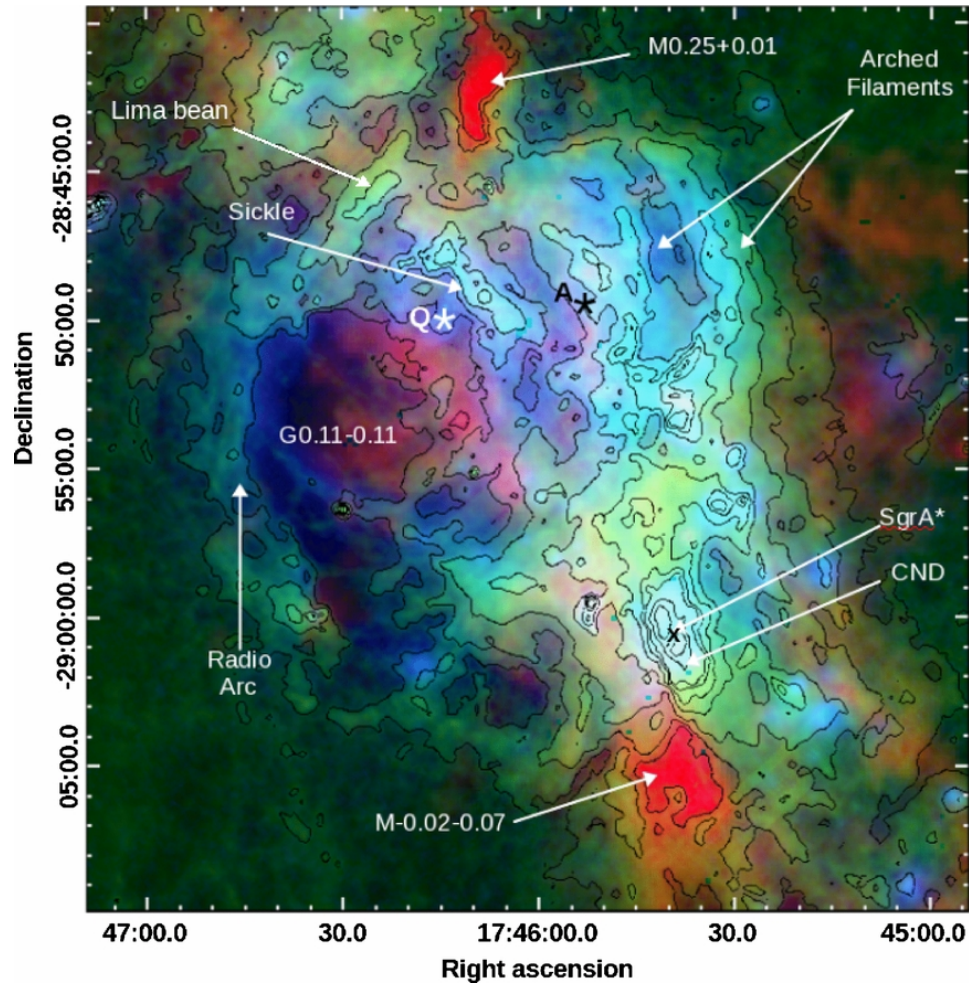


Fig. 1.10: Galactic center in far-infrared domain in different wavelength: $21.3 \mu\text{m}$ (blue), $70 \mu\text{m}$ (green) and $350 \mu\text{m}$ (red). Around the central cavity stretching from 1 to 5 the circumnuclear disk (CND) is visible. [Image credit to Etxaluze et al. (2011)]

Far-infrared wavelengths are very hard to observe since earth's atmosphere is not transparent for these wavelength. Observations are only possible for either very high located or airborne observatories. At the wavelength from $30 \mu\text{m}$ to $450 \mu\text{m}$ cold clouds of gas and dust of about 140 Kelvin or less can be observed. At these wavelength for example protostars can be detected before they become visible in

other spectrums. The Galactic Center for instance appears very brightly in the far-infrared domain, like shown in figure 1.10

1.4.4 Near- and mid-infrared wavelength

At near- and mid-infrared wavelength from $1 \mu\text{m}$ to $5 \mu\text{m}$ angular resolution of under arcsecs are possible. The reason therefore is that extinction is ten times lower than in the optical domain. In this wavelength domain every object that emits heat can be observed. Due to the observability of this detailed informations, the mass distribution and motions of stars can be concluded. For instance, Sabha (2015) investigated the stars in the direct vicinity of Sgr A*, the super massive black hole. This star formation is called the S-star cluster.

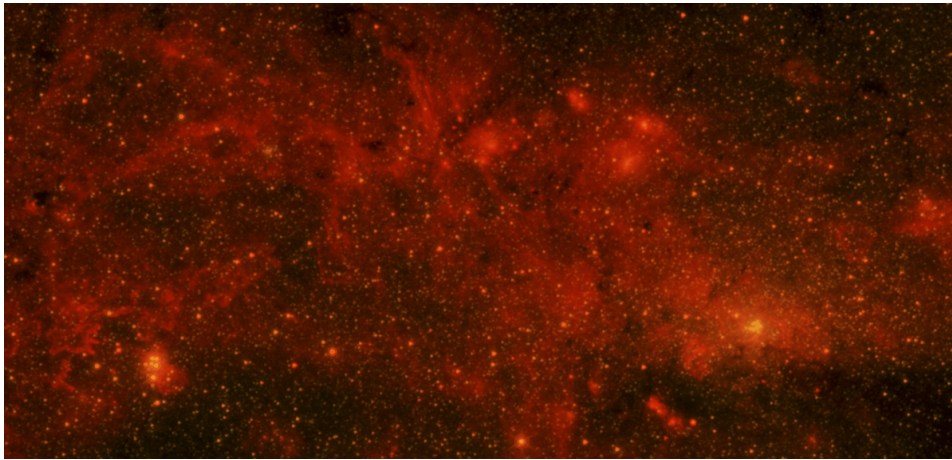


Fig. 1.11: Galactic center in infrared domain [Image credit to NASA (2018b), "NASA/CXC/SAO"]

1.4.5 Optical wavelength

The intensity at the optical domain between $\sim 0.3 \mu\text{m}$ and $\sim 1 \mu\text{m}$ is reduced by approximately 27 magnitudes by the atmosphere (Eckart et al. 2005, p.16). At these wavelengths, studies of polarisation and spectroscopy can be done. Besides the near infrared, the optical domain is the most important source for astronomical insight. The reasons therefore are that most of the activities in galaxies are produced by stars in the visible spectrum and the detectors in this domain work most efficiently. So we investigate the part of the spectrum which is most active with

the most efficient tools [Schneider (2007)]. The development of optical CCD chips increased dramatically in the past years and allows in combination with adaptive optics investigations in the optical domain in high quality. Not to be underestimated should be the influence of the Hubble Space Telescope on the development in the visible spectrum. The Hubble Space Telescope provides insight in, but not only in, the optical wavelength domain that broadened our knowledge of the universe.

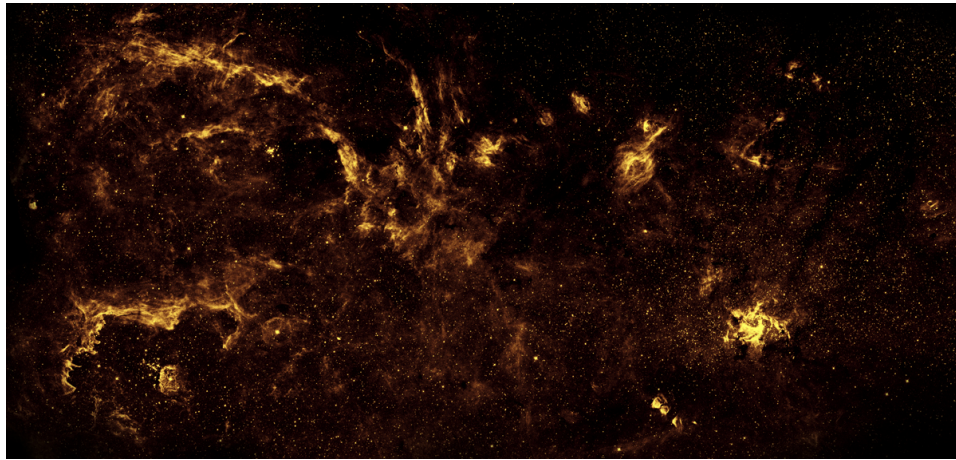


Fig. 1.12: Galactic center in optical domain [Image credit to NASA (2018b), "NASA/CXC/SAO"]

1.4.6 X-ray wavelength

The X-ray wavelength lies between 0.01 nm and 10 nm. Since X-radiation is absorbed by Earth's atmosphere, X-ray observatories are placed at high altitudes for example balloons or in space. X-rays are emitted by astronomical objects that contain very hot gas, approximately 10^7 to 10^8 K (Genzel et al. 2010, p.41). In the case of the Galactic Center the X-radiation is produced by gas that falls into the black hole Sagittarius A*. Caused by the angular momentum of the particles, they cannot cross the event horizon directly but spin around the black hole and lose gravitational energy. Other X-ray sources are for instance supernova remnants and binary stars containing a white dwarf. X-rays hitting a surface perpendicularly are absorbed rather than reflected. In order to be reflected, X-rays must hit a very high quality surface nearly parallel. The surface has the form of a slowly narrowing cone. The field of view of X-ray telescopes is about 1 degree and the resolution of

the order of a few arcseconds. The detector is usually a *Geiger-Müller counter*. In newer image instruments also CCD cameras are used.



Fig. 1.13: Galactic Center in X-ray domain [Image credit to NASA (2018b), "NASA/CXC/SAO"]

1.4.7 γ wavelength

The γ -radiation is the highest accessible energy to determine the Galactic Center. The energy of γ quantum lies above ~ 500 keV. It must be detected by orbiting observatories since all γ -radiation is also absorbed by Earth's atmosphere. γ -rays are produced by transitions in atomic nuclei or in mutual interactions of elementary particles. These high energies cannot be focused by mirrors or lenses, because γ -radiation just passes through them. Instead coded mask imaging is used, which have certain patterns made of opaque material. By blocking and unblocking the γ -rays, later on the origin structure can be computed. This is a similar approach which is used by particle detectors.

Although γ -radiation cannot penetrate Earth's atmosphere, effects they cause can be observed. When high energy γ photons enter the atmosphere, particle-antiparticle pairs can be created. The kinetic energy of these particles can be so high, that they move faster than local speed of light in the atmosphere. If this happens, Čerenkov radiation is produced in visible light domain and can be observed.

1.4.8 Sagittarius A*

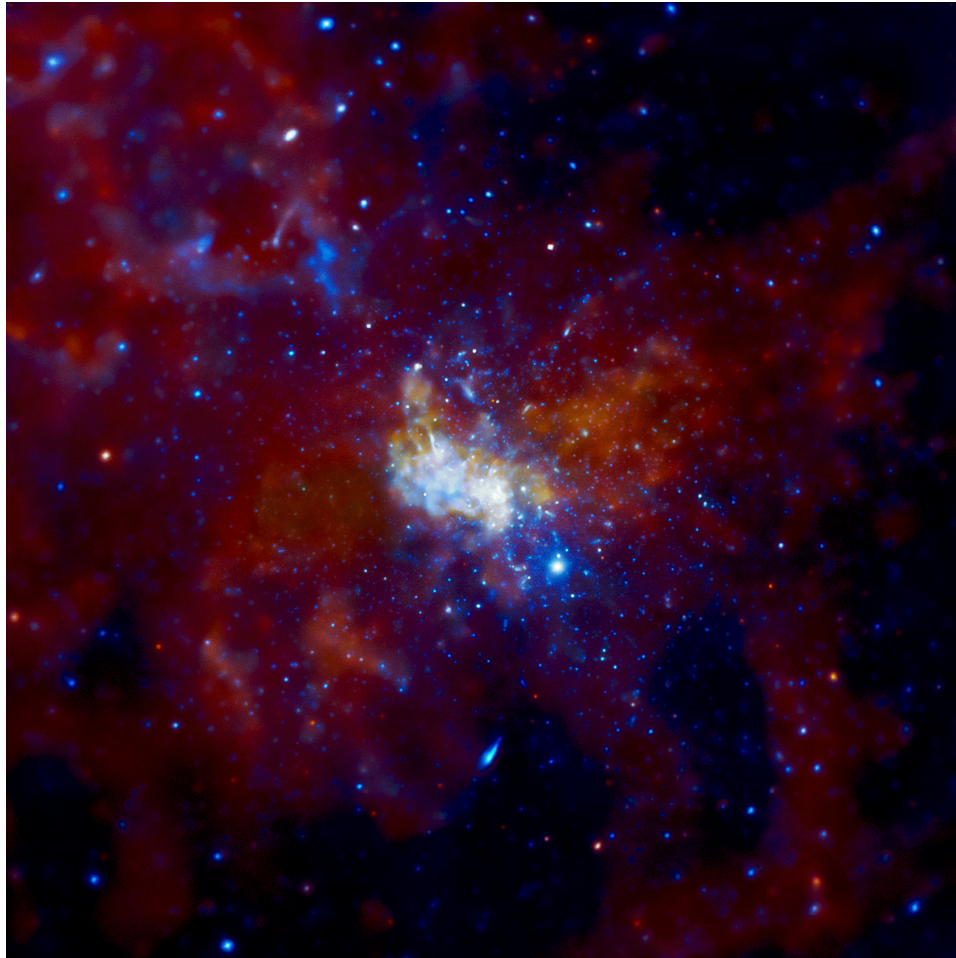


Fig. 1.14: Sagittarius A* in X-ray domain. The image is 15 arcmin across. [Image credit to NASA (2018b), "NASA/CXC/SAO"]

Already in the 1930s a strong radio source in the constellation Sagittarius at the Galactic Center was observed. In 1974 Balick & Brown (1974) found that the radio source is a super massive black hole (SMBH) called Sagittarius A* or short Sgr A*. Sgr A* appears as a compact radio source of a size of less than 2.4×10^{13} cm at a distance of 8 kpc (26,000 lightyears). The spectrum of Sgr A* is best known in radio- and sub-millimeter wavelength and barely in infrared or X-ray

wavelengths. There is a specific peak of radiation at sub-millimeter domain, which most likely is emitted by plasma within a few Schwarzschild radii of the event horizon of the black hole. In the infrared and X-ray domain, Sgr A* shows bursts of emissions, which likely are related to the increase of luminosity within minutes by a few magnitudes in infrared domain. This short temporal correlation suggests an emission within 10 Schwarzschild radii of the black hole. Due to the fact that these bursts are localised in the direct vicinity of the event horizon and also take place on very short time scales, it is suspected that these events contain information about the spin and mass of the black hole. In the near future, hopefully, it will be possible to increase the resolution of Sgr A* in the sub-millimeter domain by very long baseline interferometry. The goal of this intention would be to confirm that Sgr A* is truly a black hole by imaging the edge through gravitational deflection.

1.5 Parallaxic Angle

The parallaxic angle q is a function of the hour angle and is defined as the angle in the astronomic triangle opposite the colatitude and between the altitude and the 90° - declination. The other two angles are the azimuth and the hour angle (Fig. 1.15). The astronomic triangle is spherical and it applies to the sinus rule

$$\frac{\sin(90^\circ - B)}{\sin(q)} = \frac{\sin(z)}{\sin(t)} \quad (1.46)$$

which is equal to

$$\begin{aligned} \sin(z) \cdot \sin(q) &= \sin(90^\circ - B) \cdot \sin(t) \\ &= \cos(B) \cdot \sin(t). \end{aligned} \quad (1.47)$$

Although the equation 1.47 could be solved for q , the value of q is not precisely defined by $\sin(q)$. The reason therefore is that q could be originated in each quadrant and it is possible that two different angles have the same sine value. An angle can be determined exactly by knowing both its cosine and sine value.

The sinus-cosinus-rule provides

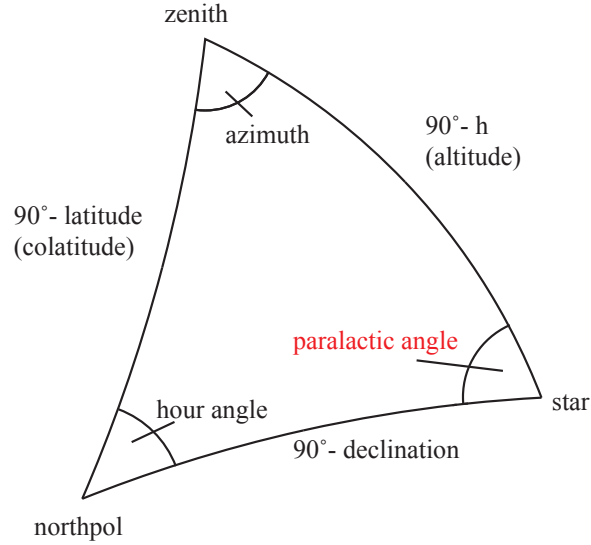


Fig. 1.15: Parallaxic angle

The parallaxic angle q is a function of the hour angle and is defined as the angle in the astronomical triangle opposite to the colatitude and between the altitude and $(90^\circ - \text{declination})$. The other two angles are the azimuth and the hour angle.

$$\begin{aligned} \sin(z) \cdot \cos(q) &= \cos(90^\circ - B) \cdot \sin(90^\circ - \delta) - \sin(90^\circ - B) \cdot \cos(90^\circ - \delta) \cdot \cos(t) \\ &= \sin(B) \cdot \cos(\delta) - \cos(B) \sin(\delta) \cos(t). \end{aligned} \quad (1.48)$$

Dividing both equations leads to

$$\tan(q) = \frac{\sin(z) \cdot \sin(q)}{\sin(z) \cdot \cos(q)} = \frac{\cos(B) \cdot \sin(t)}{\sin(B) \cdot \cos(\delta) - \cos(B) \cdot \sin \delta \cdot \cos(t)}. \quad (1.49)$$

The equation 1.49 can be divided by $\cos(B)$, because the latitude B lies between -90° and $+90^\circ$, so $\cos(B)$ is always positive. Therefore the parallaxic angle is given as

$$q = \arctan\left(\frac{\sin(t)}{\tan(B) \cdot \cos(\delta) - \sin \delta \cdot \cos(t)}\right). \quad (1.50)$$

The Large Binocular Telescope Observatory (LBTO) is located on Mt. Gra-

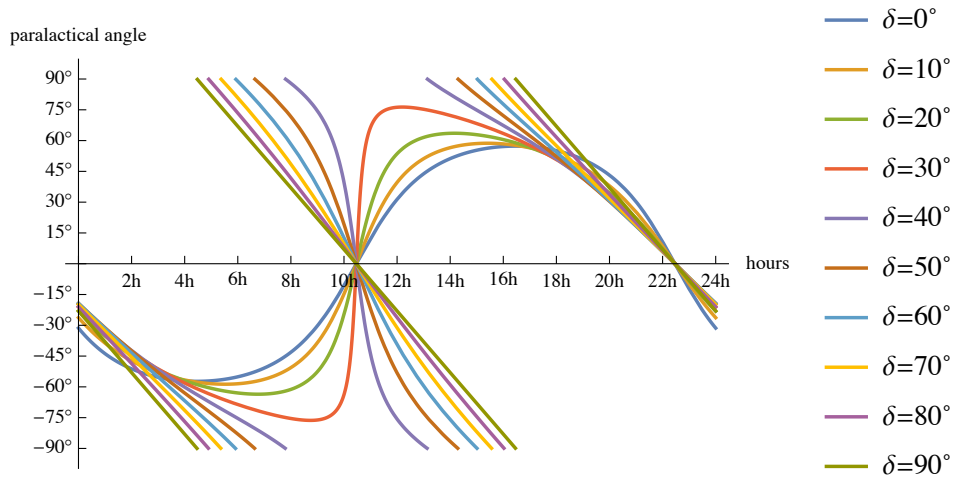


Fig. 1.16: Parallaxial angle for various declinations

ham in Arizona². For the latitude α of the LBTO of $32^{\circ}42'04.71''$ and various declination angles, the progress of the parallaxial angle is shown in Fig. 1.16. For observing the Galactic Center with its declination of $-29^{\circ}00'28.1''$ the parallaxial angle varies over the hour angle like shown in figure 1.17.

The hour angle τ is equal to the difference of the sidereal time θ and the right ascension α .

$$\tau = \theta - \alpha \quad (1.51)$$

The sidereal time can be calculated by (Meeus (1991))

$$\theta = \theta_0 \pm \lambda \begin{cases} + & \text{for eastern } \lambda \\ - & \text{for western } \lambda \end{cases} \quad (1.52)$$

where eastern longitudes are positive and western longitudes are negative. For θ_0 applies equation 1.53

²W109°53'20.63" N32°42'04.71", altitude = 3221 m, MST=UT-7. See Chapter 1.8.

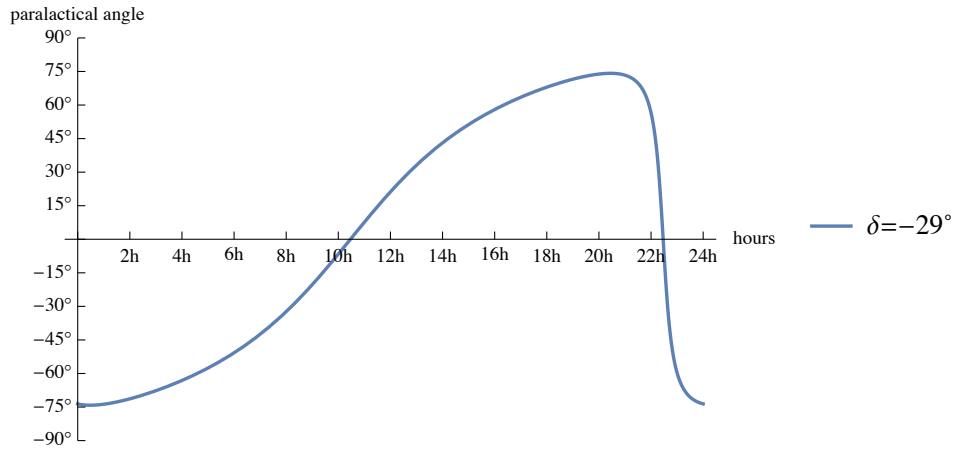


Fig. 1.17: Parallax angle for the GC

$$\begin{aligned} \theta_0 = & 280.46061837 + 360.98564736629 \cdot (\text{JD} - 2451545.0) \\ & + 0.000387933T^2 - \frac{T^3}{38710000.0}. \end{aligned} \quad (1.53)$$

The outcome of equation 1.53 is in degree. T can be calculated via equation 1.54. A sample code for calculating Julian date (JD) is shown in listing 1.1.

$$T = \frac{\text{JD} - 2451545.0}{36525} \quad (1.54)$$

Listing 1.1: Sample code for calculating Julian date following Meeus (1991).

```
double JulianDay(int date, int month, int year, double UT)
{
    if (month<=2) {month=month+12; year=year-1;}
    return (int)(365.25*year) + (int)(30.6001*(month+1)) -
        15 + 1720996.5 + date + UT/24.0;
}
```

The Julian date on 1st January 2015 at 03:00 h is $\text{JD} = 2457023.625$ and for this time the parallax angle equals

$$q = -10.4884^\circ.$$

1.6 Altitude

The altitude of astronomical objects observed from Earth varies with the hour angle τ , the declination δ of the observed object and latitude B of the observers position on Earth:

$$a(\tau, \delta) = \arcsin(\cos(\tau) \cdot \cos(B) \cdot \cos(\delta) + \sin(B) \cdot \sin(\delta)). \quad (1.55)$$

This is illustrated in figure 1.18 for the northern hemisphere. One can see that the amplitude of the altitude is bigger for smaller declinations, that means for an object at the equator level the difference between the highest and lowest position is maximal and for an object at north pole level the celestial object appears always on the same altitude. The highest altitude is reached at a declination of about 30° . Figure 1.18 shows different declinations for the latitude of LBTO, the latitude of LBTO. For the declination of the Galactic Center ($\delta = -29^\circ$) the variation of the altitude over the hour angle and the latitude of LBTO ($B=32.70^\circ$) is shown in figure 1.19.

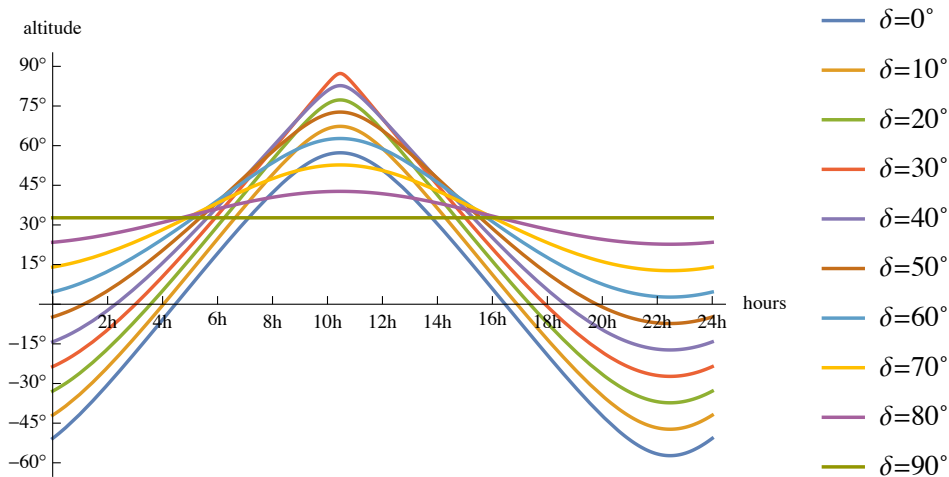


Fig. 1.18: Altitude variation over the hour angle for various declinations and the latitude of LBTO ($B=32.70^\circ$). The amplitude of the altitude is bigger for smaller declinations, that means for an object at the equator level the difference between the highest and lowest position is maximal and for an object at north pole level the celestial object appears always on the same altitude. The highest altitude is reached at a declination of about 30° .

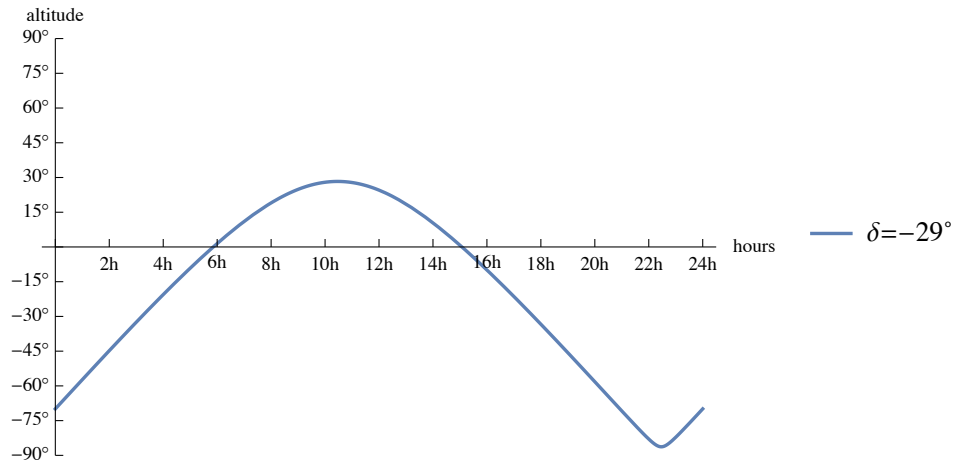


Fig. 1.19: Altitude variation over the hour angle for declination $\delta = -29^\circ$ (GC) and latitude $B=32.70^\circ$ (LBTO). The maximum altitude is at 28.298° where the parallactic angle is 0.

1.7 Field rotation

During the motion at the night sky, each celestial object gains a periodic rotation. Such a field rotation is shown in figure 1.20. The rotation of the celestial object reaches its origin orientation after one solar day and the amplitude of rotation depends on its declination. The angle of field rotation corresponds with the parallactic angle. The alt-azimuth mounting of the LBTO causes the image to rotate in the focal plane. That means the observed image rotates corresponding to equation 1.50 and the image in the focal plane rotates like shown in figure 1.20 respectively. It is to mention that, although one complete rotation is realised within a solar day, the rotation velocity is not constant but depends on the time derivation of the parallactic angle. The derivation of the parallactic angle \dot{q} is shown in figure 1.21. The field rotation is essential for the image quality for exposures longer than 1 sec. Basically two possible approaches can be used:

► Short time exposures:

Smearing caused by field rotation appears by exposures longer than 1 sec. At exposure times shorter than 1 sec the effect of field rotation on the image quality is negligible. For longer exposures field rotation must be compensated.

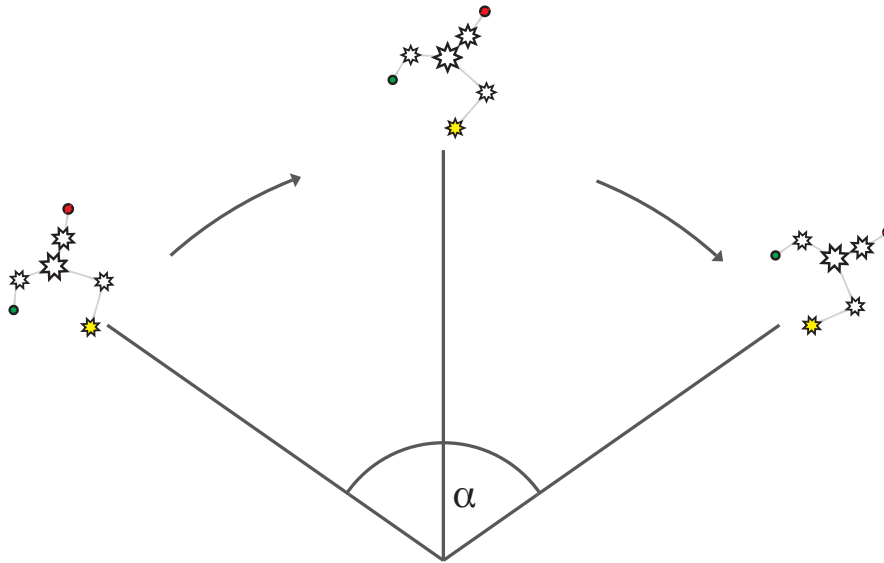


Fig. 1.20: Schematic illustration of field rotation:

The alt-azimuth mounting of the LBTO causes the image to rotate in the focal plane. That means the observed image rotates corresponding to equation 1.50 and the image in the focal plane rotates like shown in this figure respectively.

► Rotating of focal plane:

In order to compensate field rotation the detector can be rotated according to the parallactic angle. This method is used at the LBTO (Bertram 2007, P. 31).

The variation \dot{q} of the field rotation is the first derivation of the parallactic angle q in equation 1.50 and describes how fast the parallactic angle changes and, hereby, how fast the detector must rotate:

$$\dot{q} = \frac{dq}{d\tau} = \frac{\tan(B) \cos(\delta) \cos(\tau) - \sin(\delta)}{(\sin(\delta) \cos(\tau) - \tan(B) \cos(\delta))^2 + \sin^2(\tau)}. \quad (1.56)$$

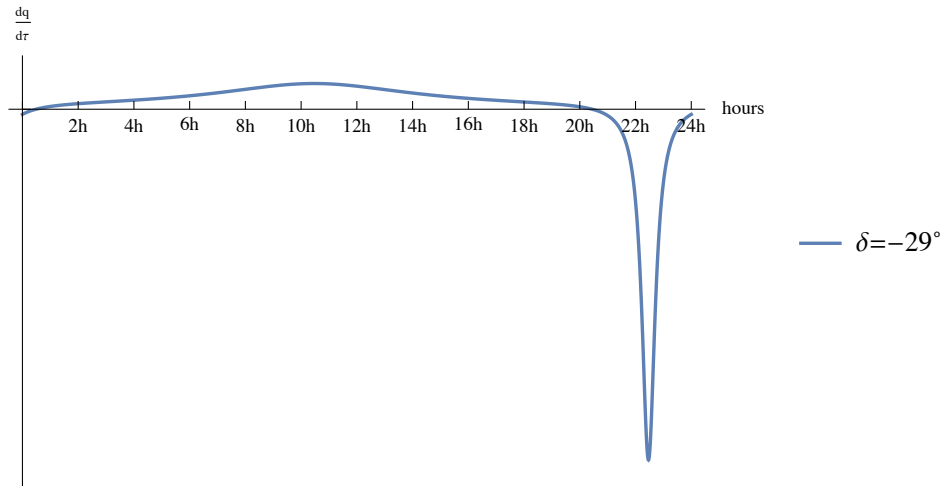


Fig. 1.21: Field rotation:

The variation \dot{q} of the field rotation is the first derivation of the parallactic angle q in equation ? and describes how fast the parallactic angle changes and, hereby, how fast the detector must rotate. The first derivation is shown here as graphic for the declination $\delta = -29^\circ$ and the latitude $B = 32.70^\circ$

1.8 The Large Binocular Telescope

The Large Binocular Telescope (LBT) has two 8.4 m monolithic mirrors which are mounted in alt-azimuth setup. It is located on Mount Graham in southeastern Arizona at an altitude of 3300 m and saw first light in October 2005 with the first primary mirror. The second primary mirror saw first light in September 2006. Both mirrors together were brought into service in January 2008. The mirror of the LBT has 8.4 m diameters and the mirrors are placed 14.4 meters apart measured from the center of each mirror. The LBT has the same light gathering capacity as a single telescope of 11.8 meter diameter and the optical resolution as a single telescope of 22.8 meter diameter, though the angular resolution is higher perpendicular to the orientation of the fringes. This limitation is compensated due to the rotation of the observed object by the parallactic angle (see section 1.7). So by observing the object over a longer period of time, the angular resolution of the object can be increased for each axe.



Fig. 1.22: Large Binocular Telescope (LBT), on Mount Graham in southeastern Arizona at an altitude of 3300 m (LBT (2018)), [Image credit: Large Binocular Telescope Observatory]

There are four different modes in which the LBT can operate:

1. **Individual beam mode**

Both telescopes operate independently. It is possible to observe two areas with a distance up to a few arc-minutes.

2. **Incoherent beam combination mode**

In this mode both telescopes point to the same area and the light-gathering capacity is combined.

3. **Coherent beam mode**

The coherent beam combination provides additionally the phase information and so an enhancement of the spatial resolution.

4. Homothetic imaging

In this mode, the coherent beam combination is paired with the homothetic pupil condition. So a higher spatial resolution can be achieved. A detailed description can be found in section 1.1.2.

The LBT has reached strehl ratios of about 60-90% in the infrared h band and 95% in the infrared m band. For comparison, older adaptive optics only reached a Strehl ratio of about 20-30% whereas a not corrected Strehl ratio lies at about 1%

1.9 LINC-NIRVANA

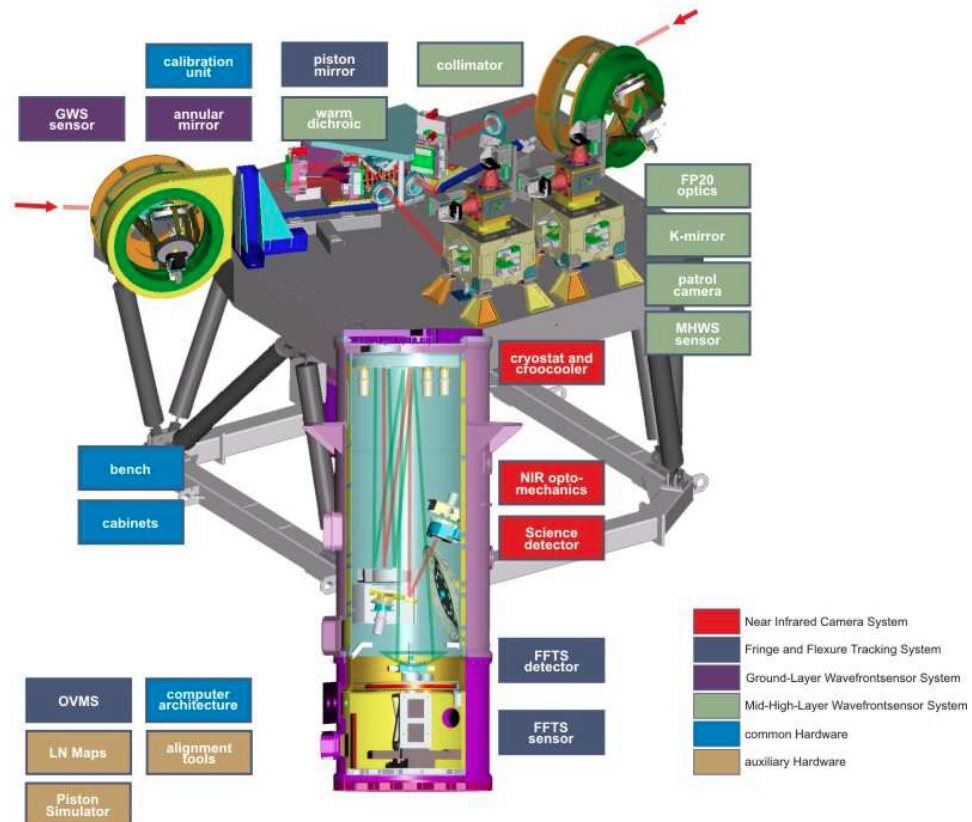


Fig. 1.23: System and sub-system overview of LINC-NIRVANA (Kürster (2010))

LINC-NIRVANA (LBT **I**Nterferometric Camera - Near-**IR**/Visible Adaptive **i**Nterferometer for **A**stronomy) is the homothetic image camera of LBT. It provides the capability to cophase images and adaptive optics. The advantage of its setup is that it is possible to reconstruct images with only a few observations during a night.

LINC and NIRVANA are two different modes. The **LINC-mode** provides NIR with classical adaptive optics, that means the adaptive optics correction operates with an on-axis natural guiding star. This implies that the observation performance of scientific targets will decrease when the distance between target and guiding star increases. The on-axis observation is also used for the fringe and flexure tracking system. The **NIRVANA-mode** provides a two-layer multi-conjugated adaptive optic. The performance in the NIRVANA-mode depends on the asterism of the guiding stars (number, magnitudes and spacial distribution). The two sensor layers are the two mid-high-layer wavefront sensor (MHWS) and the two ground-layer wavefront sensors (GWS).

1.10 Multi Conjugate Adaptive Optics (MCAO)

The layer-oriented MCAO of LINC-NIRVANA is a system to correct occurring disturbances in the atmosphere. Up to three deformable mirrors in each aperture are assigned to specific atmospherical layers. Each mirror corrects the wavefront it is assigned to. Each unit contains a pyramid wavefront sensor (Ragazzoni (1996)), which allows to collect the light of all the references and the bundle on a single CCD. The number of reference stars is limited by the number of pyramid wavefront sensors, maximum 8 reference stars for the MHWS and 12 reference stars for GWS. Due to this setup, the AO system does not depend on the magnitude of a single reference star but rather on the combined magnitudes of all used reference stars.

1.11 Functional principle

The light of both telescopes of the LBT will be combined by LINC-NIRVANA into an interferometer. Atmospherical disturbances will be corrected by MCAO

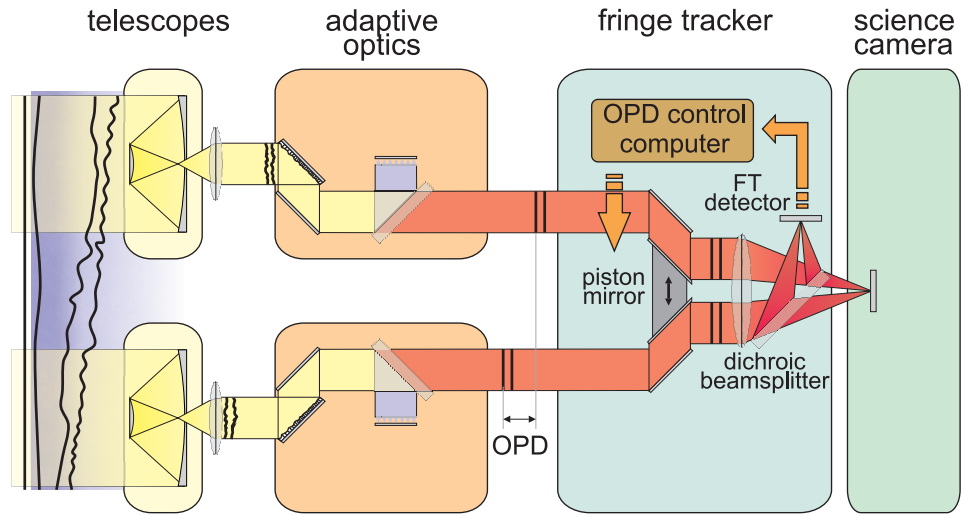


Fig. 1.24: Functional principle of LINC-NIRVANA (Bertram (2007))

(see section 1.10). Light from both telescopes enter through the annular mirrors and the field of view between 2 and 6 arcminutes will be directed to the ground layer wavefront sensor (GWS). The central 2 arcminutes are directed to the piston mirror.

The purpose of the piston mirror is to compensate the optical path-length difference (OPD). It is controlled by the OPD control computer which calculates the movement of the piston mirror with information provided by the fringe tracker detector (see Fig 1.24). The fringe tracking servo loop analyses the differential piston by measuring the fringe pattern of the reference star. The crucial condition for detecting fringes is that the differential piston is smaller than the coherence length

$$I_c = \frac{\bar{\lambda}^2}{\Delta\lambda} \quad (1.57)$$

where $\bar{\lambda}$ is the mean wavelength and $\Delta\lambda$ the width of the observed band. There are two reasons for differential pistons with different power-spectra:

1. Atmospheric differential piston

Wavefronts which pass through the atmosphere and experience disturbances. The surface of the wavefront is corrugated but still continuous. Moreover

the emerging wavefront is mostly not parallel and does therefore not hit each aperture at the same time. Differential pistons are caused by low-order atmospheric phase perturbations which exceed the size of each aperture.

2. **Instrumental effects**

The reasons for instrumental effects can for example be static misalignments, vibrations and non-perfect AO corrections.

Software description

Simulation software can be used to investigate and determinate properties and feasibilities of certain physical systems before these are implemented. Additionally, simulation results can help verifying experimental accuracy and locating experimental flaws. Simulations also can provide a better understanding of the given problem by making simplifying assumptions (Tordi et al. (2002)). LOST (Layer Orientated Simulation Tool) was created in order to test the feasibility of layer orientated multi-conjugate adaptive optics. Following, the structure of the software and certain parts of the simulation will be presented.

2.1 Simulation structure

LOST is written in Interactive Data Language (IDL) and runs on Unix and Windows operating systems. A simulation takes a few hours to weeks depending on certain parameters, which are defined in a script file, and the computing power. Those parameters are among others the field of view, the atmosphere and the demanded precision. In the script file also the telescope parameters like diameter and AO system like the wavelengths, the number of DMs (Deformable Mirrors) and the reconstruction method are defined. Two types of wave front sensors (WFS) are implemented in LOST: Shack-Hermann (SH) and pyramid.

There are three main steps during a simulation run: the input definition, the main loop and the output computation (fig. 2.1). Each natural guiding star (NGS) is allocated to a certain layer and so to a DM. The turbulent layer and the atmospheric turbulences are represented as phase screen shifting during each simulation step. The performance of the optical system, precisely the AO system, is represented as Strehl ratio (SR), which is computed as output file at the end of the simulation. The

SR is generated with the aid of point spread functions (PSF) which is calculated in each step and integrated at the end of the simulation loop in order to generate the long exposure SR map (Arcidiacono (2005)).

2.2 Simulation setup

2.2.1 Telescope and MCAO

The user can define the telescope parameters and MCAO system via script, for example the aperture of the telescope in meters and the pupil dimension in pixel. The dimension of pixel used to define the pupil is correlated to calculation precision of the Zernike polynomials (see section 1.2.5). Tordi et al. (2002) gives an example: a pupil with 128 pixels in combination with a 8 m telescope leads to pupil sampling of $\Delta s = 25$ cm/pixel. For the upper limit of the sampled spatial frequency this leads to a value of $k_{up} \approx 8$ m^{-1} . The sampling quality depends on the coherence radius r_0 of the turbulent layer (see section 1.2.1). For $r_0 \approx 25$ cm the sampling quality can be considered as good, since the variance of the part of the spectrum that is not corrected is smaller than 1 rad^2 (Tordi et al. 2002, p. 224, section 2.1). The number of DM and the corresponding altitudes to which the DM are allocated are also set in the script files. In addition, the wave front sensors are defined: Shack-Hermann or pyramid sensors. In the following simulations Shack-Hermann wave front sensors are used.

2.2.2 Atmosphere

In the config file the number of atmospheric layers are defined. In the considered simulation the number of atmosphere layers is seven. In LOST, the phase screen of each atmosphere is computed via Fourier transformation. In order to match the Kolmogorov power spectrum, sub-harmonic frequencies are added. Each face screen then is normalised. The phase screen is generated by the power spectrum defined by the Wiener relation:

$$PS(r_0, k) = 0.023r_0^{-5/3}(k^2 + k_0^2)^{-11/3} \quad (2.1)$$

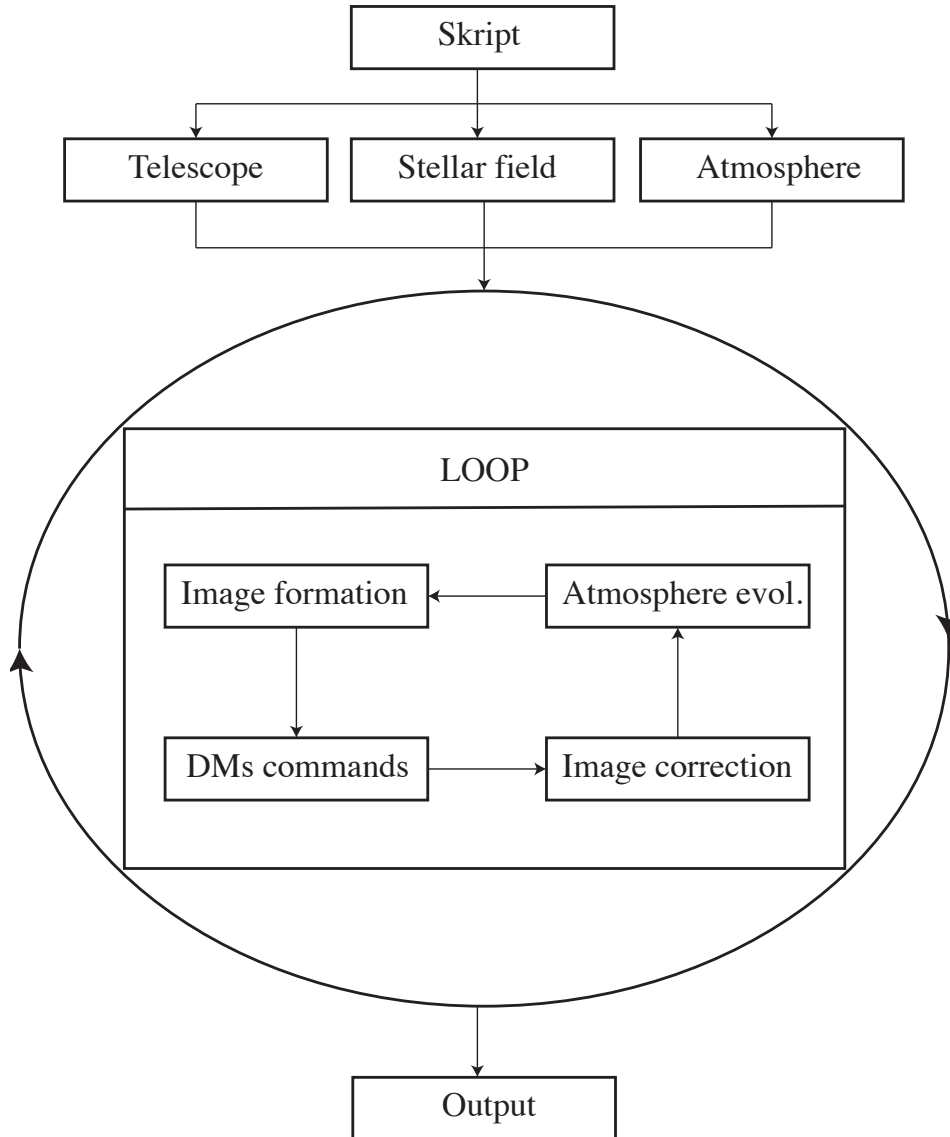


Fig. 2.1: Software structure: At first in a script file the relevant parameters are set (telescope parameters, stellar field and atmospheric configuration). In the next steps the simulation loops are performed. The number of loops depends on the simulation time. During the loops in each steps image formation is performed. This input is used to perform the DMs commands, which are used to correct the images. The next step is to evolve the atmosphere and again format the image. After the corresponding number of loops are done, the output algorithms provide the output files, i.a. the long exposure PSF files. [Tordi et al. (2002)]

where r_0 is the Fried parameter, k is the spatial frequency and k_0 is the frequency corresponding to outer scale L_0 . Normalising is done by dividing the phase screens by the square root of the average variance. This value is computed by averaging the phase standard deviation relative to a square grid telescope pupil over the phase screens. Then, the screens are multiplied by a factor that is the theoretically predicted phase variance over the pupil (Arcidiacono (2005)):

$$\sigma_\phi^2 \approx 1.03 \left(\frac{D}{r_0} \right)^{5/3}. \quad (2.2)$$

The atmospheric layer's size is defined by the pixel size given by the ratio between the dimension of the pupil diameter, which is given in the configuration file, and the Fried parameter

2.2.3 Computing wind

The direction and wind speed is randomly calculated. The distributions for five independent simulations are shown in fig. 2.2. The wind speed and direction along with the atmospheric setup can be stored and reused for other simulations. One can see that the speed direction distribution variates in a range from +40 m/s to -40m/s. On the left graph, the wind speed in x-direction and on the right graph the wind speed in y-direction are shown on the y-axis. The x-axis represent different simulations, that means random distributions for each new calculated atmosphere. The different colours represent the different layers in the atmospheric model. The boxes beneath show the average speed per layer and the corresponding error. The wind speed in both directions is distributed randomly.

2.2.4 Reference star field

One of the wide range advantages of the layer oriented approach is the use of multiple natural guiding stars as reference sources. The guiding stars are defined by the galactic latitude b , the galactic longitude l and the magnitude V . The atmospheric correction are weighted by the brightness of the guiding stars. For a single guiding star, the atmospheric corrections take place around the guiding star and, accordingly, the Strehl ratio and the point spread function are of better quality around the

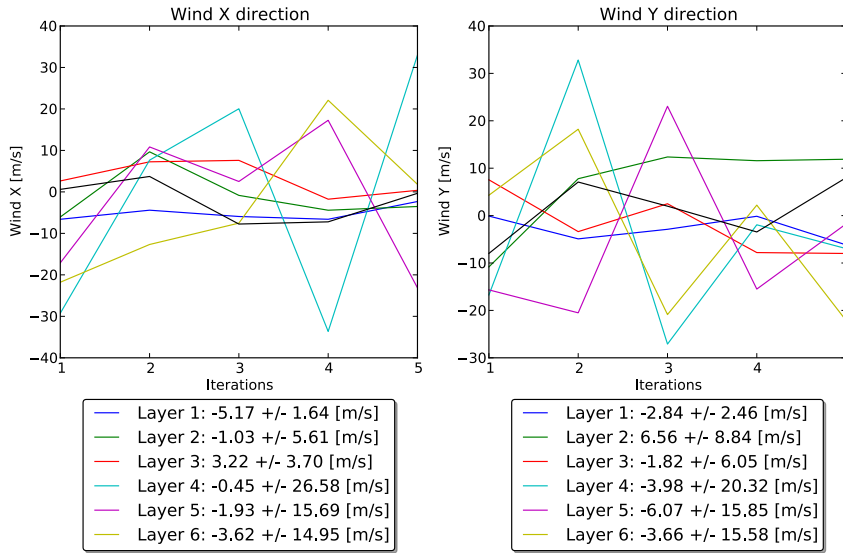


Fig. 2.2: Distribution of wind direction and speed:

On the left graph the wind speed in x direction and on the right graph the wind speed in y direction are shown on the y axis. The x-axis represent different simulations, that means random distributions for each new calculated atmosphere. The different colours represent the different layers in the atmospheric model. The boxes beneath show the average speed per layer and the corresponding error. The wind speed in both directions is distributed randomly.

NGS and decline in the part which are further away from the NGS. In the main simulation (section 3.9) two guiding stars are used: IRR1¹ and IRR2² with the magnitudes of 13.7 mag and 13.2 mag, respectively. In the case of multiple NGSs, the brightness distribution is more important. If one NGS is much brighter than the other the correction would drive towards this point and the residual field would be disproportionately worse. This would lead to unbalanced Strehl ratio and PSF. For the best result regarding a balanced Strehl ratio and best possible corrected field, the magnitudes of the NGS should not vary very much. By using similar magnitudes the advantage of multiple NGS can be utilised.

¹Position: 17h 45min 40.07sec, -29° 00' 27.5"

²Position: 17h 45min 40.21sec, -29° 00' 25.2"

2.2.5 Dummy stars

The main goal of MCOA system is to obtain a wide field of view. Thereby is beside uniformity the amount of correction likewise important. LOST measures the phase of each layer and weights it by the illumination of the stars. Each WFS processes the superposition of phases given by different layers. The correction is performed by using a certain number of Zernike polynomials and is then applied to the shape of the DM. These corrections are then applied to the integral phase over the line of sight of each star and dummy star. By doing so, it is possible to compute the Strehl ratio not only at the location of the NGS but also over the complete field of view and so we can obtain a continuous Strehl ratio and hereby a continuous PSF.

2.3 PSF and strehmap

After each iteration the instantaneous PSF is calculated with the wave-front residuals in each direction the user has defined in the config file. Additionally, after each step, the SR is computed as the ratio between the centre of the PSFs and of the diffraction limited PSF. To get the long exposure PSF, which is determined at the end of the simulation run, the PSF of each loop is summarised. Also, the instantaneous SR data are saved. The long exposure SR map over the FoV is calculated by linear interpolation of the SR values over each sky direction.

2.4 Deconvolution

In order to get the initial picture, the, with the PSF convolved pictures, need to be de-convolved. Therefore, the lucy-algorithm is applied (Eckart et al. (2005)). In the lucy-algorithm an initial picture is estimated. The better this estimation is the more efficiently works the algorithm. This estimated image $O_k(x, y)$ is convolved with the know PSF $H(x, y)$ and one obtains the image $\Psi_k(x, y)$:

$$\Psi_k(x, y) = O_k(x, y) \odot H(x, y) \quad (2.3)$$

In the next step the observed image $G(x, y)$ is divided by the obtained picture $\Psi_k(x, y)$ and convolved with the PSF $H(x, y)$. Doing this one gets a correction

2×2 -matrix $R_k(x, y)$:

$$R_k(x, y) = \frac{G(x, y)}{\Psi_k(x, y)} \odot H(x, y). \quad (2.4)$$

When the correction factor $R_k(x, y)$ is now multiplied with the estimated image $O_k(x, y)$ one receives the next estimated image $O_{k+1}(x, y)$ for the next iteration:

$$O_{k+1}(x, y) = O_k(x, y) \cdot R_k(x, y) \quad (2.5)$$

The Lucy-algorithm was implemented in IDL. However, due to a much better performance, for the evaluation the software "dpuser" was used here. To perform the deconvolution, 10.000 iterations were performed. Due to the fact, that during the study of the science cases in chapter 4, five different parallactic angles were simulated, the deconvolution algorithm needed to be adjusted. This adjustments are described in section 3.8.

2.5 Simulation parameters

LOST allows to simulate various setups. For the performed simulations in chapter 4 the setup of LBT is used with a telescope aperture of 8.2 m and a pupil size of 128 pixel. The WFS wavelength is set to 2.12 microns and two DMs are implemented in altitudes 0 m and 9000 m. The Kokmogorov atmosphere model contains 7 layers of a size of 4096 pixel x 4096 pixel each. Two natural guiding stars are implemented. The complete simulation parameters are listed in table 2.1.

Tab. 2.1: This table shows the parameters used to perform the simulations in chapter 4

Sections	Parameter Name	Parameter value
Telescope	Telescope aperture	8.2m
	GWS FoV	120'' - 360''
	Layer size	4096 pixel
	Pupil size	128 pixel
	Scientific wavelength	2.12 microns
	WFS wavelength	0.75 microns
	Time scale	10^{-4} s
	System	Number of DMs
Altitudes of DMs		0 m and 9000 m
Loop		Number of steps
	Number of Zernike modes	113 and 201
	PSF size	1364 pixel
	Atmosphere	Number of layer
Size of layer		4096 pixel
Atmospherical model		Kolmogorov
Stellar field	Number of NGS	2
	X-position of NGS	-8.92'', -29.57''
	Y-position of NGS	16.90'', -8.75''
	Magnitudes of NGS	13.70 mag, 13.20 mag
	Dummy stars	Number of dummy stars
Grid step between dummy stars		20''
WFS characteristics		bandwidth integration
	quantum efficiency	0.3
	Sky brightness (R-band)	17

Simulations

In order to analyse the science cases in chapter 4, the PSFs for different parallactic angles must be generated. Although LOST generates one Strehl map, 25 PSF are generated in the present simulation setup, since the field of view is divided in 5×5 squares. The numbering of the PSFs starts with 1 in the upper left corner or 1st element in the 1st line, and ends with 25 in the lower right corner the 5th element in the 5th line. Each single PSF is convolved with the corresponding part of the input picture that shall be analysed and the resulting picture must be recomposed accordingly. Although having multiple PSFs, the goal is to create a single output image.

These procedures and corresponding results are described in this chapter.

3.1 Simulation setup

In this first simulation the natural guiding star is set at the right middle edge, at position (30"0"). In figure 3.2 the Strehl map shape shows a maximum at the right side and slopes in all directions. The parallactic angle for this simulation was 35° and the simulated period was 1 second.

3.2 PSFs

The generated PSFs with the simulation setup described in 3.1 are shown in figure 3.1. 25 PSFs have been simulated in a 5×5 grid. Each PSF has an edge length of 1360 pixel and is cut to 250 pixel in order to view the non-zero part of the PSFs due to the fact that these cut out parts are of no interest for further consideration. These crops were made in order to have a better view on the PSFs and has no scientific

effect. One can see that the structure of the PSFs are as expected: the PSF which are in the area of the NGS are much more narrow and sharper than in the areas far away from the NGS. PSF number one for instance takes up nearly the complete 250×250 pixel of the area and no maxima or minima are recognisable, whereas PSF number 15 span only about 20×20 pixel and shows clearly the diffraction limited PSF structure described in section [1.1.3](#).

PSFs

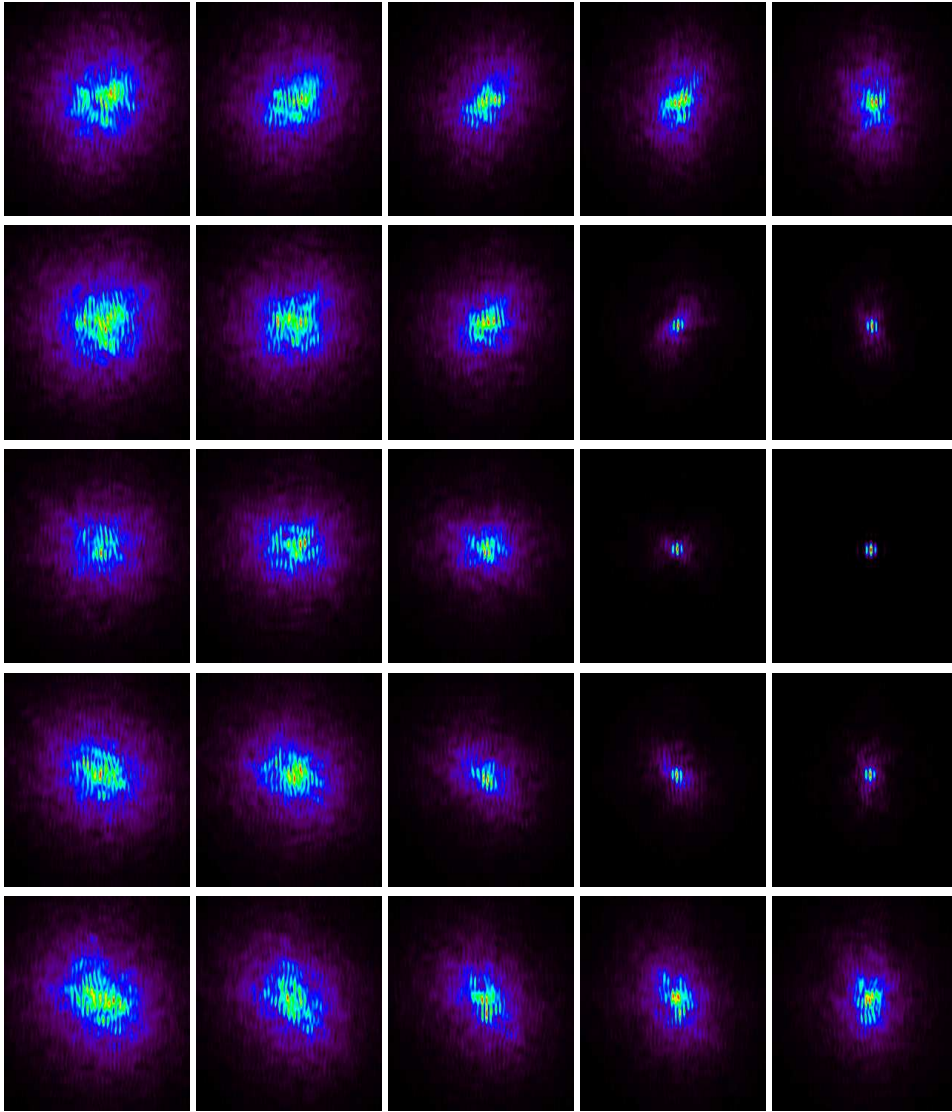


Fig. 3.1: A grid of 5×5 PSFs were simulated. Each PSF has an edge length of 1360 pixel and is cut to 250 pixel in order to view the non-zero part of the PSF's due to the fact that these cut out parts are of no interest for further consideration. These crops were made in order to have a better view on the PSFs and has no scientific effect. One can see that the structure of the PSFs are as expected: the PSF which are in the area of the NGS are much more narrow and sharper than in the areas far away from the NGS. This corresponds with the strelmap shown in figure 3.2

The corresponding Strehl map is composed of this 25 PSFs and is shown in figure 3.2. In both, the PSFs and the Strehl map, it is visible that the guiding star is positioned centre right.

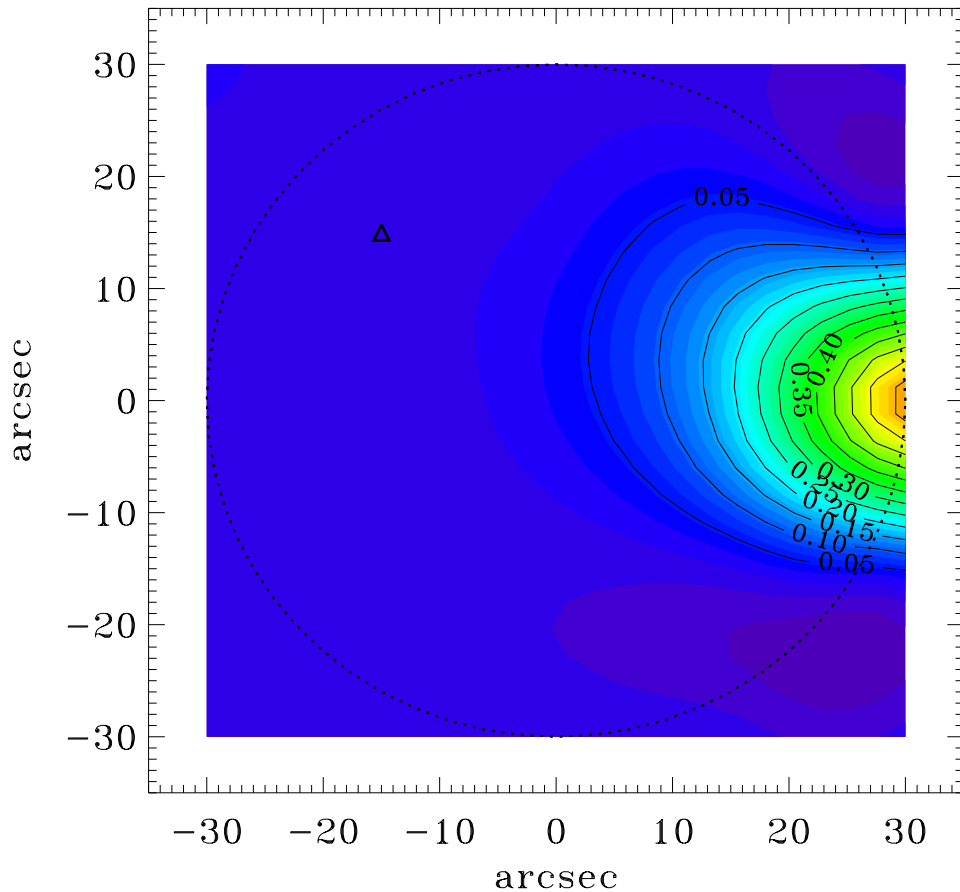


Fig. 3.2: Strehlmap corresponding to PSFs in figure 3.1:

The strehlmap shape shows a maximum at the right side where the NGS was positioned and slopes in all directions. The parallactic angle for this simulation was 35° and the simulated period was 1 second. The other parameters can be seen in table 2.1.

In order to get the final output picture, which considers atmospheric disturbances and instrumental effects, an test input picture was created which later on will be convolved with the PSFs.

Figure 3.3 shows this input picture with 49 punctuated sources with an amplitude of 100 and have an edge length of 250 pixel each to match the edge length

of the corresponding PSFs. This test input picture represents an original image which would appear without atmospheric or instrumental effects. Convolution with the PSF will show which effect atmospheric turbulences and instrumental disturbances have on observations from the Earth's surface.

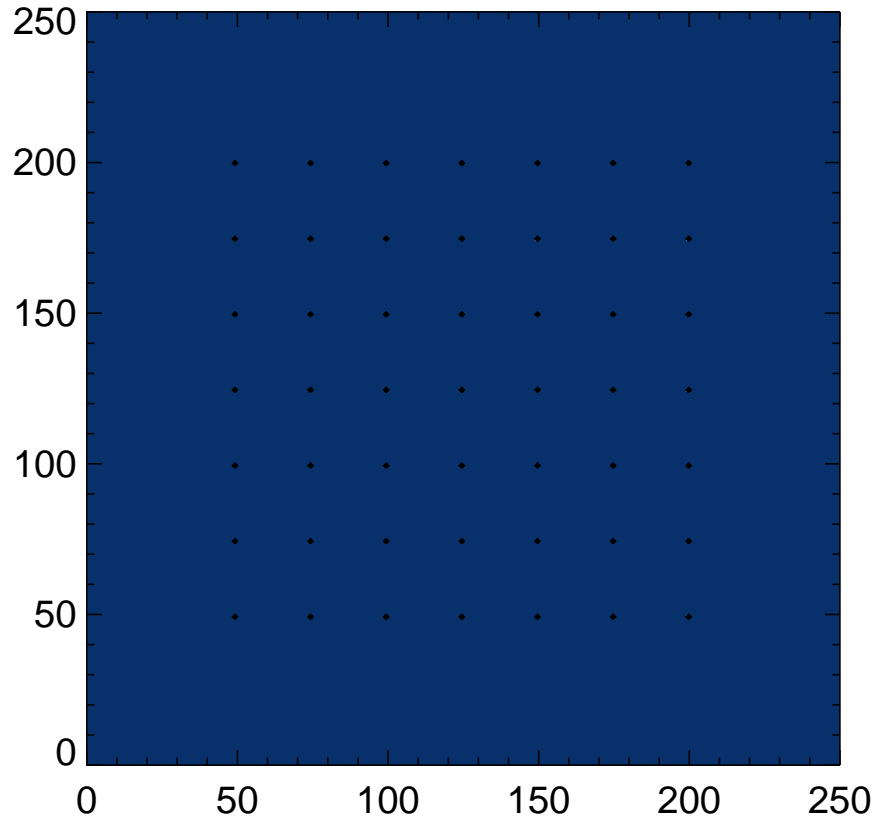


Fig. 3.3: Input pictures:

The test input-picture is specifically chosen: all points have the same magnitude and all points distributed homogeneously so that the effect of the PSF can be estimated for each part of the field of view equally.

The test input picture is specifically chosen: all points have the same magnitude and all points distributed homogeneously so that the effect of the PSF can be estimated for each part of the field of view equally. The test picture is convolved with each of the 25 PSFs shown in figure 3.4. It is important at this point to stress out, that just one input image is convolved with 25 different PSF, that is like observ-

ing the same celestial constellation through 25 different atmospheric and optical systems.

The result is shown in figure 3.4. These 25 convolved output images show the expected structure. The first convolved image (in the top left) shows only a smudged though rectangular structure. There is a noisy structure in the middle sector and the intensity seems to drop in a rectangular form towards the edges. No single sharp maxima is recognisable. This corresponds with low quality in the strehmap and the wide and imprecise PSF in figure 3.1. Along the first row towards the fifth convolved image, the image quality increases. Although more structures can be seen, the single points from the input image are only vaguely recognisable. The quality of the convolved images in the 2nd row are already better. Since the 6th convolved image (1st convolved image in 2nd row) is similar to the 5th, the 10th convolved image ¹ already allows to determine all the maxima from the input image. Also, the diffraction limited structure is recognisable. Especially in the middle, the single maxima get more smudged, but still each maxima is visible. For the 15th convolved pictures the best PSF is used. Best means that the PSF is small, sharp and shows the diffraction limited structures. Accordingly each maxima is recognisable with its diffraction limited form and all maxima are clearly separated. Since the given PSFs are axially symmetric, the lower halves of the convolved images are very similar to the upper halves.

¹last image in 2nd row

Convolved

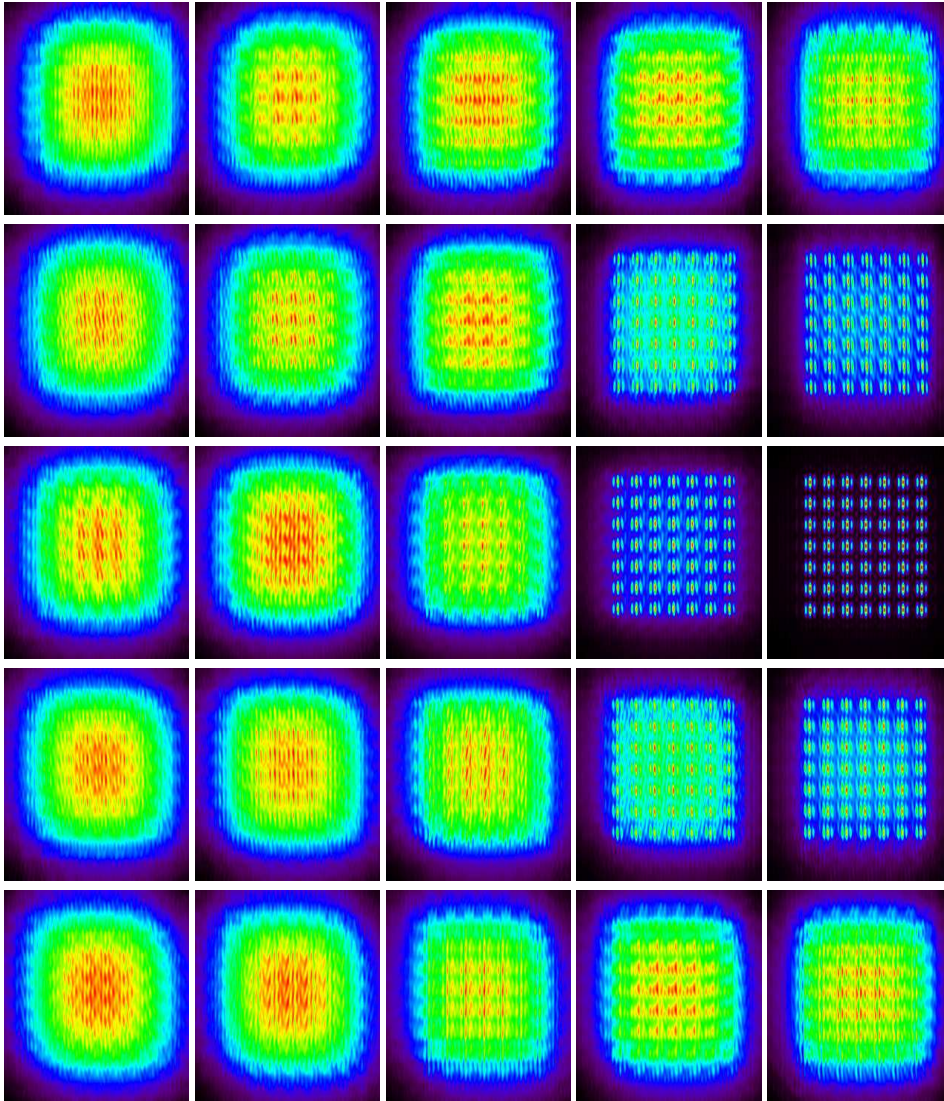


Fig. 3.4: Input image in 3.3 convolved with each PSF in figure 3.1:

These 25 convolved output images show the expected structures. The first convolved image (in the left top) shows only a smudged though rectangular structure. There is a noisy structure in the middle sector and the intensity seems to drop in a rectangular form towards the edges. No single sharp maxima is recognisable. This corresponds with low quality in the strehmap and the wide and unprecise PSF in figure 3.1. Along the first row towards the fifth convolved image, the image quality increases. Although more structures can be seen, the single points from the input image are only vaguely recognisable. The quality of the convolved images in the 2nd row are already better. Since the 6th convolved image (1st convolved image in 2nd row) is similar to the 5th, the 10th convolved image (last image in 2nd row) already allows to determine all the maxima from the input image. Also, the diffraction limited structure is recognisable. Especially in the middle the single maxima gets more smudged, but still each maxima is visible. For the 15th convolved pictures the best PSF is used. Best means that the PSF is small, sharp and shows the diffraction limited structures. Accordingly each maxima is recognisable with its diffraction limited form and all maxima are clearly separated. Since the given PSFs are axially symmetric, the lower halves of the convolved images are very similar to the upper halves.

3.3 Image generation

The edge length of the PSF extract is 250 pixel long and so is the input image, too. The convolved output image shall have the same edge length.

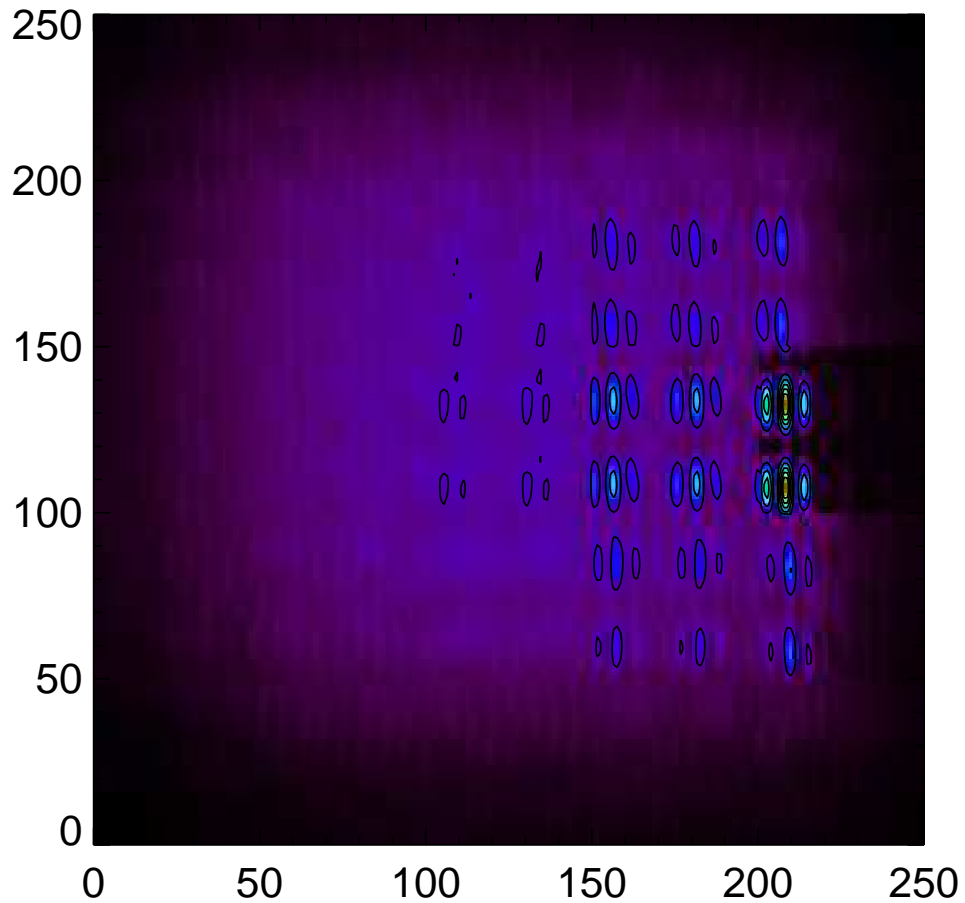


Fig. 3.5: Overall picture stitched together from convolved pictures from figure 3.4:

In order to get an overall picture with an edge length of also 250 pixel, each of the 25 convolved pictures are correspondingly stitched together. That means that from the first convolved picture in the first row a segment in x-direction from 1 to 50 pixel and in y-direction also 1 to 50 pixel is taken and is put in the segment of the overall picture in x-direction from 1 to 50 and in y from 1 to 50. Then from the second convolved picture in the first row a segment in x-direction from 50 to 100 pixel and in y-direction 1 to 50 pixel is taken and is put in the overall picture in x-direction 50 to 100 pixel and in y-direction 1 to 50 pixel. This is done until from each convolved picture the corresponding part is put in the overall picture.

In order to get an overall picture with an edge length of also 250 pixel, each of the 25 convolved pictures are correspondingly stitched together. That means that from the first convolved picture in the first row a segment in x-direction from 1 to 50 pixel and in y-direction also 1 to 50 pixel is taken and is put in the segment of the overall picture in x-direction from 1 to 50 and in y from 1 to 50. Then from the second convolved picture in the first row a segment in x-direction from 50 to 100 pixel and in y-direction 1 to 50 pixel is taken and is put in the overall picture in x-direction 50 to 100 pixel and in y-direction 1 to 50 pixel. This is done until from each convolved picture the corresponding part is put in the overall picture. This overall picture is shown in figure 3.5.

3.4 Transition smoothing

Since the input picture is convolved with each of the different PSFs, each convolved pictures looks different like shown in figure 3.4. As described in section 3.3 from each of these single convolved pictures a certain part is taken in order to generate an overall image. Because of this, the transitions between each of this partial pictures is not smooth. This effect is strengthened when the gradient in the strehmap in figure 3.2 changes rapidly. So when the images are stitched together the transitions needs to be smoothed in order to get a continuous output image. In figure 3.6 the stitch lines between the single parts of the overall image are shown. All transitions in x directions as well as in y directions must be smoothed. Since there are 4 transitions and 250 lines in each directions, 1000 transition smoothings must be performed per direction (2000 in sum).

In figure 3.7 exemplary, the cross section of the overall picture at $x = 75$ (red line) in figure 3.6 is shown. The cross section in $x = 75$ is shown in figure 3.7

At the four transition points 50, 100, 150 and 200, leaps are present, which means that the transitions are not continuous. Especially at the points 100, 150 and 200, the leaps are very clearly visible. In addition, the slope at the points 100 and 200 have different signs and switch from positive to negative at the point 100 and from negative to positive at the point 200. Although the slope at the point 150 is the same before and after the transition, there is a major gap in the functional value. It is a coincidence that at the point 50 the leap is smaller than at the other transition

points. In order to overcome this and obtain continuity, a smoothing algorithm must be applied. The principle of this so called cosine-bell function is explained in section 3.5.

After applying the cosine-bell function on the transitions, the cross section column of the overall picture at $x = 75$ is shown in figure 3.8. It can easily be seen that the transition points are smoother than before. Both slopes at each transition point show the same value before and after the transition and it is only a small leap at the point 200 left.

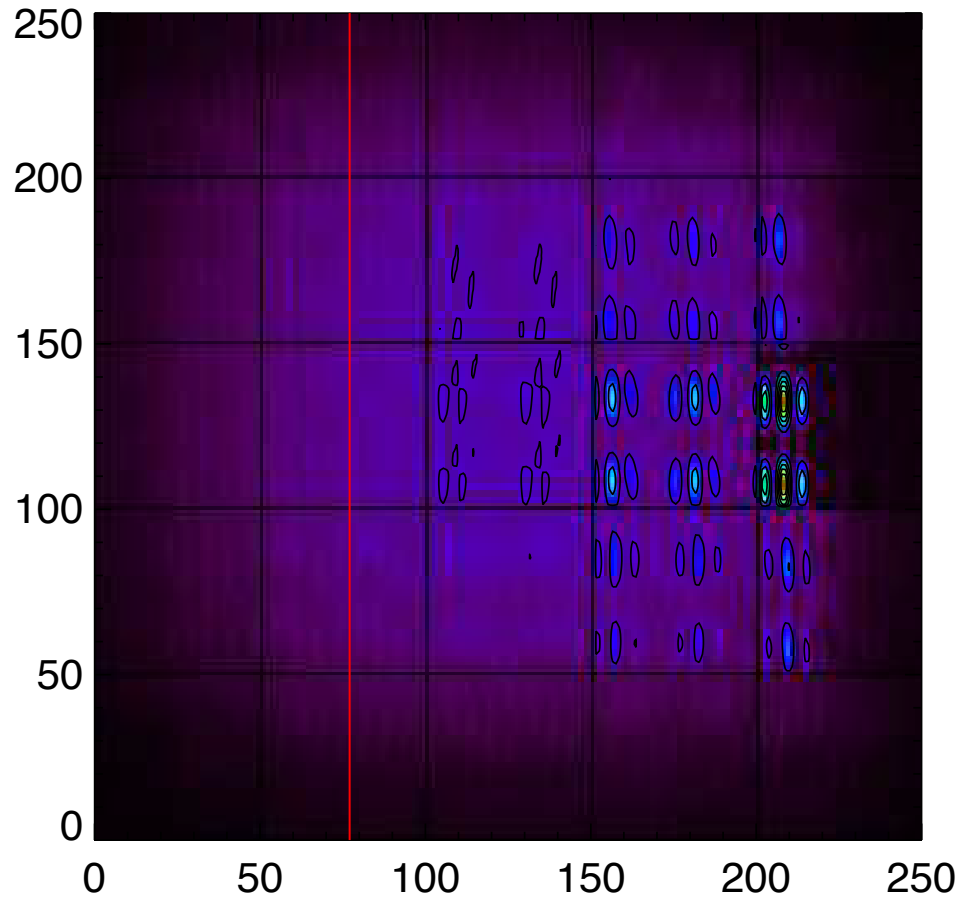


Fig. 3.6: Stitchpoint in the overall picture:

Exemplary, the column at the position $x = 75$ was chosen to demonstrate the leaps at the transition point in x-direction 50, 100, 150 and 200. Although the transitions seems to be smooth, the cross section figure 3.7 show the leaps at the transitions points.

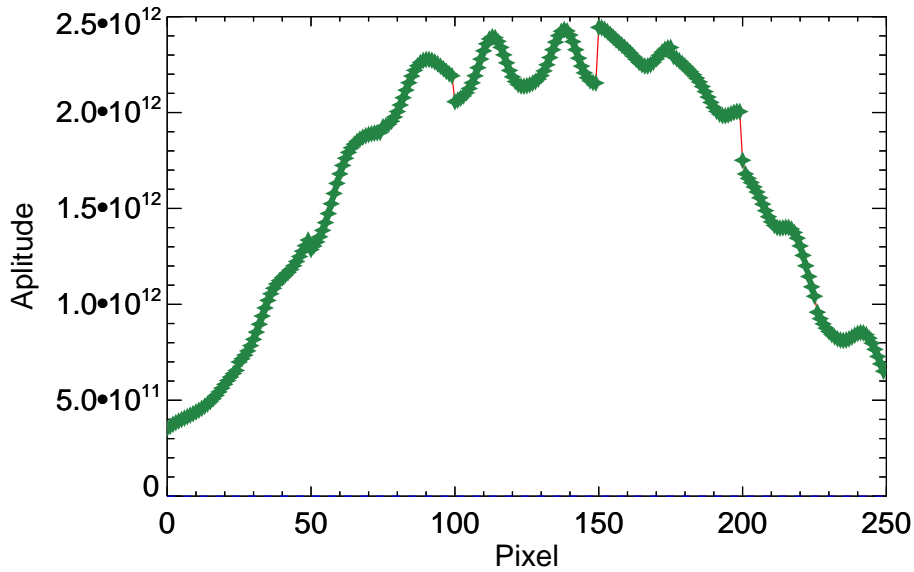


Fig. 3.7: Transition in column 75 of the overall picture:

At the four transition points 50, 100, 150 and 200, leaps are present, that means that the transition are not continuous. Especially at the points 100, 150 and 200 the leaps are very clearly visible. In addition the slope at the points 100 and 200 have different signs and switch from positive to negative at the point 100 and the from negative to positive at the point 200. Although the slope at the point 150 is the same before and after the transition, there is a major gap in the functional value. It is a coincidence that at the point 50 the leap is smaller than at the other transition points.

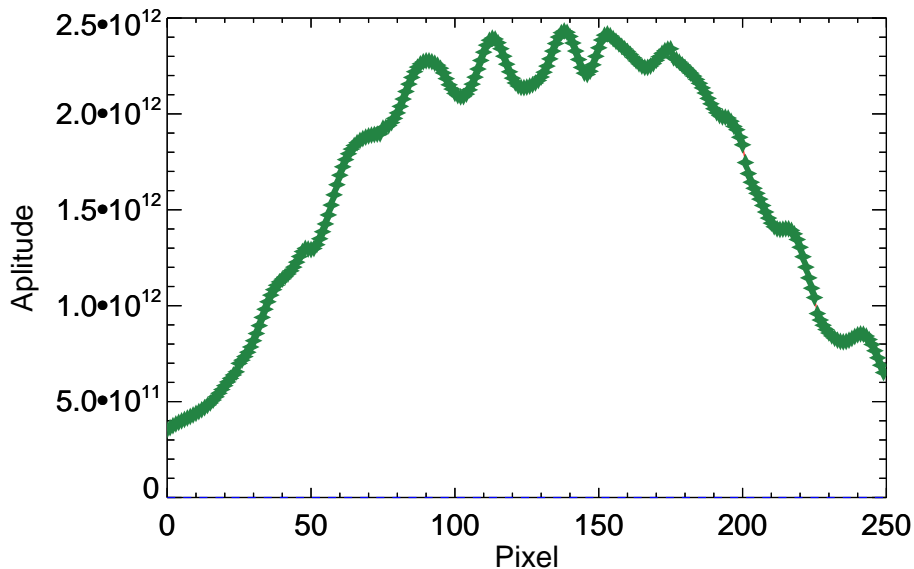


Fig. 3.8: Smoothed transition in row 75 of the overall picture:

After applying the cosine-bell function on the cross section of the overall picture at $x = 75$, it can easily be seen that at the transition points are smoother than before. Both slopes at each transitions show the same value before and after the transition and it is only left a small leap at the point 200.

Finally, after applying the cosine-bell function to all transitions for both x and y direction the final convolved and stitched together picture is shown in figure 3.9. Corresponding to the strehlmap and the 25 single PSF the smoothed final output image shows the expected structure. On the left side of the image, where the Strehl ratio is very low, the single input points are not recognisable. In the middle part the image quality increases and some structures are shown but the results are not conclusive. In the middle right part, the diffraction limited image of the point can clearly be seen. In contrast to the un-smoothed image in figure 3.5 there are less hard edges and the transition points are no longer recognisable.

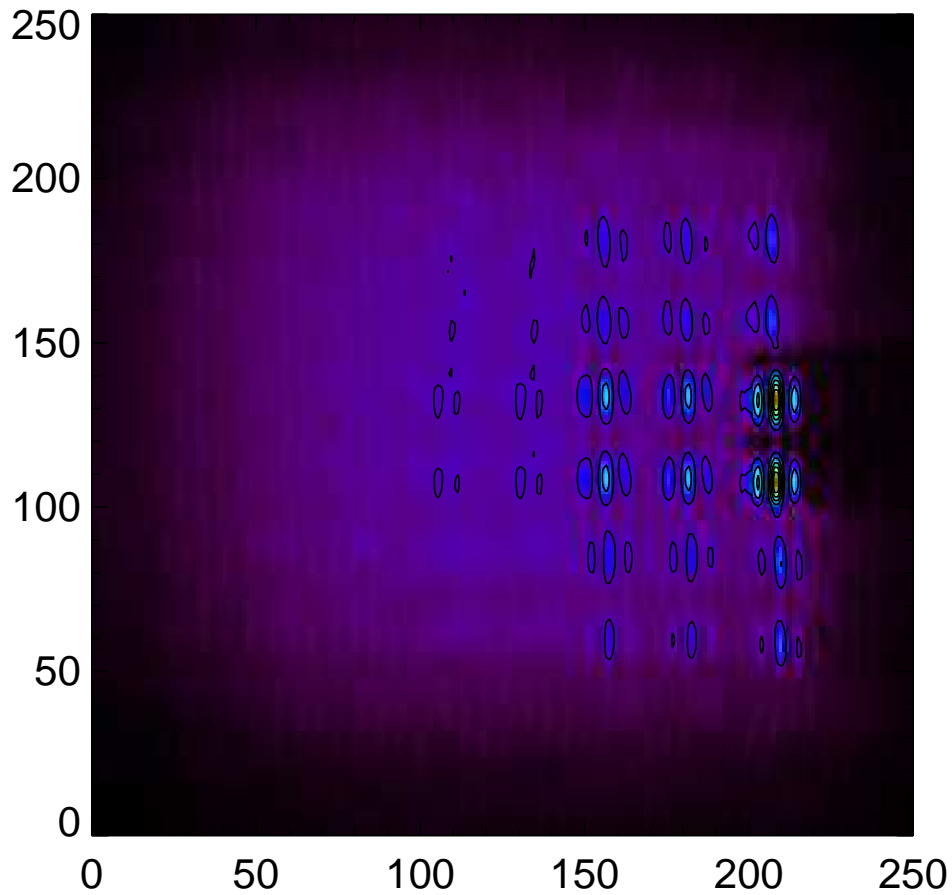


Fig. 3.9: Final overall picture with smoothed transitions:

Finally, after applying the cosine-bell function to all transitions for both x and y direction the final convolved and stitched together picture is shown in figure 3.9. Corresponding to the strehmap and the 25 single PSF the smoothed final output image shows the expected structure. On the left side of the image, where the Strehl ratio is very low, the single input points are not recognisable. In the middle part the image quality increases and some structures are shown but the results are not conclusive. In the middle right part, the diffraction limited image of the point can clearly be seen. In contrast to the un-smoothened image in figure 3.5 there are less hard edges and the transition points are no longer recognisable.

3.5 Cosine-bell function

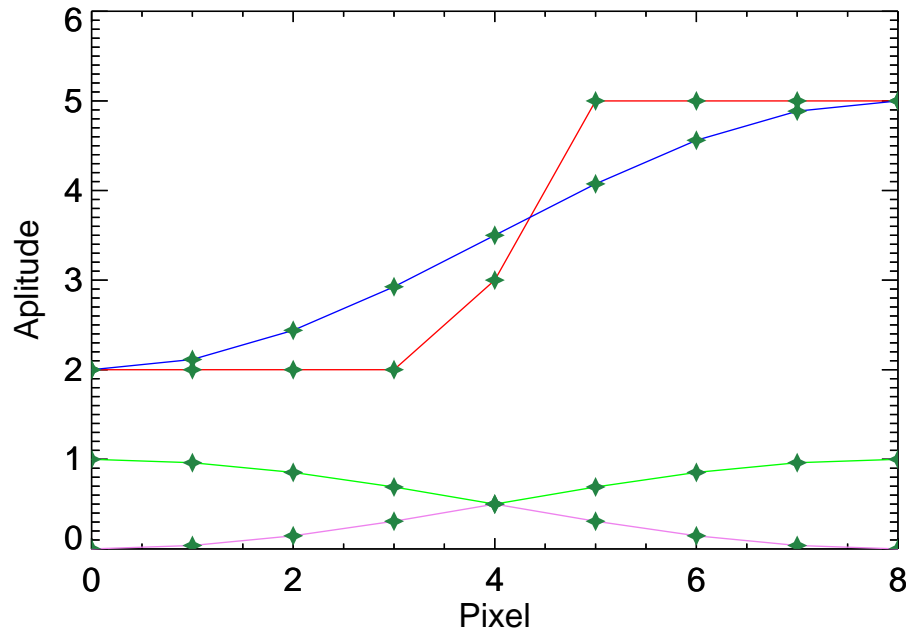


Fig. 3.10: The principle of the cosine-bell-function: Red line: unprocessed original input data

Blue line: smoothed, cosine-bell-function applied output data

Green line: 1st cosine-function

Purple line: 2nd cosine-function

Principle: the algorithm goes from left to right. To evaluate the value at each step m over a smoothing width of n , the functional value of the input data (red line) at the point m is multiplied with 1st cosine function at the point m , the value of $(m - n)^{th}$ value is multiplied with 2nd cosine-bell functions at the point $m - n$ and the sum of this both results gives the new output value (blue line) at the point m

The purpose of the cosine-bell-function is to smooth the transition between composed parts of an image. Therefore, two cosine functions of the period of $\frac{\pi}{2}$ with an offset of +1 are taken

$$f_1(x) = \frac{\cos(x \cdot s \cdot \pi) + 1}{2}, \quad (3.1)$$

$$f_2(x) = \frac{\cos(\pi(x \cdot s + 1)) + 1}{2}, \quad (3.2)$$

with the step length s :

$$s = \frac{1}{n-1}$$

In figure 3.10 is an example with 9 points (red line) shown. In this plot, also the two cosine functions can be seen. The smoothing procedure works as follows:

- ▶ the algorithm goes through the array (red line), starting on the left side ($n=0$)
- ▶ the first element $n=0$ is multiplied with first cosine function (green line, value 1) plus the last element n multiplied with the second cosine function (purple, value 0),
- ▶ in the next step, the element $n=1$ of the array is multiplied with the first cosine function at $n = 1$ (green line) plus the $(n-1)^{\text{th}}$ element of the array multiplied with the second cosine function (purple) at the point $n-1$. This is the new value (blue line) at the point n ,
- ▶ both cosine functions are mirrored at the middle of the array,
- ▶ the so smoothed function can be seen in figure 3.10 (blue line).

The cosine-bell algorithm must perform on a certain overlap at the transition point. The width of the overlap depends on each case. On the one hand, the width of the overlap must not be too big, since the cosine-bell function smoothes the overlap and thereby it annihilates information at this point. On the other hand the width must not be too small at deep decent in order to create a gentle transition. In all simulations, the width of the overlap was 50 pixels, 25 in each sub-image. In general the cosine-bell algorithm calculates the average values between two points by taking into consideration the position between the start and end point. This consideration has the effect that the average value is weighted.

3.6 Galactic Center - low resolution

To get a better understanding which effect different PSF setups and input images have on the quality of the output image, in this next simulation, the input picture is a 10" x 10" caption of the Galactic Center (section 3.11) in a lower resolution. The image size is 2000 x 2000 pixel.

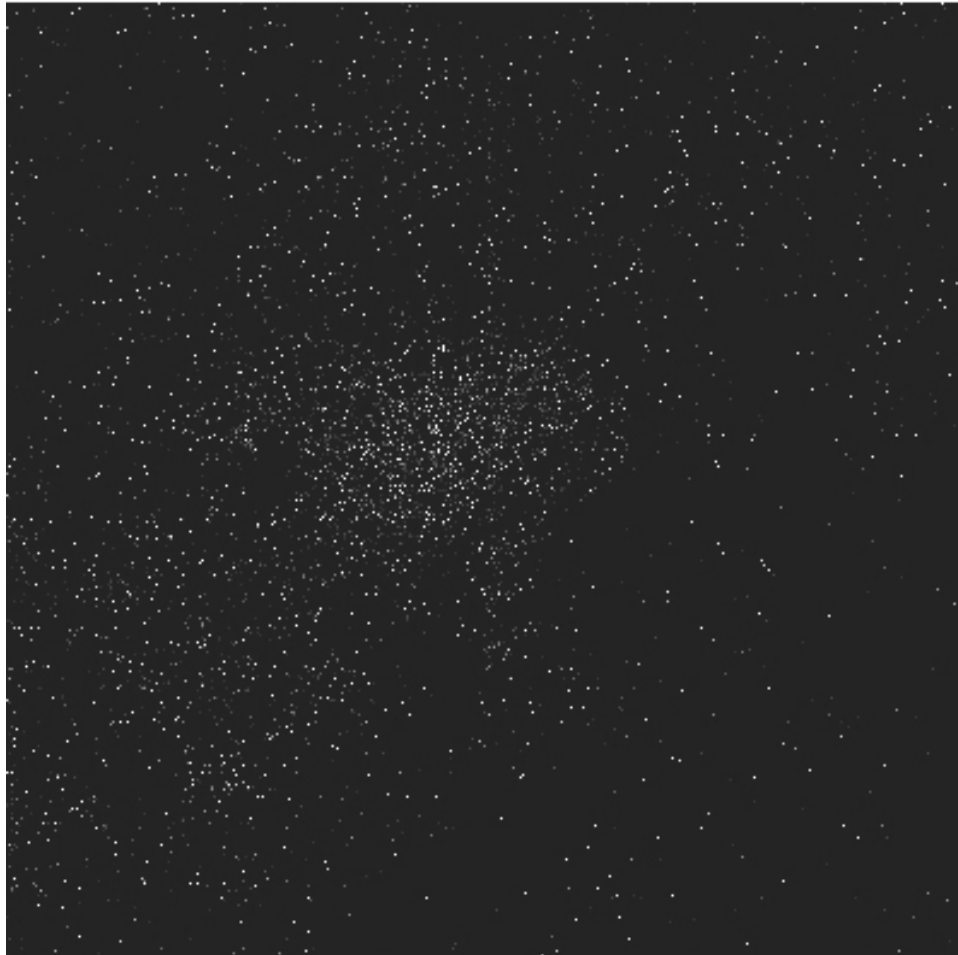


Fig. 3.11: Low resolution 10" x 10" detail pictures of the Galactic Centre in a resolution of 2000 x 2000 pixel

The configuration of this simulation is the same as in section 3.1, but the posi-

tion of the guiding star is in the centre of the FoV. The simulation generated also a 5 x 5 grid of PSFs which are shown in figure 3.12. The 25 PSFs comply with the specification that the NGS is positioned in the centre of the FoV. The central PSF (the 13th or 3rd PSF in 3rd row) shows a clear diffraction limited structure. The central and the two secondary maxima are clearly distinguishable and the structure is hardly smudged. This observation also applies for the eight directly adjacent PSFs: the diffraction limited structure is also clearly recognisable, whereby the structure is a little more smudged.

PSFs

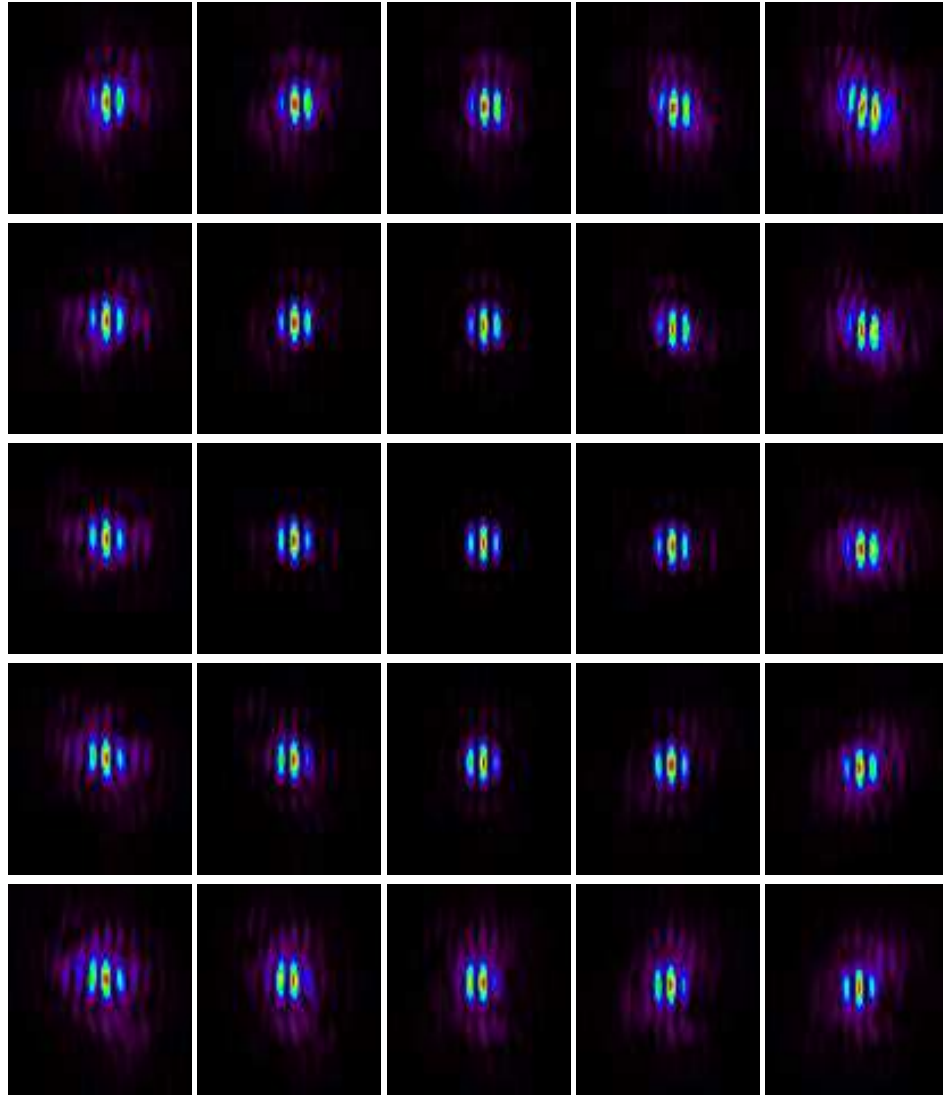


Fig. 3.12: 5x5 simulated PSFs with a centered NGS:

The 25 PSFs comply with the specification that the NGS is positioned in the centre of the FoV. The central PSF (the 13th or 3rd PSF in 3rd row) shows clearly a diffraction limited structure. The central and the two secondary maxima are clearly distinguishable and the structure is hardly smudged. This observation also applies for the eight directly adjacent PSFs: the diffraction limited structure is also clearly recognisable, whereby the structure is a little more smudged. Also the outer lying PSFs show a central and mostly secondary maxima, but as expected the structures are more smudged. In general, the shown PSFs have a high quality.

Also the outer lying PSF show a central and mostly secondary maxima, but as expected the structures are more smudged. In general, the shown PSFs are of a high quality.

The final stitched picture is shown in figure 3.13. The given image shows the expected structure: the central part shows detailed structures and the diffraction limited images of the point sources are recognisable. Radial outward going, the image quality decreases and although still diffraction limited sources can be seen, these structures are more smeared.

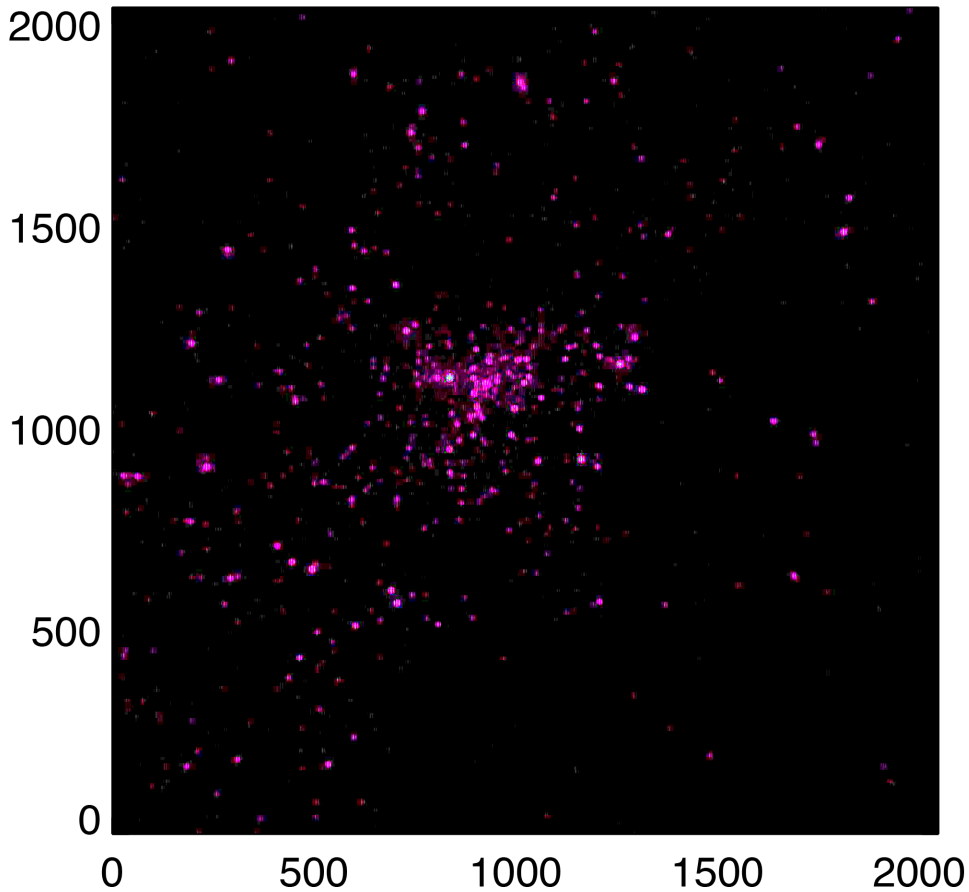


Fig. 3.13: 10" x 10" detail around the Galactic Center in low resolution:

The given image show the expected structure: the central part shows detailed structures and the diffraction limited images of the point sources are recognisable. Radial outward going the image quality decreases and although still diffraction limited sources can be seen, these structures are more smeared.

3.7 Galactic center - high resolution

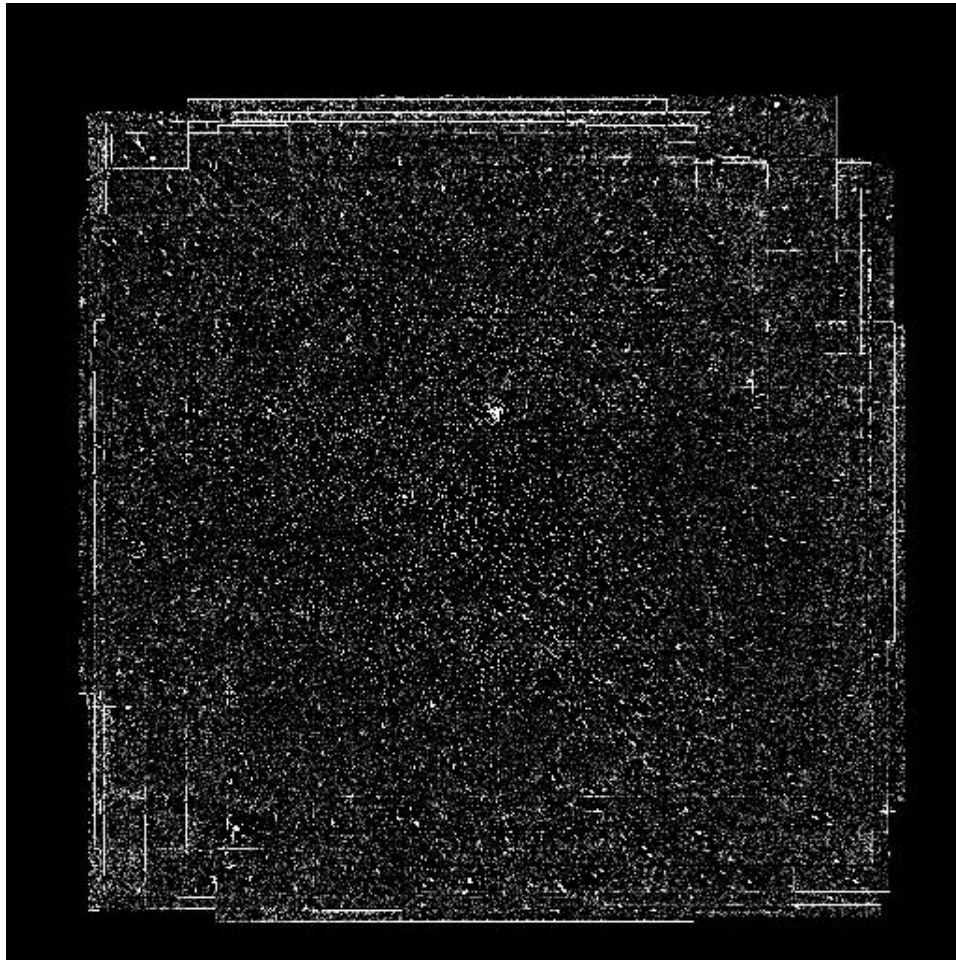


Fig. 3.14: 10" x 10" detail around the Galactic Centre in higher resolution

In this case, a high resolution 10" x 10" detail picture (figure 3.14) of the Galactic Centre is convolved with the same PSFs like in section 3.6. The simulated PSFs are shown in figure 3.12 and the image quality of the single convolved images is correlated with these PSFs and are shown in figure 3.15: The image in the centre shows detailed structures and single sources are recognisable.

Convolved

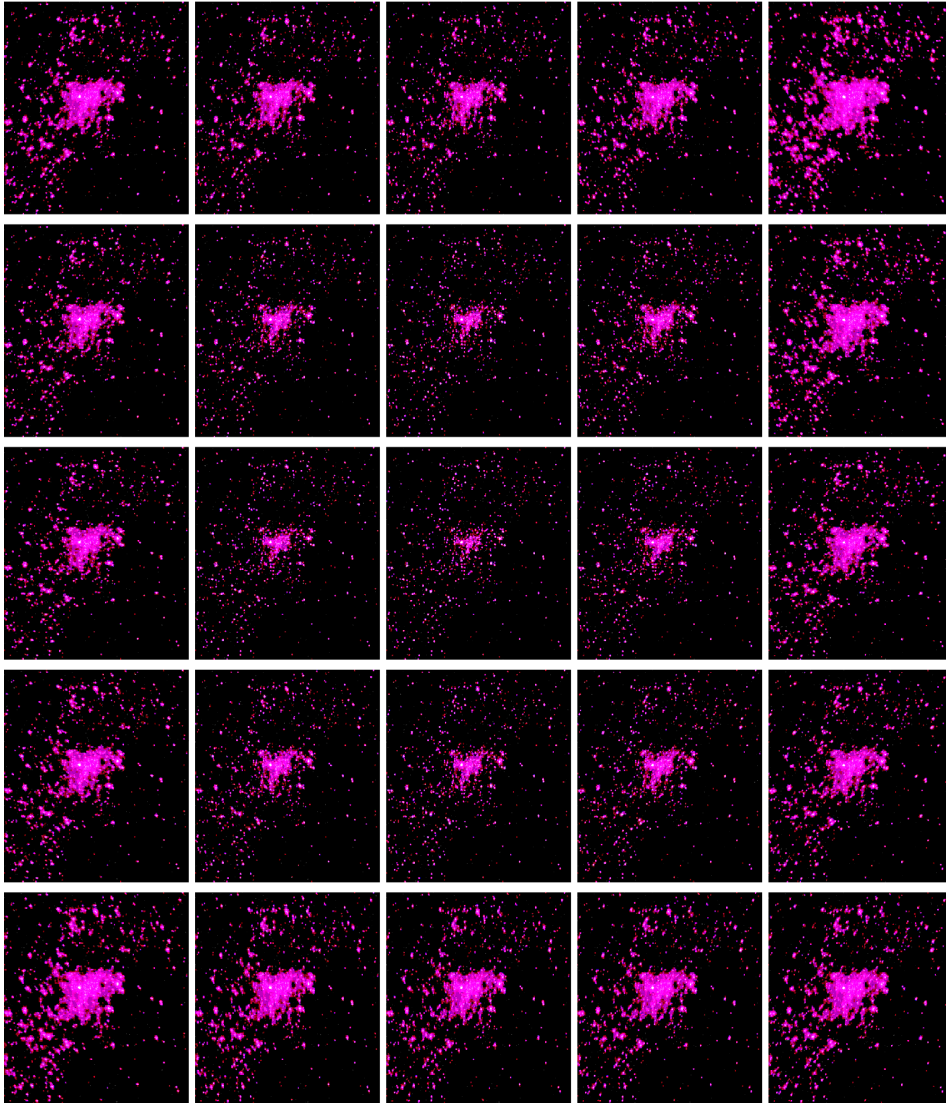


Fig. 3.15: Convolution with a low resolution picture of the gc (Fig. 3.11) and the PSFs in (3.12): The image quality of the single convolved images is correlated to the PSFs shown in figure 3.12: The image in the centre show detailed structures and single sources are recognisable. This good image quality also applies for the eight directly adjacent images: detailed structures are also given, although the structure in the centre starts to smear. This effect of smearing increases for the outwards images and instead of single sources the centre structure becomes mashed up.

This good image quality also applies for the eight directly adjacent images: detailed structures are also given, although the structure in the centre starts to smear. This effect of smearing increases for the outwards images and instead of single sources the centre structure becomes mashed up.

Each PSF has the image size of 2000 x 2000 pixels and shows a 10" x 10" detail around the Galactic Centre.

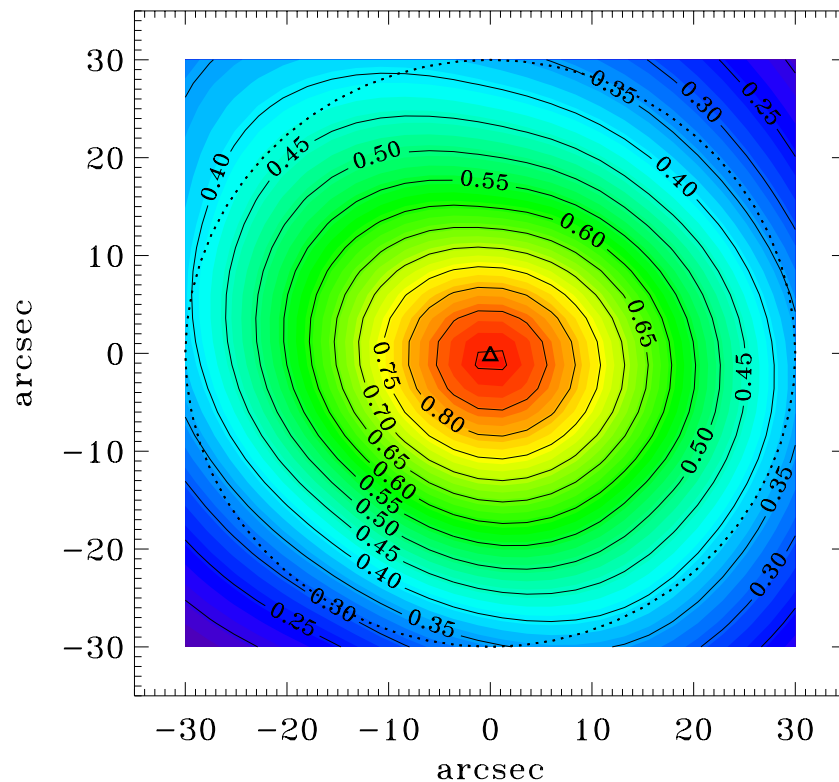


Fig. 3.16: Strehlmap corresponding to PSFs in figure 3.12:

The Strehl ratio goes up to 90 % in the middle and falls circular to a value of 20 % to 25 %. The strehlmap is extremely symmetric and of very good quality. It must be considered that atmospheric and instrumental effects hardly cause disturbance while imaging through the central arcsecs with a Strehl ration of about 90 %. Although such a good strehlmap is unrealistic under normal observing conditions, convolving the corresponding PSFs with the input image helps understanding the influences of atmospheric and instrumental effects on imaging.

The corresponding strehlmap is shown in figure 3.16. The strehl ratio goes up to 90 % in the middle and falls circular to a value of 20 % to 25 %. The strehlmap is extremely symmetric and of very good quality. It must be considered that atmospherical and instrumental effects hardly cause disturbance while imaging through the central 10 arcsecs with a strehl ration of about 90 %.

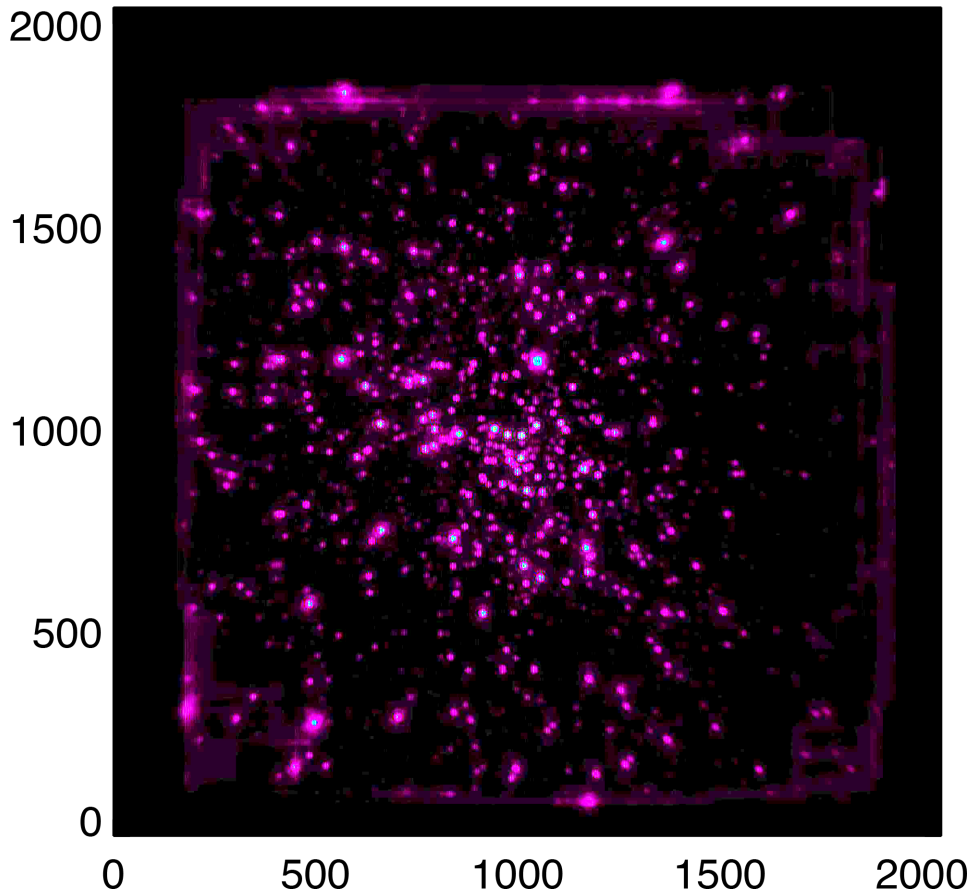


Fig. 3.17: 10" x 10" detail of the Galactic Centre in high resolution. Fig. 3.14 convolved with Fig. 3.12:

Since the PSF quality is extremely good, the convolved image shows in the central part diffraction limited images of single point sources. The output image quality decreases radially outwards. When comparing with the original input picture in 3.14 one can see that although the PSF quality is very good, a lot of details cannot be reconstructed in the convolved output image.

Although such a good strehlmap is unrealistic under normal observing conditions, convolving the corresponding PSFs with the input image helps understanding

the influences of atmospherical and instrumental effects on imaging.

The final convolved output picture is shown in figure 3.17. Since the PSF quality is extremely good, the convolved image shows diffraction limited images of single point sources in the central part. The output image quality decreases radially outwards. When comparing with the original input picture in 3.14 one can see that although the PSF quality is very good, a lot of details cannot be reconstructed in the convolved output image.

3.8 De-convolution

The convolved output images 3.13 and 3.17 show the simulated results after imaging through atmosphere and instrument. The final goal however is to get the original input image. In our simulated cases of course these images are given in 3.11 and 3.14 but the purpose of an actual observation is to obtain these very input images. Therefore a de-convolution of the output image must be performed.

The deconvolution method via lucy is described in section 2.4. The speciality of the simulation of various science cases in section 3.9 is that five different parallactic angles are simulated. The goal was to create one averaged initial picture after de-convolution. In order to achieve this, an own version of the lucy-algorithm was implemented. The fundamental function of the lucy-algorithm were kept, but there were three main differences:

1. Only 10 iteration were performed.
2. The correction factor $R_k(x, y)$ in equation 2.4 is computed for each parallactic angle and than averaged.
3. The new estimated image O_{k+1} in equation 2.5 is multiplied with an averaged correction factor.

3.9 Simulation of various science cases

In the next simulation setup, two guiding stars were implemented: IRR1 and IRR2 (see tab 3.1). Additionally, five different parallactic angles were simulated in order

to get an averaged original input picture during the deconvolution process (see tab 3.2). The single Strehl maps for the five different parallactic angles are shown in figure 3.18.

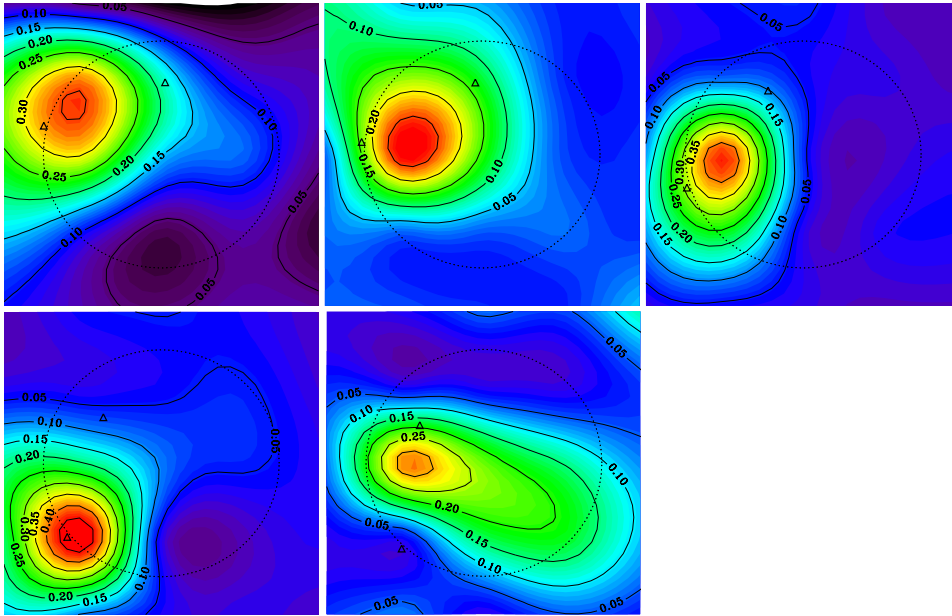


Fig. 3.18: Strehlmaps for the 5 different parallactic angles:

- 1st image (1st image in 1st row): -30.783°
- 2nd image (2nd image in 1st row): -24.698°
- 3rd image (3rd image in 1st row): 0°
- 4th image (1st image in 2nd row): 30.783°
- 5th image (2nd image in 2nd row): 24.698°

In the first step, the input picture of the galactic centre in high resolution with embedded science cases (fig 3.19, left image) is convolved with the PSF already used in section 3.6. The picture composition process is explained in section 3. The results for the five parallactic angles are shown in figure 3.20. After the deconvolution, like described in section 3.8, this resulting image is convolved with a gaussian function, since all point sources appear as gaussian or airy shaped sources. The final results are shown in the right figure in 3.19.

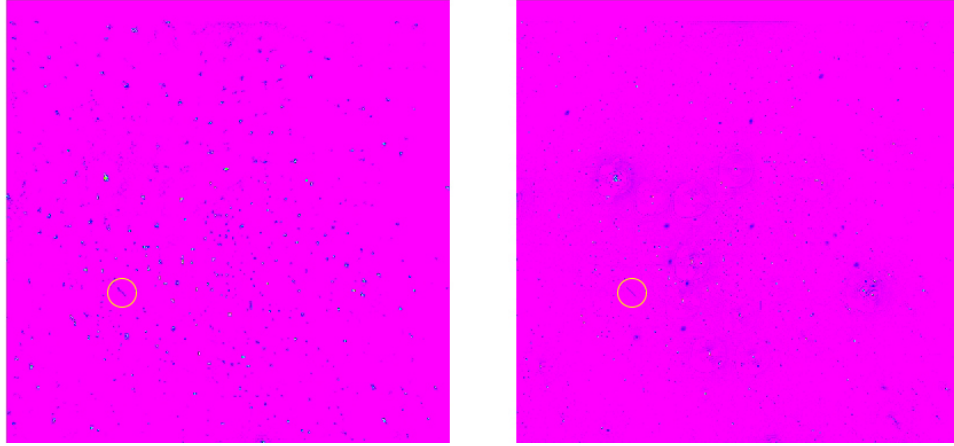


Fig. 3.19: Left: Output picture after de-convolving.
 Right: Input picture of Galactic Center in high resolution with science cases (both: 10" x 10" detail in 2000 x 2000 pixel resolution)
 The, to be analysed, science cases are marked in figure 4.1 and discussed in chapter 4. Although the single cases are discussed later, one science case (thin dusty filaments, in section 4.3) is marked with a yellow circle in order to show that these structures are still present after the de-convolving process.

Tab. 3.1: Optical reference stars.

Star	α	β	Magnitude
IRR1	$17^h 45^{min} 40^{sec}.07$	$-29^\circ 00' 27''.5$	13.7 mag
IRR2	$17^h 45^{min} 40^{sec}.21$	$-29^\circ 00' 25''.2$	13.2 mag

Tab. 3.2: Simulated parallactic angles.

	Parallactic angle	Altitude
1	-30.783°	20°
2	-24.698°	24°
3	0°	28.298° (max. altitude)
4	24.698°	24°
5	30.783°	20°

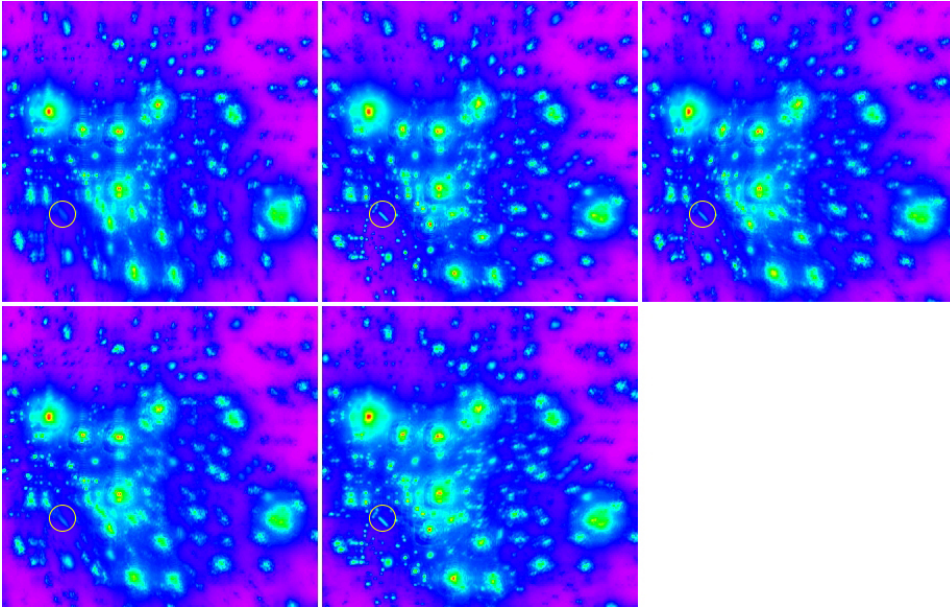


Fig. 3.20: Image of the convolved Galactic Centre ($10'' \times 10''$ detail in 2000×2000 pixel resolution).

The convolved images of the Galactic Centre are shown for 5 different parallactic angles:

1st image (1st image in 1st row): -30.783° ,

2nd image (2nd image in 1st row): -24.698° ,

3rd image (3rd image in 1st row): 0° ,

4th image (1st image in 2nd row): 30.783° ,

5th image (2nd image in 2nd row): 24.698° .

The yellow circles show thin dusty filaments (discussed in section 4.3). It can be seen that for each parallactic angle these structures are present, although the image quality differs for the parallactic angles. In the 2nd and 5th image the structure is clearly recognisable. The 3rd image shows this structure, but is more smudged. In the 1st and 4th image still a maxima is visible, but is hardly discernible as a linear structure.

Science cases

In order to verify astrophysical hypotheses, it is crucial to compare theoretical results with actual astronomical measurements. Not only the measurements themselves, but also the measurement errors are of great interest. Since a great number of hypotheses require very precise measurements, it is important to understand how adequately proper motions of celestial objects can be reconstructed after observing through Earth's atmosphere. The proper motion of celestial objects is easily calculated by

$$v = \frac{s}{t}. \quad (4.1)$$

The measurement of t can be considered without error since the exposure time (scale of seconds to minutes) is much smaller than the period of time between the single measurements (scale months to years). The measurement of s however contains errors. These errors are caused by atmospherical disturbances and aberrations of the instruments. Although adaptive optics can correct atmospherical disturbances of course certain errors remain. The result of the sum of all errors causes that the point sources are smudged. Mathematically, this leads to an accordingly wider or narrower gaussian form. Concerning the proper motion of celestial objects, this error can be written in a gaussian error propagation:

$$\Delta v = \frac{\Delta s}{t}. \quad (4.2)$$

In this chapter, various science cases which were placed in the input image of the Galactic Centre, their recoverability after the convolving and de-convolving process and the occurring errors while recovering are investigated. Each science case also is put in context of current scientific research.

The input, convolved and re-convolved images have a resolution of 2000 x 2000 pixel each and show 10" x 10" detail around the Galactic Centre. All performed position determinations are given in pixel relative to the image section. The error of the position determination is also given in pixel, but can easily be converted in angular units with the relation:

$$5 \text{ mas} = 1 \text{ pixel}, \quad (4.3)$$

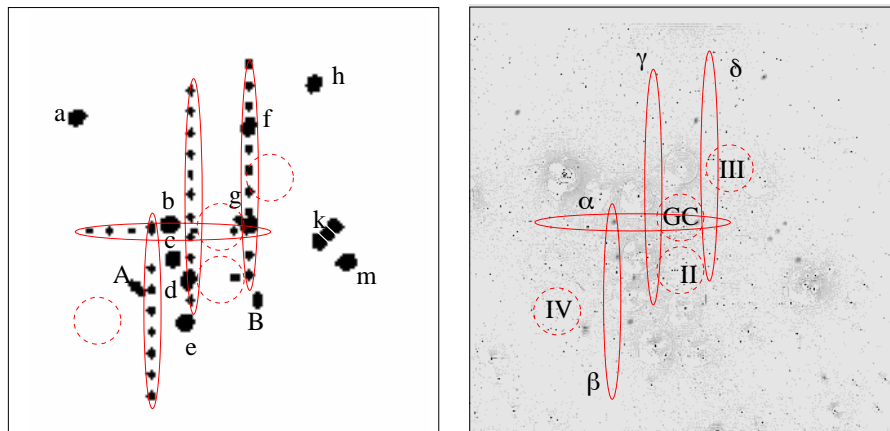


Fig. 4.1: Science Cases, 10" x 10" detail around the Galactic Centre:

α, β, γ and δ : Proper motions,
 GC, II, III and IV: small stellar associations,
 A and B: Thin dusty filaments,
 a, b, c, d, e, f, g, h and m: disk embedded sources,
 k: cometary and asymmetric bow-shock sources.

4.1 Proper motions of stars within the central stellar cluster

Along the four stripes α , β , γ , and δ in figure 4.1 up to 12 sources were positioned at equidistant separations from each other. The source along the stripe β pass the highest stellar density whereas all other stripes contain a significant portion of sources the pass through the Galactic Centre region in which the projected stellar density is very high. This simulation will allow to demonstrate how well

the stellar positions can be extracted after the interferometric observations and the image reduction described here. This is best done by plotting the known input positions against the retrieved stellar positions followed by a determination of the uncertainties that result if one derives proper motion information from the final reconstructed images. See figures 4.2, 4.3, 4.4 and 4.5. The measured points in the input and re-convolved output image are plotted in the figure 4.7 and listed in tab. 4.1, tab. 4.2, tab. 4.3 and tab. 4.4. One can see that in stripe α the position in x-direction is reproduced very well, since the y-components vary. This can be seen better in figure 4.7a. For the stripes β (figure 4.7b), γ (figure 4.7c) and δ (figure 4.7d) it is similar, but in these cases the y-components can be reproduced well and the x-components vary. It is important to mention that although in the input image all points are placed in a line (red line), the linearity can not always be determined. The reason therefore is that in very dense regions the placed points are difficult to find. The gaussian fit is performed for a $10 \text{ px} \times 10 \text{ px}$ area around the known position of the input points. In cases where multiple sources are in this area, the gaussian function may fit another source and performs the fit accordingly.

In Parsa et al. (2017) the physics close to a supermassive black hole (SMBH) are studied. Using the three stars S2, S38 and S55/S0-102 with the shortest period and applying Newtonian models the mass of and the distance to Sgr A* are $M_{BH} = (4.15 \pm 0.13 \pm 0.57) \times 10^6 M_{\odot}$ and $R_0 = 8.19 \pm 0.11 \pm 0.34 \text{ kpc}$. In order to test general relativity, precise measurements are required. Beside the mass of Sgr A* and the distance to it, also the stellar orbits must be determined.

In 2002, the periapses passage S2 has been studied by near-infrared (NIR), adaptive optics and lead to a more detailed Keplerian orbital elements.

The mass of the SMBH can also be determined precisely by observing the orbit of S38. S38 is well suited for examination since most of its orbit is to the less crowded west of Sgr A*.



Fig. 4.2: Stripe α

. Top: Original Image, Bottem: Re-Convolved Image. Each image shows a detail of $3.6'' \times 0.1''$.

S55/S0-102 has a period of only ≈ 12 years and is therefore also suited for investigating the mass and distance of Sgr A*. (Parsa et al. 2017, P. 2). The astrometric data is plotted and compared to newtonian and relativistic simulations of the orbit. In order to interpolate the orbit from the astrometric data the error of the right ascension and the declination must be considered.



Fig. 4.3: Stripe β
 Left: Original Image, Right:
 Re-Convolved Image. Each
 image shows a detail of $0.1''$
 $\times 4.1''$



Fig. 4.4: Stripe γ
 Left: Original Image, Right:
 Re-Convolved Image. Each
 image shows a detail of $0.1''$
 $\times 5.6''$

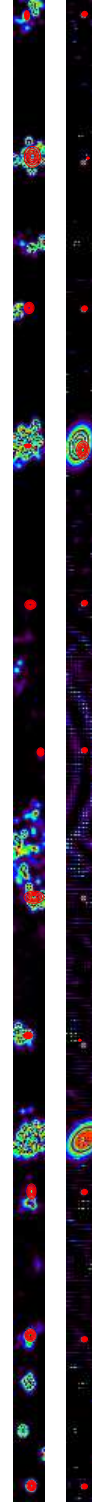


Fig. 4.5: Stripe δ
 Left: Original Image, Right:
 Re-Convolved Image. Each
 image shows a detail of $0.1''$
 $\times 5.1''$

Fig. 4.6: Mean value for \bar{y} and error Δy in table 4.5 and point coordinates (red circles) in tab. 4.1

Tab. 4.1: Point coordinates for stripe α including 1σ -gauss-error.

Input		Output	
(X Y) [px]	(ΔX ΔY) [px]	(X Y) [px]	(ΔX ΔY) [px]
(11.02 10.00)	(0.8786 0.8380)	(12.39 10.11)	(1.531 1.475)
(111.0 10.00)	(0.8493 0.8493)	(108.5 13.18)	(1.763 1.608)
(211.0 9.992)	(0.8540 0.8557)	(210.7 10.43)	(1.436 1.816)
(311.0 9.998)	(0.8670 0.8716)	(310.6 9.013)	(1.441 1.200)
(411.0 10.00)	(0.8526 0.8490)	(409.9 10.80)	(1.484 1.511)
(511.0 10.01)	(0.8600 0.8705)	(509.6 10.34)	(1.678 2.542)
(611.0 10.01)	(0.8556 0.8651)	(610.1 9.983)	(1.456 1.886)
(717.0 14.75)	(0.2623 0.3793)	(716.6 13.78)	(0.5940 2.620)

Tab. 4.2: Point coordinates for stripe β including 1σ -gauss-error.

Input		Output	
(X Y) [px]	(ΔX ΔY) [px]	(X Y) [px]	(ΔX ΔY) [px]
(11.00 10.00)	(0.8493 0.8493)	(11.38 9.643)	(1.583 1.516)
(10.99 110.0)	(0.8529 0.8457)	(11.17 109.0)	(1.943 1.572)
(11.00 210.0)	(0.8514 0.8493)	(10.98 210.4)	(1.329 1.734)
(11.00 310.0)	(0.8513 0.8511)	(10.16 309.2)	(1.948 1.531)
(10.99 410.0)	(0.8603 0.8504)	(9.751 411.0)	(1.391 2.399)
(10.98 510.0)	(0.8749 0.8755)	(11.02 509.4)	(2.201 1.535)
(8.438 617.0)	(0.3572 0.2306)	(9.964 616.6)	(1.953 0.6144)
(13.63 708.0)	(0.5390 0.2833)	(12.32 708.1)	(1.795 1.364)
(10.99 810.0)	(0.8605 0.8566)	(10.90 807.8)	(1.347 1.088)

4.2 Small stellar associations

A special interest is devoted to small stellar associations like the central about 1 arc-second diameter high velocity cluster around the super massive black hole Sgr A* (the so called S-cluster) or the small compact association IRS13E that is a candidate for harbouring an intermediate mass black hole. Here, it is of interest to

Tab. 4.3: Point coordinates for stripe γ including 1σ -gauss-error.

Input		Output	
(X Y) [px]	(ΔX ΔY) [px]	(X Y) [px]	(ΔX ΔY) [px]
(11.00 9.999)	(0.8510 0.8510)	(13.02 10.96)	(1.318 1.416)
(10.90 109.9)	(0.9359 0.9491)	(10.13 109.2)	(1.402 1.624)
(10.01 210.4)	(1.895 2.301)	(8.334 207.7)	(0.3456 0.9495)
(13.89 317.0)	(0.4525 0.2960)	(17.65 307.5)	(0.4065 0.7489)
(10.99 410.0)	(0.8790 0.8515)	(10.91 408.5)	(1.325 1.502)
(11.00 510.0)	(0.8493 0.8493)	(17.50 507.3)	(0.7832 0.3685)
(11.00 610.0)	(0.8493 0.8512)	(17.65 607.3)	(0.4713 0.4331)
(10.94 710.0)	(0.9102 0.7847)	(16.24 715.9)	(1.637 1.378)
(11.00 810.0)	(0.8558 0.8543)	(15.29 813.2)	(1.811 2.682)
(11.02 909.9)	(0.8607 0.9293)	(10.27 910.6)	(1.602 3.237)
(11.00 1010.)	(0.8493 0.8493)	(14.04 1008.)	(1.331 1.111)
(11.02 1110.)	(0.8741 0.8605)	(12.01 1116.)	(1.356 1.254)

Tab. 4.4: Point coordinates for stripe δ including 1σ -gauss-error.

Input		Output	
(X Y) [px]	(ΔX ΔY) [px]	(X Y) [px]	(ΔX ΔY) [px]
(11.00 10.00)	(0.8500 0.8500)	(11.26 10.53)	(1.410 1.770)
(11.00 110.0)	(0.8611 0.8633)	(10.60 112.6)	(1.735 2.115)
(11.00 210.0)	(0.8496 0.8494)	(11.26 210.3)	(1.442 2.654)
(8.203 313.0)	(0.3102 0.2281)	(9.167 316.2)	(1.338 1.107)
(17.92 407.0)	(0.3205 0.2720)	(12.81 410.1)	(3.225 2.168)
(10.99 510.0)	(0.8627 0.8603)	(16.93 508.7)	(1.116 1.462)
(11.00 610.0)	(0.8507 0.8505)	(10.60 608.8)	(1.779 1.635)
(9.899 713.8)	(1.998 3.253)	(8.977 716.6)	(1.086 0.4954)
(11.00 810.0)	(0.8493 0.8493)	(9.816 810.3)	(1.530 1.991)
(13.21 912.0)	(0.3182 0.2541)	(11.87 912.9)	(2.631 3.732)
(11.00 1010.)	(0.8493 0.8493)	(8.413 1009.)	(0.6670 1.544)

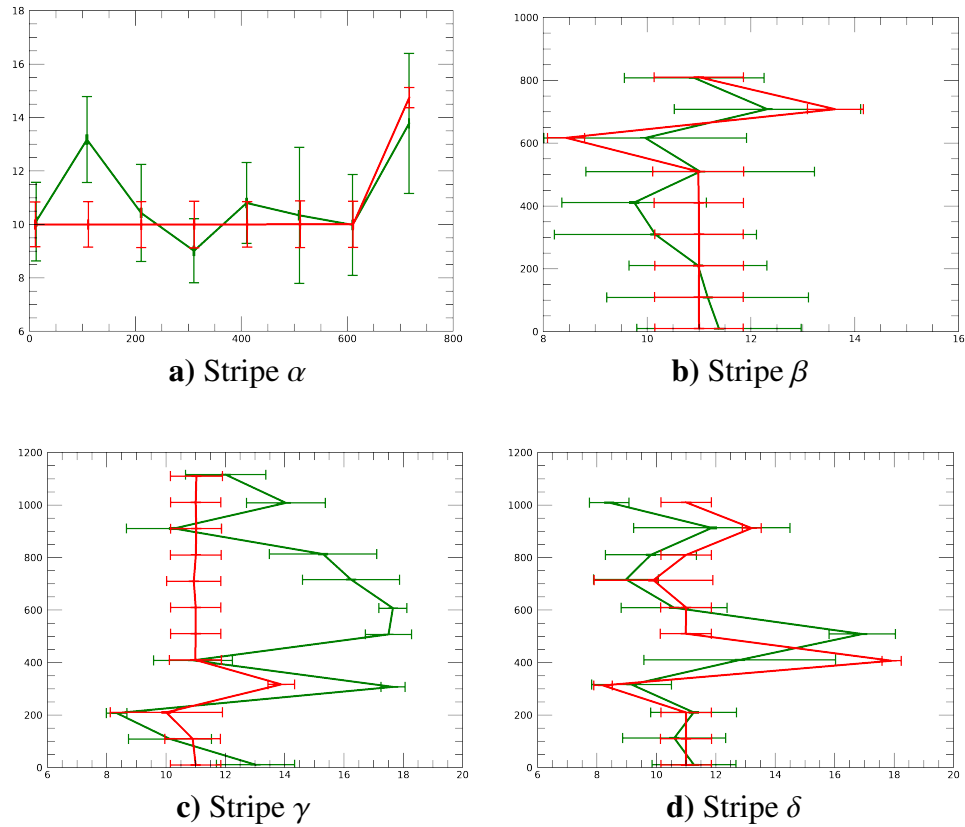


Fig. 4.7: Measured point with 1σ -gauss-errors of stripes α , β , γ and δ . Red represents the original points in the input image. Green represents the measured point in the re-convolved image. One can see that in stripe α the position in x-direction is reproduced very well, since the y components vary. This can be seen better in figure 4.7a. For the stripes β , γ and δ it is similar, but in these cases the y-components can be reproduced well and the x-components vary. It is important to mention that although in the input image all points are placed in a line (red line), the linearity can not always be determined. The reason therefore is that in very dense regions the placed points are difficult to find. The gaussian fit is performed for a 10 px x 10 px area around the known position of the input points. In cases where multiple sources are in this area, the gaussian function may fit another source and performs the fit accordingly.

Tab. 4.5: Mean value and errors of stripes α , β , γ and δ .

Stripes		\bar{x} [px]	Δx [px]	\bar{y} [px]	Δy [px]
α	Output			10.95	3.58
	Input			10,59	0.66
β	Output	10.85	3.05		
	Input	11.00	0.62		
γ	Output	13.59	1.56		
	Input	11.15	0.95		
δ	Output	11.06	3.14		
	Input	11.47	0.85		

be able to retrieve stellar positions from faint stars that move within these associations. These motions then allow to derive enclosed masses of the black holes. In Mužić et al. (2008) the proper motion of several sources within the extremely dense stellar association IRS 13E are measured. This measurement of the northern sources (mostly Wolf-Rayet and O-type stars) show that six of seven of these resolved source show a common proper motion. These results favour the hypothesis that the complex of extremely red sources (IRS 13N) half an arcsecond north of IRS 13E are very young stars (less than 1 Myr.), but the conclusions are not clear. According to today's state of knowledge, star formation took place in two star bursts: one ~ 100 Myr years ago and one ~ 7 Myr ago. Finding younger stars in the Galactic Center would imply two things: on the one hand star formation near massive black holes could be possible in general. On the other hand the existence of younger stars could show that star formation is not limited on star burst. In order to determine the motions respectively the orbits around Sgr A* position measuring is necessary. This scenario is simulated by extracting an image of the S-cluster (labeled with the letters GC in Fig. 4.1) and placing it at three different locations as close as possible to the central stellar cluster (Fig. 4.8).

These positions are labeled II, III, and IV. Showing the central stellar cluster and the regions II, III, and IV in the input and re-convolved output images and measuring the stellar positions will demonstrate how well these stars can be recovered. Like one can see, the original picture of the GC (top left image in fig. 4.8) is ex-

tremely detailed and star clusters can be identified. The GC in the resulting image after de-convolving shows less structures, but the positions of individual sources can still be determined, although the single structures are ex-patiated. Since GC III is farthest away from the the guiding stars, the image quality drops as expected. Almost none of the sources can clearly be determined. Due to the fact that both, GC II and GC IV are closest to the guiding stars, more details can be seen. Nevertheless, in both cases an allocation of structures to the original sources is hardly possible. One can see that the background noise is reduced in all re-convolved images. Halos which can be seen in the original image of the Galactic Center lack completely in the re-convolved images.¹

¹Please consider that an observation of only five seconds were simulated. A longer observation would allow to reconstruct more and sharper details of the input image. Please see section [4.6](#)

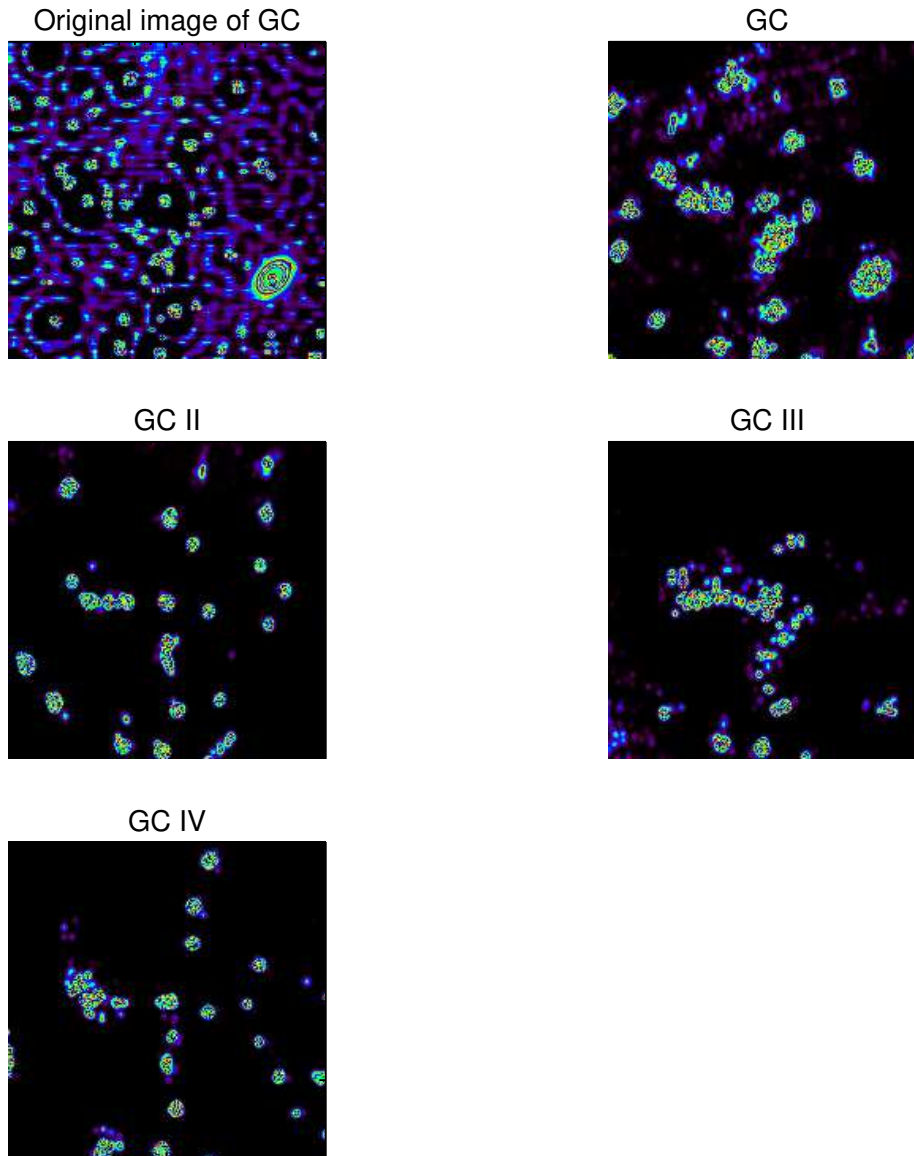


Fig. 4.8: Small stellar associations.

Left top: Original image of GC. Right top: GC. Middle left: GC III. Middle right: GC II, Bottom left: GC IV. Each image shows a detail of $1'' \times 1''$.

Like one can see the original picture of the GC is extremely detailed and star clusters can be identified. The GC in the resulting image after de-convolving shows less structures, but the positions of individual sources can still be determined, although the single structures are expatiated. Since GC III is farthest away from the the guiding stars, the image quality drops as expected. Almost none of the sources can clearly be determined. Due to the fact that both, GC II and GC IV are closest to the guiding stars more details can be seen. Nevertheless, in both cases an allocation of structures to the original sources is hardly possible. One can see that the background noise is reduced in all re-convolved images. Halos which can be seen in the original image of the Galactic Center lack completely in the re-convolved images.

4.3 Thin dusty filaments

Especially along the eastern arm and within the western bar of the mini-spiral, one finds long thin filaments that are prominent in the L-band at $3.8 \mu\text{m}$ wavelength. They were included in the simulations since it is very likely that the strongest of these filaments will show up also in the K-band at $2 \mu\text{m}$ wavelength if the region is observed with high angular resolution imaging techniques. These filaments are very thin (probably not (easily) resolvable perpendicular to their extent) and are probably due to dust and gas that is swept up by the strong winds from the hot He-stars or a wind from Sgr A* itself. The structures are placed at positions labeled A and B in the original input image. Showing the two filaments in the input (fig. 4.9) and re-convolved output images (fig. 4.10) demonstrates how well these structures can be recovered. As one can see in both cases the linearity of the original filaments are recognisable. Since the structure A is closer to guiding stars, more points could be resolved. However the line structure is broken down to seven more or less separate points, such that the linearity is apparent but does not allow the conclusion that these points are coherent. Also, the individual points are wider than the original line structure width. In the re-convolved image B is, reconstructed as a narrow and oblong structure with two separate maxima.²

²Please consider that an observation of only five seconds were simulated. A longer observation would allow to reconstruct more and sharper details of the input image. Please see section 4.6

In Mužić et al. (2007) the proper motion of such thin filaments are investigated in the L'-band ($3.8 \mu\text{m}$) with the NACO adaptive optics system at the ESO VLT UT4. They can be found inter alia in the mini-spiral (roughly $40'' \times 40''$ around Sgr A*) which is hosted in a dense clumpy molecular ring of circum nuclear disk (CND). This mini-spiral contains several narrow, filamentary structures and in Mužić et al. (2007) approximately the central $18 \times 18 \text{ arcsec}^2$ were studied. These thin filaments are curved with their convex side westwards and could originate from interaction with fast wind of the interstellar medium. It could be shown that they have a proper motion to the west. However, the analysis of the Keplerian orbit fitting shows that this motion cannot only be caused only by the gravitational effect of the SMBH. Mužić et al. (2007) propose that two sources can have an additional effect to this proper motion:

- ▶ An outflow emanating from the black hole at the position of Sgr A* and
- ▶ an outflow from the disk of mass-losing He-stars.

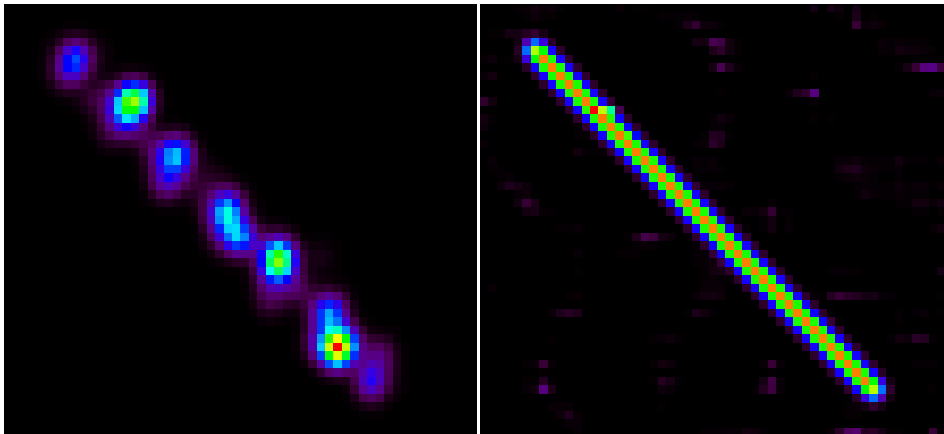


Fig. 4.9: Linear structure A. Left: Re-convolved image. Right: Original input image. Each image shows a detail of $0.275'' \times 0.25''$.

As one can see the linearity of the original filaments are recognisable. Since the structure A is closer to guiding stars, more points could be resolved. However, the line structure is broken down to seven more or less separate points, such that the linearity is apparent but does not allow the conclusion that these points are coherent. Also, the individual points are wider than the original line structure width.

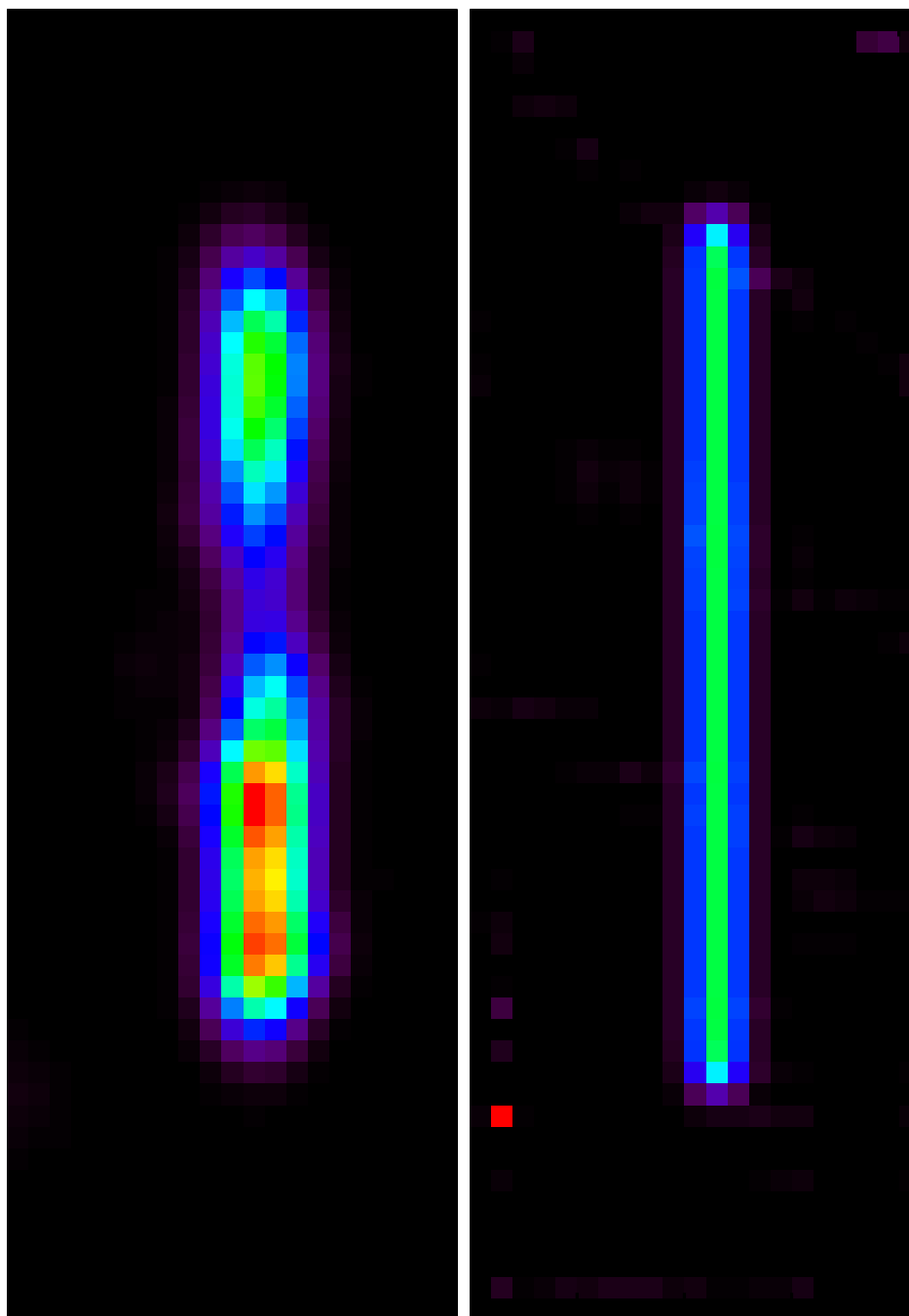


Fig. 4.10: Linear structure B. Left: Re-convolved image. Right: Original input image. Each image shows a detail of $0.1'' \times 0.3''$.

As one can see the linearity of the original filaments are recognisable. B is in the re-convolved image reconstructed as a narrow and oblong structure with two separate maxima. Also, the two maxima are wider than the original line structure width.

4.4 Disk embedded sources

There are several stellar sources in the central stellar cluster that are surrounded by extended dusty material. For sources within the mini-spiral, the extended material probably consist out of dust and gas swept up by the stellar winds of the stars moving through the mini-spiral. In a few cases the stars could also be surrounded by a small disk of dust if there are either very young or evolved (after an evolutionary phase of mass-loss). In Mužić et al. (2010) the proper motions of two comet-shaped sources X7 and X3 are investigated. The motion measurement is performed by observing the position ($\sim 0.8''$ and $3.4''$ projected distance to Sgr A*) of the objects of interest during several epochs covering approximately 6 years. The form of the bow-shock, the proper motion vector and the velocities show three characteristics:

- ▶ The bow-shock symmetry axes of these two sources are misaligned about 5° with their bow-shock point towards Sgr A*.
- ▶ Their proper motion vector shows about 45° away from connecting line between the sources and Sgr A*.
- ▶ A high proper motion velocity of several $100 \frac{km}{s}$.

These characteristics suggest that the bow-shocks origin in the interaction with fast winds from the Galactic Center.

Since the time measurement is considered to be accurate, the position determination comes with a certain inaccuracy. To simulate this scenario and to determine how well the extended structures and the inclosed stars can be recovered by the data reduction the objects a, b, c, d, e, f, g, h, k and m were included. Here, Gaussian shaped hard edged profiles were used at various ellipticities in order to simulate these extended disks at different inclination angles.

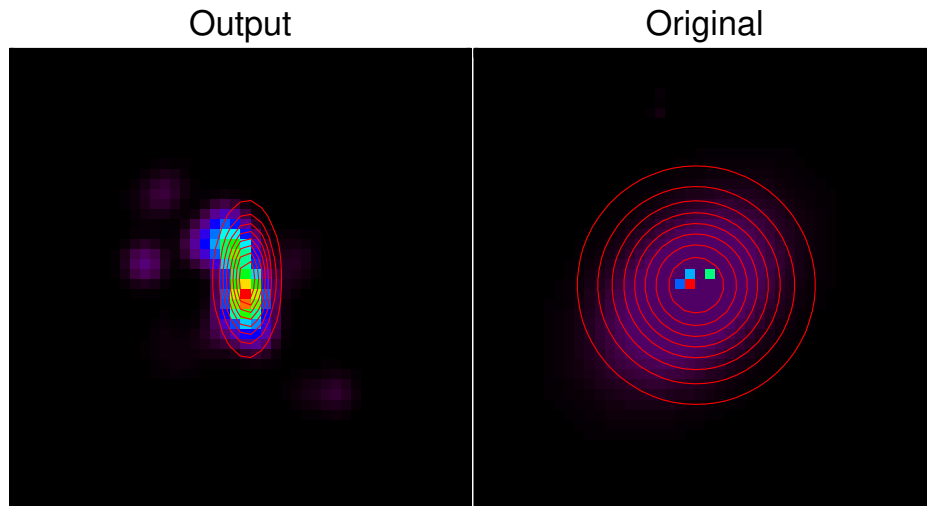


Fig. 4.11: Source a: each image shows a detail of $0.225'' \times 0.225''$.

The right image shows the original input gaussian source. On the left the re-convolved output source is shown. One can see that the re-convolved image is no longer symmetric, and therefore the fitted gaussian function is narrower than in the original input source. The position determination however is accurate. In the re-convolved image also additional points sources are recognisable. Most likely, these additional structures originate in inaccuracy during the de-convolution process.

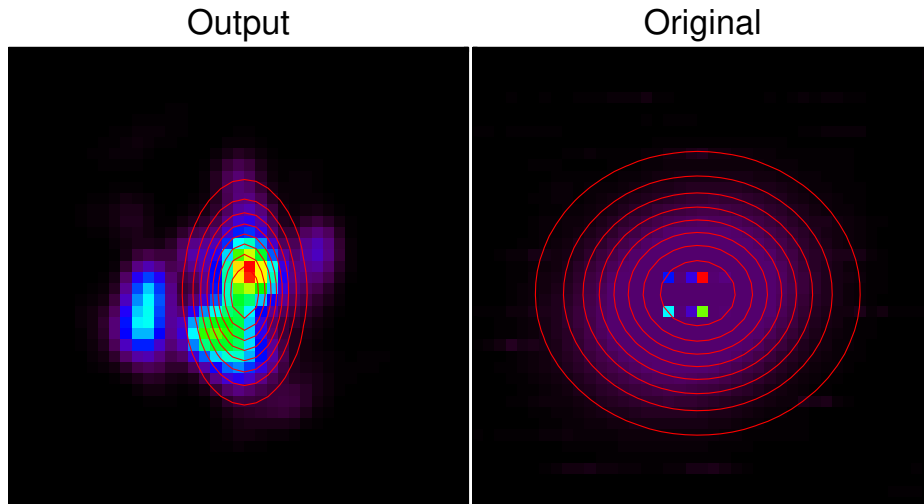


Fig. 4.12: Source b: each image shows a detail of $0.225'' \times 0.225''$.

The right image shows the original input gaussian source. On the left the re-convolved output source is shown. The re-convolved image is no longer radially symmetrical and shows two maxima. The gaussian fit matches best on the right maxima. In general, the position determination is accurate but the symmetric form of the input point source is mostly lost during the convolution and re-convolution process.

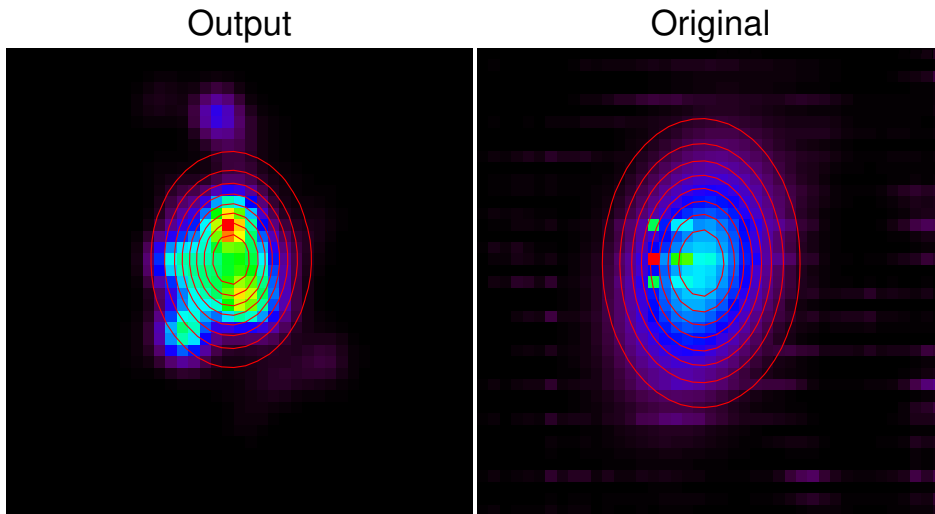


Fig. 4.13: Source c: each image shows a detail of $0.225'' \times 0.225''$.

The right image shows the original input gaussian source. On the left the re-convolved output source is shown. Since in the input image additional structures around the source point are given, in the re-convoluted image these structures are missing. In general, the radial symmetric form is given in the output image, although there is no longer a single, centre maxima, but two maxima slightly below and above the original maxima of the input image. Above the central structure also small round structure is recognisable.

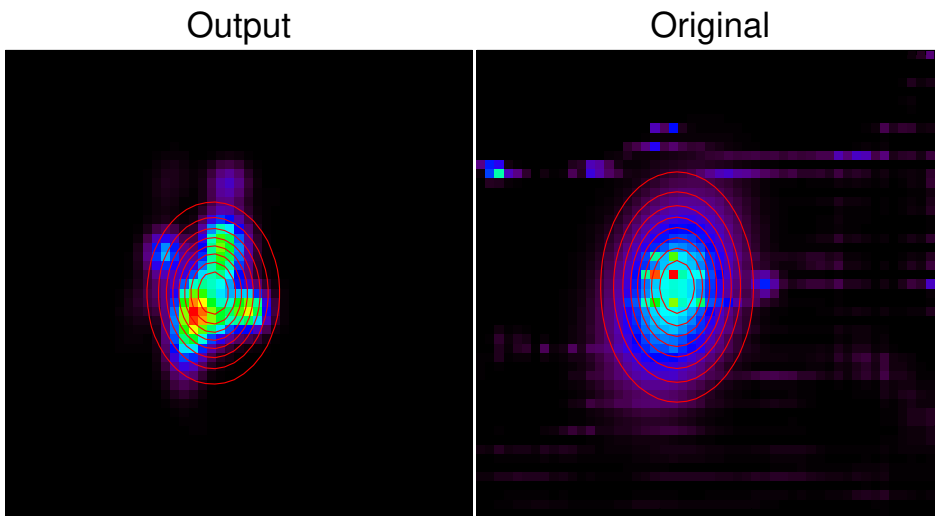


Fig. 4.14: Source d: each image shows a detail of $0.225'' \times 0.225''$.

The right image shows the original input gaussian source. On the left the re-convolved output source is shown. In the input image, several structures around the central gaussian source are given. These structures are lost in the re-convoluted image, which means that detailed structures cannot be reproduced after re-convolution. Although in the output structure the radial symmetric structure of the input source can hardly be seen, the position determination is accurate.

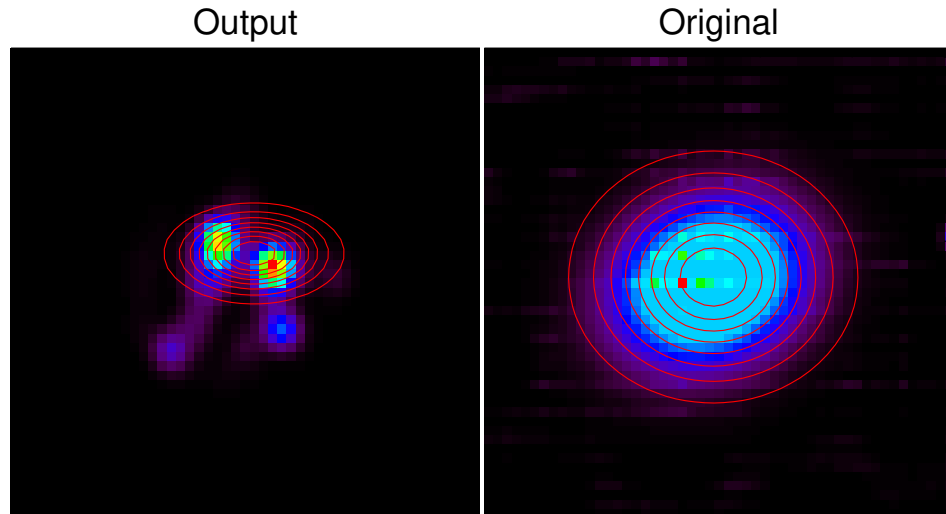


Fig. 4.15: Source e: each image shows a detail of $0.225'' \times 0.225''$.

The right image shows the original input gaussian source. On the left the re-convolved output source is shown. The radial symmetric input source is split up into two separate bigger maxima and two minor maxima. The symmetric structure is hereby no longer recognisable, although the position determination is quite good but varies from the position of the input source.

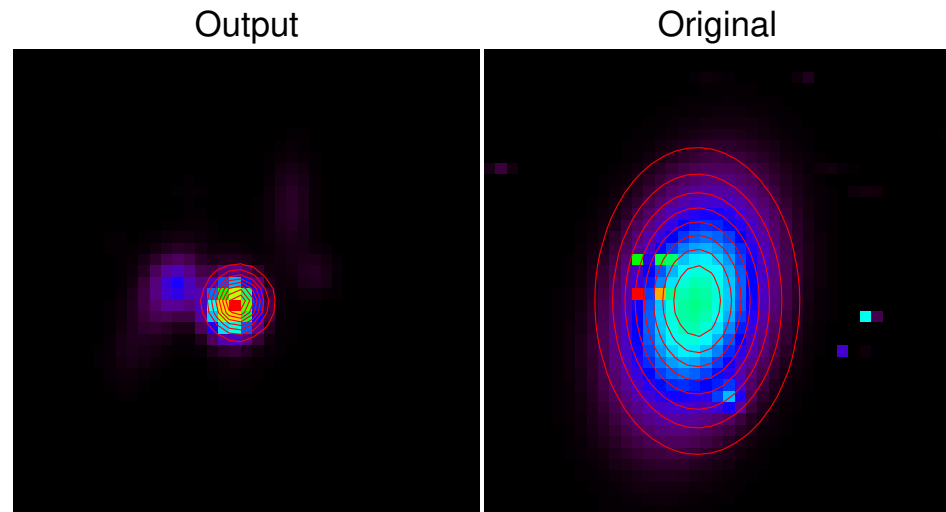


Fig. 4.16: Source f: each image shows a detail of $0.225'' \times 0.225''$.

The right image shows the original input gaussian source. On the left, the re-convolved output source is shown. The radial symmetric input source is split up into two separate maxima. The central, more dominant maxima show a radial symmetric structure but is much smaller in diameter. This leads to a smaller 1σ -error of the gaussian fit.

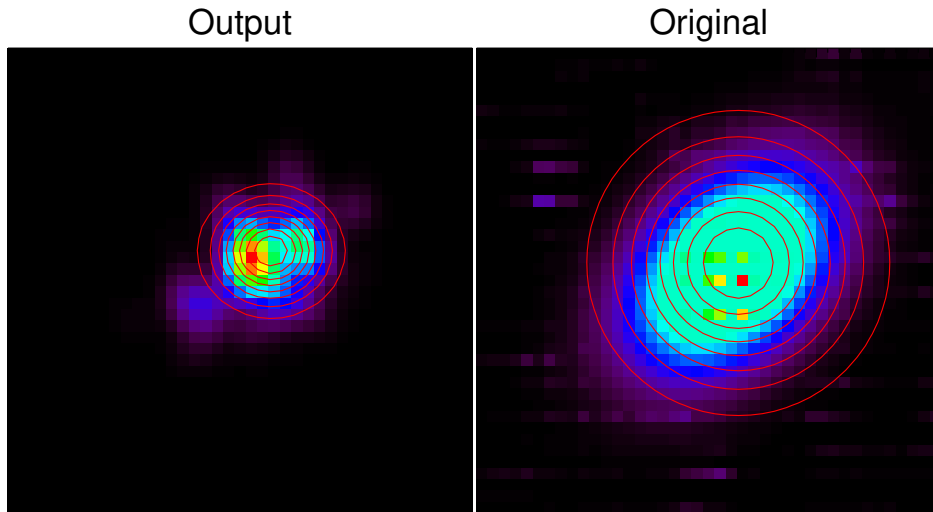


Fig. 4.17: Source g: each image shows a detail of $0.225'' \times 0.225''$. The right image shows the original input gaussian source. On the left, the re-convolved output source is shown. The radial symmetric input source can be reconstructed in the re-convolved image, since the structure is frayed and smaller in diameter.

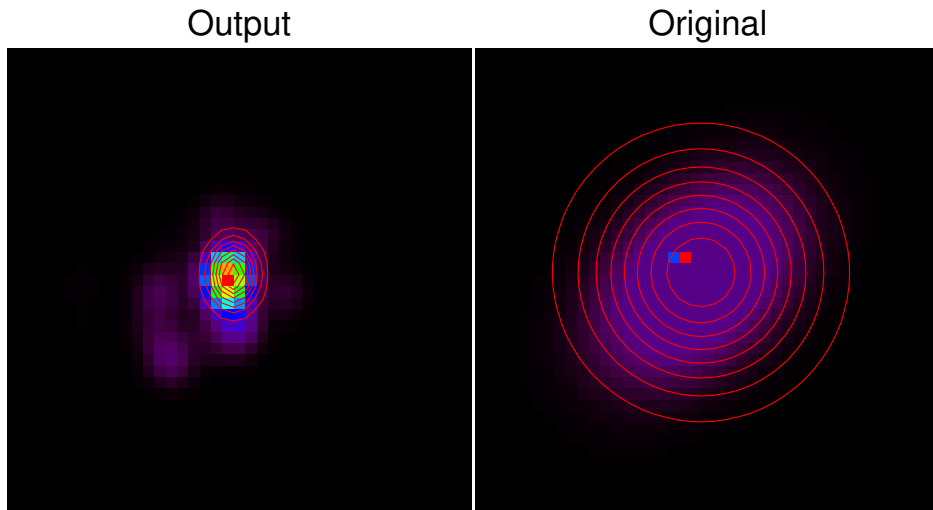


Fig. 4.18: Source h: each image shows a detail of $0.225'' \times 0.225''$. The right image shows the original input gaussian source. On the left, the re-convolved output source is shown. The radial symmetric input source is reconstructed as a more smudged structure, but still a central maxima is recognisable. Around the central maxima several small structures can be seen.

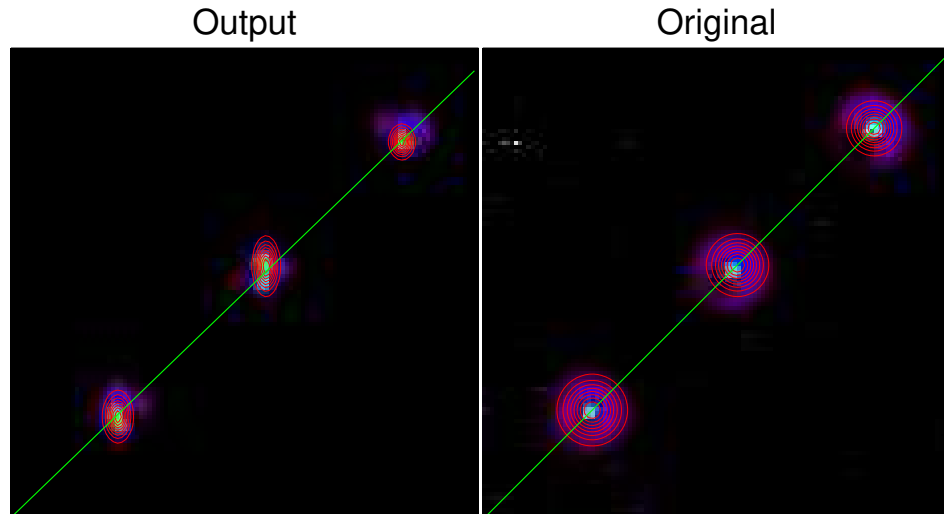


Fig. 4.19: Source k: each image shows a detail of $0.575'' \times 0.575''$.

The right image shows the original input gaussian source. On the left the re-convolved output source is shown. The input image shows three comet-shaped sources. Since both the three central maxima and the linearity of the three input source can be reproduced, the comet-shaped characteristics can no longer be seen. This shows that observing comet-shaped structures in the Galactic Centre is still a challenge.

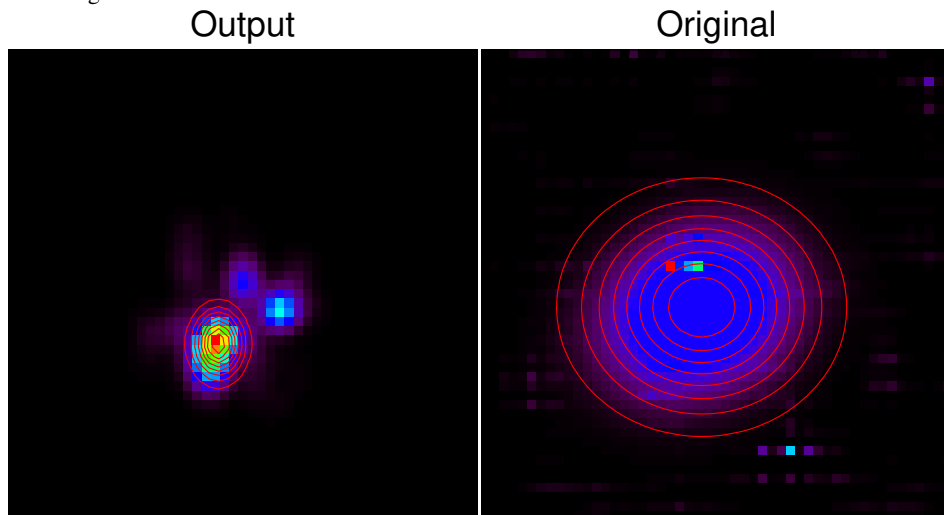


Fig. 4.20: Source m: each image shows a detail of $0.225'' \times 0.225''$.

The right image shows the original input gaussian source. On the left the re-convolved output source is shown. The radial symmetric structure of the input image is split up into three maxima. The major maxima is positioned slightly below the original position and is narrower than the original one.

Showing the input (right pictures) and re-convolved output images (left pictures) for each sources and measuring of the star to disk contrast, it is demonstrated how well the structures can be recovered.³ Therefore, for each input and output source a gaussian interpolation is performed in order to get both the peak position and the error of each source. The error is 1σ of the peak point. The results are listed in table 4.6.

Tab. 4.6: Positions of sources a, b, c, d, e, f, g, h, k and m in the original image and the re-convolved output, including errors in x and y direction.

Sources	Input		Output	
	(X Y) [px]	(ΔX ΔY) [px]	(X Y) [px]	(ΔX ΔY) [px]
a	(21.18 21.42)	(5.39 5.40)	(22.67 22.01)	(1.51 3.54)
b	(19.07 18.14)	(6.55 5.72)	(20.01 18.23)	(2.49 4.54)
c	(18.73 21.08)	(3.92 5.75)	(18.77 21.39)	(3.17 4.28)
d	(21.00 24.17)	(3.82 5.75)	(21.79 23.53)	(3.29 4.54)
e	(23.92 25.07)	(7.20 6.27)	(25.38 27.55)	(4.46 2.47)
f	(17.82 17.97)	(4.06 6.11)	(18.75 17.87)	(1.43 1.51)
g	(21.97 20.94)	(6.05 6.10)	(22.10 21.94)	(2.94 2.66)
h	(18.92 20.20)	(5.94 5.97)	(19.00 20.05)	(1.34 1.85)
k	(26.67 25.73)	(4.09 4.16)	(26.09 24.13)	(1.78 3.06)
	(62.10 61.09)	(3.61 3.64)	(62.21 60.83)	(1.63 3.52)
	(97.11 96.11)	(3.26 3.24)	(97.02 92.73)	(1.56 2.11)
m	(22.94 22.15)	(7.21 6.42)	(21.95 18.33)	(1.62 2.21)

In addition, in case k (fig. 4.19) three comet-shaped sources are investigated. In the input image all three sources are positioned on a line. In the output image the positions are measured and a linear regression is performed. The slopes and intersects are listed in 4.7. The measurements are shown in fig. 4.21.

³Please consider that an observation of only five seconds were simulated. A longer observation would allow to reconstruct more and sharper details of the input image. Please see section 4.6

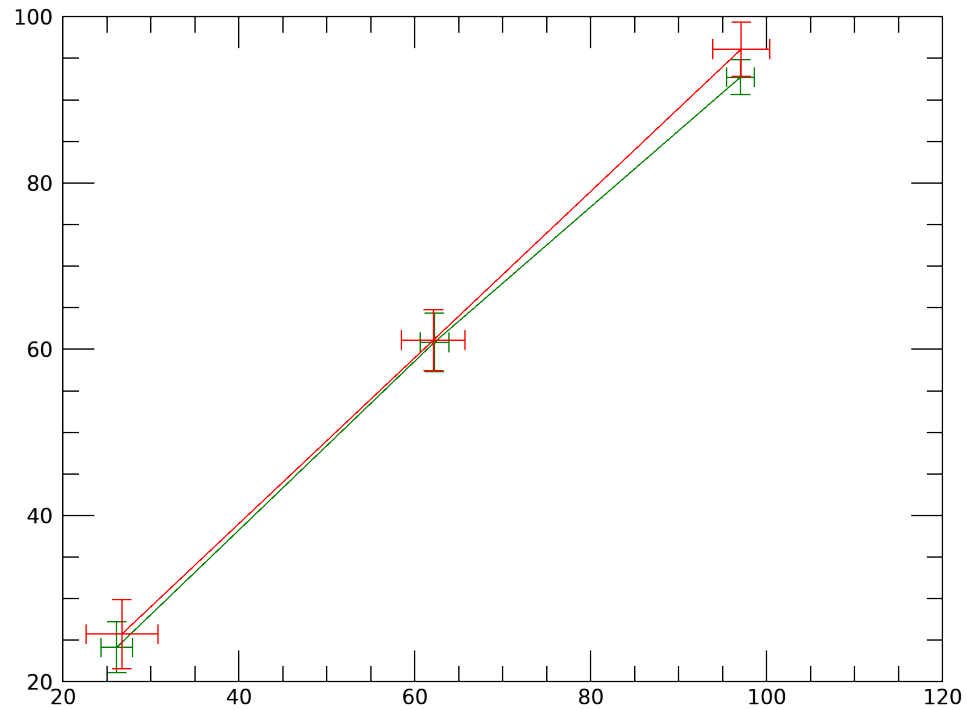


Fig. 4.21: Position measurement of the three sources k .

The red line represents input sources and the green line the position of the re-convolved sources. Both in the input and the re-convolved image the three sources lay on a line. The error bars for the re-convolved sources are smaller due to the fact that the re-convolved structures are narrower than the original ones.

Tab. 4.7: Slope and intersections of the line fits of the three sources k .

	Slope m	Δm	Intersect b	Δb
Output	0.9640	0.0610	-0.4825	4.6336
Input	0.9992	0.1046	-0.9375	7.6477

As the extended structures are difficult to be recovered and individual results depend on the details of the noise and PSF side-lobe distribution one can assume that some of these effects average out if one sums up many trails. The produced two sums show two more similar images with less artefacts in the extended halos as shown in figure 4.22. The summarised re-convolved image on the left has a smaller

diameter and the circular form is less uniform than the summarised original input on the right side. For both summarised images again a gaussian function was fitted in order to perform a position determination and the results in table 4.8 show that the position determination works quite well.

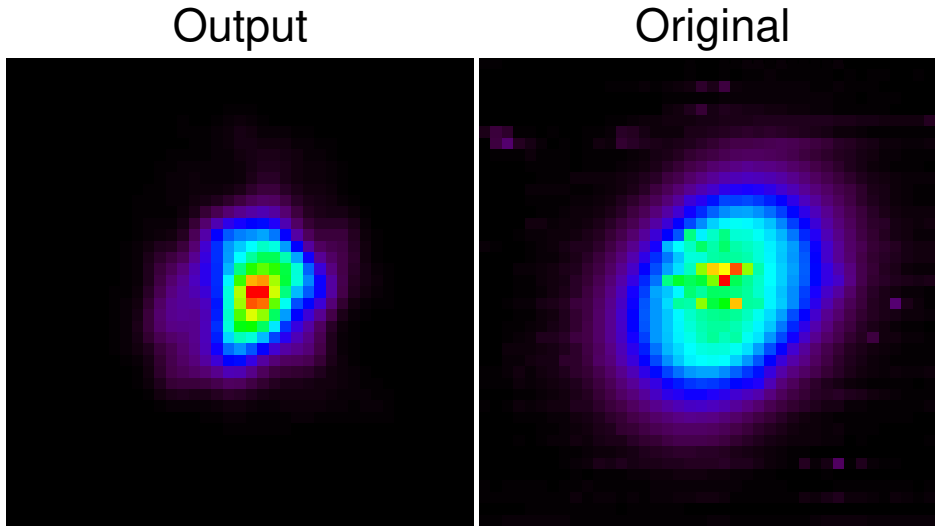


Fig. 4.22: Sum of disk embed sources a, b, c, d, e, f, g, h and m. Detail of 0.2" x 0.2".

Tab. 4.8: Positions of sources a, b, c, d, e, f, g, h, k and m in original image and re-convolved output including errors in x and y direction.

Output		Input	
(X Y) [px]	(ΔX ΔY) [px]	(X Y) [px]	(ΔX ΔY) [px]
(21.54 20.14)	(2.94 3.65)	(20.96 20.13)	(5.39 5.96)

4.5 Cometary and asymmetric bow-shock sources

Some of the embedded dusty sources are asymmetric bow shock sources and cometary shaped sources. In the first case the asymmetry is due to the motion of the source through the interstellar medium and in the second case the shape is due to a strong

wind blowing against the stars dust shell. The asymmetric sources are mostly associated with the mini-spiral (see section 4.3) and the cometary sources that lie in the mini-cavity that is blown into the mini-spiral most likely by a wind from Sgr A*. In feature k, a star into an increasingly (from south east to north west) asymmetric extended cone-shaped structure is placed. In table 4.6 the measured input and re-convolved output points are shown. Figure 4.19 shows how well the structures can be reproduced.⁴ In addition, a linear regression is performed on the three point in both the input and re-convolved image (fig. 4.21). The slopes and intersects are listed in table 4.7. Tanner et al. (2002) investigate the cold source IRS 21 with the W. M. Keck 10 m telescope that provided diffraction-limited 2-25 μm images of the central parsecs of the Galactic Centre. Tanner et al. (2002) conclude that IRS 21 is a massive star that pass through the norther arm sources IRS 1, 2, 5, 8 and 10 while loosing mass. The interaction of this medium with dust and gas of the northern arm that falls in and orbits Sgr A* creates bow-shocks. In order to determine the size of IRS 21 as best-fitting model profile an Gaussian HWHM is assigned. The immense size of IRS 21 of ~ 650 AU at 2.2 μm and of ~ 1600 AU at mid-infrared is more than 2 magnitudes greater than expected⁵. The most obvious explanation is the bow-shock dust distribution model, where the dust profile is a spherical shell with a constant dust density. From this and with a luminosity of $\sim 10^4 L_{\odot}$ follows that most probably the central source is a Wolf-Rayet star.

4.6 Results

This thesis dealt with the simulation of detecting electromagnetic waves coming from celestial objects through Earth's atmosphere with AO-corrected interferometric telescopes. The main purpose was to understand the magnitude of measuring errors during position determination. Therefore, science cases were added to an image of the Galactic Centre and the propagation through Earth's atmosphere, detecting and the reconstruction of the original image were simulated. Then position determination on the original and reconstructed image were performed and the

⁴Please consider that an observation of only five seconds were simulated. A longer observation would allow to reconstruct more and sharper details of the input image. Please see section 4.6

⁵The largest stellar photosphere (a M supergiant) is about 4 AU

measuring errors were determined as mean value of all errors and are calculated as shown in table 4.9.

Tab. 4.9: Mean measuring errors for original and re-constructed image in x- and y-direction in pixel and milliarcseconds

	Δx [px]	Δy [px]	Δx [mas]	Δy [mas]
Input	0.25	0.26	1.26	1.32
Output	0.43	0.27	2.16	1.36

Considering the image size and resolution the correlation between pixel and milliarcseconds is given as:

$$5 \text{ mas} = 1 \text{ pixel} \quad (4.4)$$

With the results from table 4.9 now the error of proper motions:

$$\Delta v = \frac{\Delta s}{t} = \frac{\sqrt{\Delta x^2 + \Delta y^2}}{t} = \frac{2.55 \text{ mas}}{t} \quad (4.5)$$

can be estimated.

The calculated error on the proper motion in equation 4.5 applies for a simulated observing duration of 5 seconds. If the simulation observing duration was extended to 1 hour, the error of the proper motion would be reduced by

$$\frac{1}{\sqrt{\frac{t_{int}}{5 \text{ sec}}}} = \frac{1}{\sqrt{\frac{3600 \text{ sec}}{5 \text{ sec}}}} \approx \frac{1}{27} \quad (4.6)$$

and the error of the proper motion measurement would be

$$\Delta v = \frac{\Delta s}{t} = \frac{\sqrt{\Delta x^2 + \Delta y^2}}{t} = \frac{0.095 \text{ mas}}{t}. \quad (4.7)$$

Due to the long calculating period of round about 3 weeks for the simulation of a 1 second observation, the simulation of a 1 hour observation was foregone and the resulting decrease of the error of the proper motion was estimated in equation 4.6.

Summary

Many topics were covered in this thesis in order to be able to determine the measuring errors in table 4.9 by means of the simulated science cases.

Chapter 1: Theory

In the first chapter the functional principle of telescopes and interferometers, imaging theories and physically given borders of angular resolution are presented. Furthermore, the atmospheric influences on wavefronts propagating through it and the reasons for these effects are discussed. Atmospheric models are introduced in order to be able simulating those effects. As a solution to overcome the limitations of imaging through Earth's atmosphere, adaptive optics and the corresponding theories were introduced. The central object of interest, the Galactic Centre, is described in various wavelength bandwidths. Later on, stellar movements are investigated, since position, rotation and appearing altitude of observed celestial object are key simulation parameters. Finally, the simulated telescope is introduced and described. These telescope characteristics are one of the main simulation parameters.

Chapter 2: Software description

Chapter two describes the numerical simulation tool LOST that was used to produce the resulting PSFs. These PSFs contain the disruptive effect of imaging through Earth's atmosphere and telescope instruments and the corrections made by the multi-conjugate adaptive optics modules. A layer orientated approach with

Kolmogorov atmospheric model is implemented. LOST is written in the Interactive Data Language (IDL) and script based. The script files contain the telescope setup like mirror diameter or pupil dimension. The atmospheric model, the number of layers and natural guiding stars are also configured in the script files. Other parameters are the field of view, number of deformable mirrors and other numerical parameters. The simulations are started by defining the parallactic angle, the wavelength that should be observed and the simulated observation time. The propagation through the atmospheric layers is performed by using geometrical optics approximations. Also, the adaptive optical correction are performed and finally the PSF files are generated. Even with the same parameters and setup configurations, each simulation is unique since the moving speed of each atmospheric layer is randomly chosen. Though it is also possible to use the same atmosphere for different simulations.

The PSF can be convolved with any input image. This convolved image simulates the image one would see in the telescope after the electromagnetic waves would have passed Earth's atmosphere. The purpose of observing celestial object is of course to know the image without the disturbing effect of Earth's atmosphere and instruments. This process of reconstructing the initial image after the imaging process is called re-convolution. Since convolving is a simple Fourier multiplication, a division of the output image by the PSF in order to get the initial image is due to numerical reasons not possible. The procedure of re-convolving is described in chapter 3.

Chapter 3: Simulations

Since LOST does not generate one single PSF, but divides the whole FoV into sections with separate PSFs, a number of processings must be performed to generate one single contiguous picture. One example with a central natural guiding star is shown in figure 5.1 with the corresponding Strehl map in figure 5.2. Each PSF in figure 5.1 represents the disturbances in this particularly area and therefore an input image must convolved with each of these PSFs and the resulting images must be assembled in a way that the part of each convolved image corresponding to the position of the PSF is stitched together.

PSFs

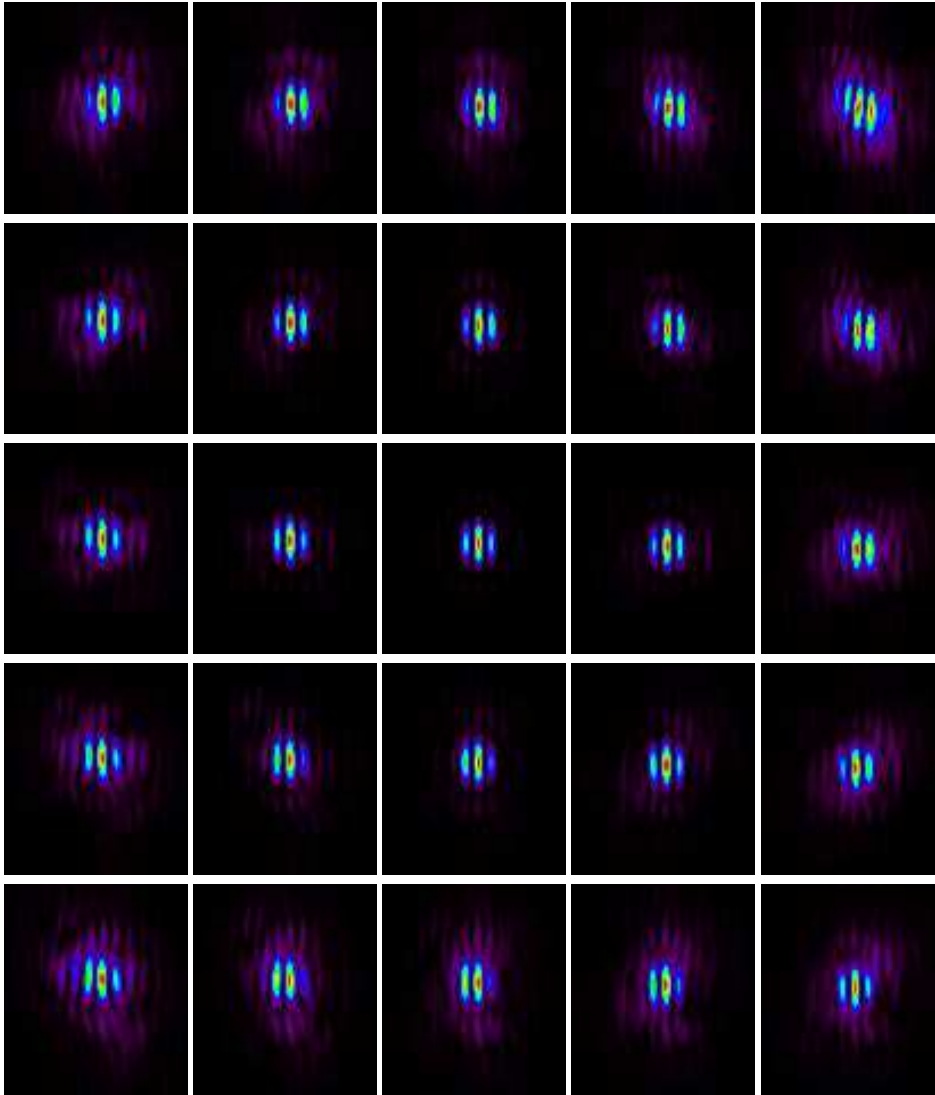


Fig. 5.1: Whole FoV divided in 5×5 simulated PSFs with a centred NGS.

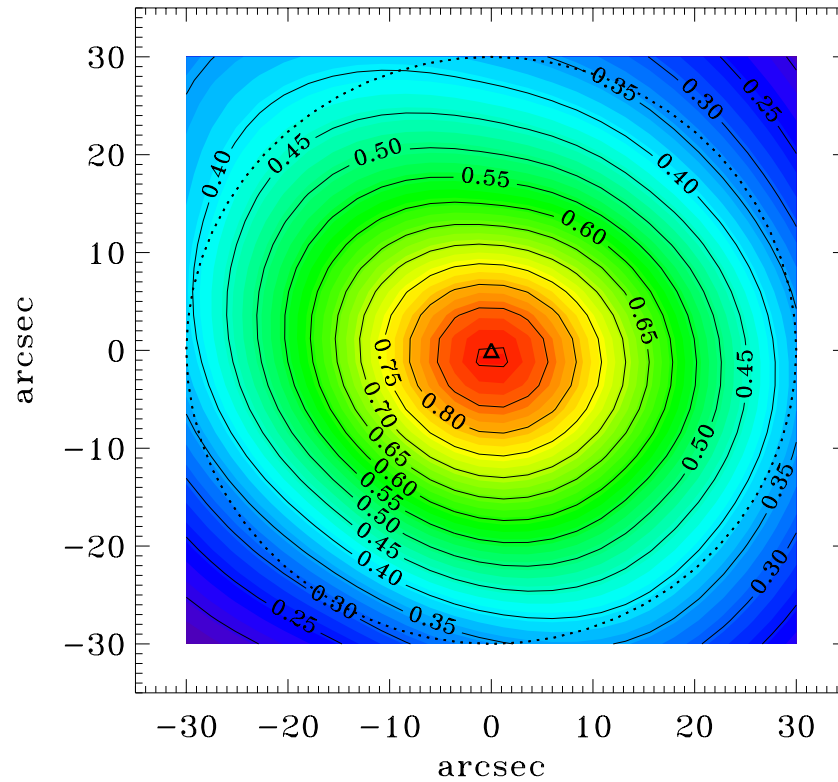


Fig. 5.2: Strehlmap corresponding to PSFs in figure 5.1

Such a composed convolved image needs to be re-convolved in order to produce the original input image. Since a division of the output image by the PSF is numerical not possible, an approximation method is used where a hypothesised input image is taken, convolved with the known PSF and compared to the also known output image. By comparing the true output image with the hypothetical one, a correction matrix is calculated and multiplied with the initial hypothesised input image. By repeating this procedure often enough, the hypothetical input image will converge to the real input image. This procedure is called the lucy-algorithm. This chapter also contains additional test constellations. Finally, the science cases were simulated with two natural guiding stars. The science cases were placed in an image of the Galactic Centre. The PSFs were simulated for various parallactic

angles and were averaged. This single averaged PSF is convolved with the image of the Galactic Centre that contains the science cases.

Chapter 4: Science cases

In chapter four finally the convolved output image is re-convolved and the single science cases are investigated as bow shocks, proper motion, thin elements, small stellar associations and disk embedded sources. Since the science cases in figure 5.3 are located in different areas within a detail of $10'' \times 10''$ around the Galactic Centre, the reconstruction quality varies from observing point to observing point. Although all of the various science cases shown in figure 5.3 were investigated by comparing the position determinations and their measuring errors of the original input image and the re-convolved one, different aspects matter:

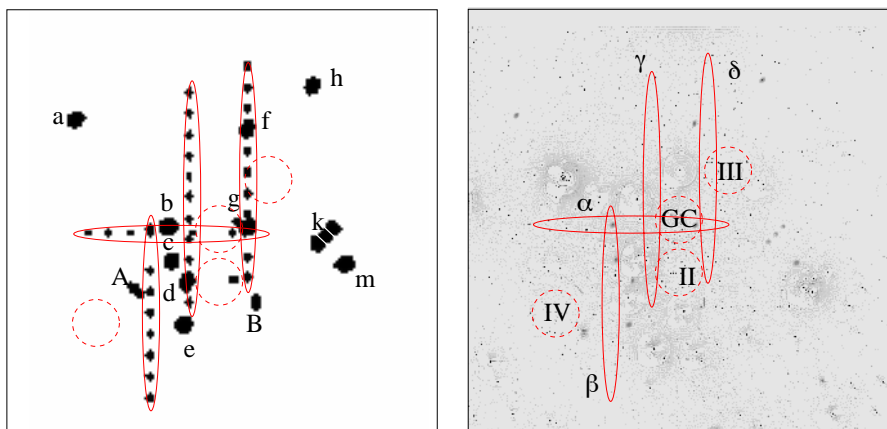


Fig. 5.3: Science Cases, $10'' \times 10''$ detail around the Galactic Centre:

α, β, γ and δ : Proper motions,
 GC, II, III and IV: small stellar associations,
 A and B: Thin dusty filaments,
 a, b, c, d, e, f, g, h and m: disk embedded sources,
 k: cometary and asymmetric bow-shock sources.

- **Proper motion:** For instance for the proper motion cases α, β, γ and δ it is important to understand if the linearity of these structure can be reconstructed after re-convolution.

- ▶ **Small stellar associations:** In the case of small stellar associations, it is of interest if structures within different regions around the Galactic Centre are recognisable after the re-convolution process.
- ▶ **Thin dusty filaments:** Thin dusty filaments are very thin and oblong structures. Here the main question is whether these structures can be reproduced.
- ▶ **Disk embedded sources:** These sources are gaussian shaped forms. The input sources have a certain peak and width. Here, is of interest if the form and position of these structures can be reproduced.
- ▶ **Bow-shock sources:** Bow-shock sources have a characteristic sickle-shaped form. It was investigated if this special characteristic form of these sources can be reconstructed.

The original input image and the re-convolved output image are shown in figure 5.4.

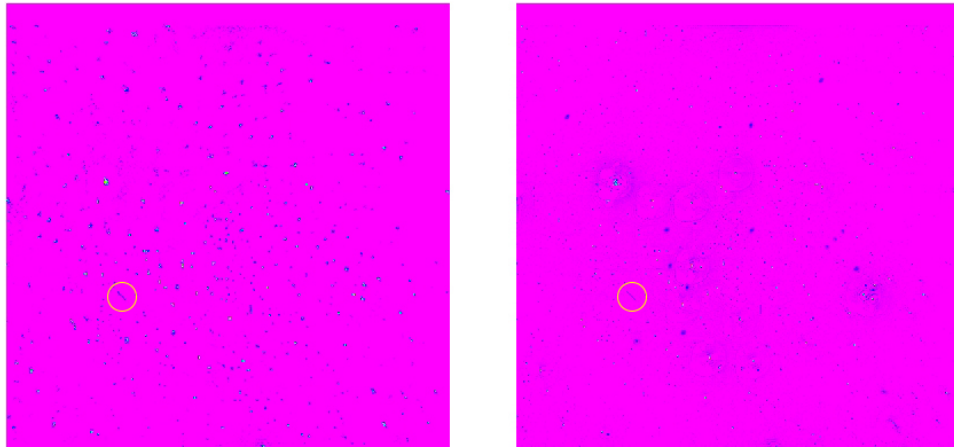


Fig. 5.4: Left: Output picture after de-convolving.
Right: Input picture of Galactic Center in high resolution with science cases (both: 10" x 10" detail in 2000 x 2000 pixel resolution).

Each science case was put into context of current scientific research and almost all of them have in common that position determination, including error estimation, were performed. Due to the evaluation of these measuring errors, the results table 4.9 could be determined.

Bibliography

- 2pem Wikipedia. 2015, Zernike [6](#), [44](#)
- Arcidiacono, C. 2005 [74](#), [76](#)
- Balick, B. & Brown, R. L. 1974, The Astrophysical Journal, 194, 265 [58](#)
- Bertram, T. 2007, Universität zu Köln [7](#), [39](#), [65](#), [70](#)
- Cox, A. N. 2015, Allen's astrophysical quantities (Springer) [38](#)
- Eckart, A., Schödel, R., & Straubmeier, C. M. 2005, The black hole at the center of the Milky Way (World Scientific) [49](#), [53](#), [55](#), [78](#)
- Etzaluze, M., Smith, H. A., Tolls, V., Stark, A., & González-Alfonso, E. 2011, The Astronomical Journal, 142, 134 [6](#), [54](#)
- Fried, D. L. 1966, JOSA, 56, 1372 [40](#)
- . 1982, JOSA, 72, 52 [48](#)
- Genzel, R., Eisenhauer, F., & Gillessen, S. 2010, Reviews of Modern Physics, 82, 3121 [56](#)
- GMT. 2018, Giant Magellan Telescope , <https://www.gmto.org/2013/01/winter-2013/> [5](#), [26](#)
- Jankov, S. 2010, Serbian Astronomical Journal, 181, 1 [31](#)
- Kolmogorov, A. N. 1941, Akademiia Nauk SSSR Doklady, 30, 299 [38](#)
- Krishnavedala. 2018, Own work, CC BY-SA 4.0 [5](#), [30](#)
- Kürster, M. 2010 [6](#), [7](#), [37](#), [68](#)
- LBT. 2018, Giant Magellan Telescope , <https://www.nasa.gov/topics/universe/features/lbti20101206-i.html> [7](#), [67](#)

- Masciadri, E., Stoesz, J., Hagelin, S., & Lascaux, F. 2010, *Monthly Notices of the Royal Astronomical Society*, 404, 144 [6](#), [39](#)
- Meeus, J. H. 1991, *Astronomical algorithms* (Willmann-Bell, Incorporated) [61](#), [62](#)
- Mužić, K., Eckart, A., Schödel, R., et al. 2010, *Astronomy & Astrophysics*, 521, A13 [123](#)
- Mužić, K., Eckart, A., Schödel, R., Meyer, L., & Zensus, A. 2007, *Astronomy & Astrophysics*, 469, 993 [121](#)
- Mužić, K., Schödel, R., Eckart, A., Meyer, L., & Zensus, A. 2008, *Astronomy & Astrophysics*, 482, 173 [117](#)
- NASA. 2018a, *Armstrong Flight Research Center*, <https://www.nasa.gov/centers/armstrong/> [5](#), [26](#)
- . 2018b, *NASA/CXC/SAO*, <http://chandra.si.edu/> [6](#), [7](#), [49](#), [52](#), [55](#), [56](#), [57](#), [58](#)
- Parsa, M., Eckart, A., Shahzamanian, B., et al. 2017, *The Astrophysical Journal*, 845, 22 [111](#), [112](#)
- Ragazzoni, R. 1996, *Journal of modern optics*, 43, 289 [69](#)
- Sabha, N. B. I. 2015, PhD thesis, Universität zu Köln [55](#)
- Schneider, P. 2007, *Extragalactic astronomy and cosmology: an introduction* (Springer Science & Business Media) [56](#)
- Tamás, S. 2018, Own work, CC BY-SA 3.0, [5](#), [29](#)
- Tanner, A., Ghez, A., Morris, M., et al. 2002, *The Astrophysical Journal*, 575, 860 [132](#)
- Tordi, M., Roberto, R., & Diolati, E. 2002, 58, 223 [8](#), [73](#), [74](#), [75](#)
- Traub, W. A. 1986, *Applied optics*, 25, 528 [6](#), [35](#), [36](#)

Danksagung

Diese Dissertation wäre ohne die Hilfe zahlreicher Personen nicht möglich gewesen.

Ich möchte mich an erster Stelle bei meinem Doktorvater, Herrn Prof. Dr. Andreas Eckart, dafür bedanken, dass er mir die Möglichkeit gegeben hat, diese Arbeit anfertigen zu können. Neben der inhaltlichen Führung bin ich vor allem für seine moralische Unterstützung dankbar. Jedes Gespräch hat meine Motivation und Zuversicht gestärkt. Vielen Dank für die Zeit, Mühen und Begeisterung, die mich immer wieder angesteckt haben.

Bedanken möchte ich mich zudem bei Prof. Dr. Lucas Labadie für die Erstellung des Zweitgutachtens sowie bei Prof. Dr. Bülent Tezkan für die Übernahme des Prüfungsvorsitzes. Auch Herrn Dr. Gerold Busch gilt mein Dank für die Übernahme des Prüfungsbeisitzes.

Bei Herrn Dr. Jens Dierkes und Herrn Dr. Matthew Horrobin möchte ich mich für die Unterstützung bei allen Fragen und Problemen rund um meine Arbeit bedanken. Many thanks also to Camelo Arcidiacono for providing LOST and most of all for the comments in the code. I would have been lost without them.

Herrn Dr. Achim Mester möchte ich für die anregenden Gespräche rund um meine Arbeit und das Korrekturlesen danken.

Anneme, Babama ve Ablamın teşekkür ederim. Desteğiniz ve emeğiniz için minnettarım.

Und dann natürlich Anne: Danke.

Erklärung

Ich versichere, dass ich die von mir vorgelegte Dissertation selbständig angefertigt, die benutzten Quellen und Hilfsmittel vollständig angegeben und die Stellen der Arbeit – einschließlich Tabellen, Karten und Abbildungen –, die anderen Werken im Wortlaut oder dem Sinn nach entnommen sind, in jedem Einzelfall als Entlehnung kenntlich gemacht habe; dass diese Dissertation noch keiner anderen Fakultät oder Universität zur Prüfung vorgelegen hat; dass sie noch nicht veröffentlicht worden ist sowie, dass ich eine solche Veröffentlichung vor Abschluss des Promotionsverfahrens nicht vornehmen werde. Die Bestimmungen dieser Promotionsordnung sind mir bekannt. Die von mir vorgelegte Dissertation ist von Herrn Prof. Dr. Andreas Eckart betreut worden.

Köln, den 24.07.2018

